THERMAL CONTACT RESISTANCE IN CARBON NANOTUBE FOREST INTERFACES

A Dissertation
Presented to
The Academic Faculty

By

John Harold Taphouse

In Partial Fulfillment
Of the Requirements for the Degree
Doctor of Philosophy in Mechanical Engineering

Georgia Institute of Technology

May 2015

Copyright © John Harold Taphouse 2015

THERMAL CONTACT RESISTANCE IN CARBON NANOTUBE FOREST INTERFACES

Approved by:

Professor Baratunde A. Cola, Advisor
George W. Woodruff School of Mechanical Engineering
Georgia Institute of Technology

Professor Samuel Graham, Co-Advisor
George W. Woodruff School of Mechanical Engineering
Georgia Institute of Technology

Dr. Jud Ready
Georgia Tech Research Institute
Georgia Institute of Technology

Professor Gleb Yushin
School of Materials Science and Engineering
Georgia Institute of Technology

Professor Satish Kumar
George W. Woodruff School of Mechanical Engineering
Georgia Institute of Technology

Date Approved: December 19, 2014

To my wife Trisha

ACKNOWLEDGEMENTS

I'd like to start by thanking my advisors Dr. Baratunde Cola and Dr. Samuel Graham. I am grateful for their candid advice, guidance, patience, and support throughout the entire Ph.D. degree. In particular, I'd like to thank Dr. Cola for never letting me settle. I came to Georgia Tech intending to put myself in an uncomfortable position where I would be continually forced to develop both intellectually and personally. His energy and incessant drive to better himself and those around him has undoubtedly accelerated my own development. Perhaps I can inspire him to do another pump-and-run someday. I'd also like to thank Dr. Satish Kumar, Dr. Gleb Yushin, and Dr. Jud Ready for serving on my committee. I have enjoyed our conversations and sincerely appreciate their time and insight.

Next I'd like to acknowledge all of those who have contributed to this research. I'd like to thank all members past and present of the NEST and EMRL labs, the staff of the Georgia Tech I.E.N., the faculty of the Woodruff School, Dr. O'Neil Smith and Professor Seth Marder for a fruitful collaboration, Dr. Andrey Voevodin and Dr. Christopher Muratore of the Air Force Research Laboratory and the University of Dayton, and many others. Without all of your help this degree would have not been possible. I'd especially like to thank Dr. Virendra Singh and Dr. Anuradha Bulusu for their selfless mentorship and generous assistance. I also owe special thanks to my colleague, mentor, and friend Mr. Thomas Bougher for all of his help and his willingness to have a conversation, whether it be about research or life.

Last, I'd like to thank all of my friends and family. I am grateful to Kyle Karlson for his friendship, support, and inclination to embark on many poorly planned adventures. I am deeply appreciative of everything my parents and grandparents have sacrificed and done to support me over the years. Their love empowered me throughout my childhood and continues to do so today. I'd also like to thank my siblings Kimberly, Phillip, and Sara, my Father In-law Harold Valley,

Denise Lafreniere, and my Mother In-law Carla Valley for their support and friendship. Most of all, I'd like to thank my wife Trisha. No one sacrificed more to make this degree a possibility. I am certain that I could not have done this without her selfless love and encouragement. I will forever be grateful.

TABLE OF CONTENTS

ACKNOWLEDGEMENTS iv

LIST OF TABLES ix

LIST OF FIGURES x

NOMENCLATURE xv

SUMMARY xviii

CHAPTER 1: INTRODUCTION 1
1.1 Motivation 1
1.2 Thermal Interface Materials 2
1.3 Carbon Nanotube Forest TIMs 4
1.4 Research Objectives 8

CHAPTER 2: BACKGROUND 11
2.1 Existing and Emerging TIMs 11
2.1.1 Conventional TIMs 11
2.1.2 Emerging Nanostructured TIMs 13
2.1.3 Evaluating TIM Performance 14
2.2 Thermal Transport at Contacts and Interfaces 15
2.2.1 Thermal Transport between Dissimilar Materials 15
2.2.2 Thermal Transport between Contacting Surfaces; The Effect of Surface Roughness 21
2.2.3 Additional Impediments to Thermal Transport 25
2.3 Thermal Transport at Carbon Nanotube Forest Contacts 27
2.3.1 Thermal Transport at Individual CNT Contacts 27
2.3.2 Contact Mechanics and Thermal Transport at the Scale of CNT Forests 30

CHAPTER 3: EXPERIMENTAL METHODS 33
3.1 Carbon Nanotube Synthesis 33
3.2 Thermal Metrology 35
3.2.1 Photoacoustic 36
3.2.2 Time-Domain Thermoreflectance 39

CHAPTER 4: ENHANCING CONTACT AREA: LIQUID SOFTENING 44
4.1 Introduction 44
4.1.1 Hypothesis 44
4.2 Methods 45
4.2.1 The Wet-Compress-Dry (WCD) Process 46
4.2.2 Photoacoustic 47
4.2.3 Shear Adhesion 48
4.2.4 Capillary Forces 48
4.2.5 Coarse-Grain Mechanics Simulations 49

4.3 Results 50
4.3.1 Photoacoustic Results 50
4.3.2 Shear Adhesion Results 52
4.3.3 Simulation Results 53
4.4 Discussion 54
4.4.1 Attenuation of Inter-CNT Van der Waals Interactions 54
4.4.2 Capillary Forces 55
4.5 Summary 58

CHAPTER 5: ENHANCING BOND STRENGTH WITH SURFACE MODIFIERS 59
5.1 Introduction 59
5.2 Pyrenylpropyl Phosphonic Acid 59
5.3 Interface Modification and Coupling Procedure 61
5.4 Total Thermal Resistance of PyprPA Coupled CNT Forests 62
5.5 Thermal Stability, Attachment Strength, and Electrical Characterization 66
5.6 Exploration of Additional Modifiers 68
5.7 Summary 70

CHAPTER 6: BONDING WITH NANOSCALE POLYMER COATINGS 71
6.1 Introduction 71
6.2 Polymer Coating and Bonding of CNT Forests 72
6.2.1 Coating and Bonding Procedure 72
6.2.2 Characteristics of Coated CNT Forests 73
6.3 Results 76
6.3.1 Total Thermal Resistance of Polymer Coated and Bonded CNT Forests 76
6.3.2 Thermal Stability of Polymer Coated and Bonded CNT Forests 78
6.3.3 Polymer Coated and Bonded Thermal Interposers 79
6.3.4 Shear Adhesion 79
6.4 Analysis 79
6.4.1 Effect of CNT Forest Height 79
6.4.2 Thermal Transport at Polymer Coated CNT Contacts 81
6.5 Summary and Recommendations 84

CHAPTER 7: RESOLVING THE CNT FOREST TIP INTERFACE RESISTANCE WITH TIME-DOMAIN THERMOREFLECTANCE 85

7.1 Introduction 85
7.2 TDTR of CNT Forest Contacts 86
7.2.1 Samples 86
7.2.2 Measurement Strategy 87
7.2.3 Data Fitting 88
7.3 Measurement Sensitivity and Uncertainty 89
7.4 Results 91
7.4.1 Glass-Al Interface Results 91
7.4.2 Glass-Al-CNT Forest Interface Results 94
7.5 Limitations of the Bi-Directional Sample Configuration 99

7.6 Summary and Recommendations 101
7.6.1 Summary 101
7.6.2 Recommendations 101

CHAPTER 8: SUMMARY AND RECOMMENDATIONS 103
8.1 Summary and Major Findings 103
8.1.1 Chapter 4: Liquid Softening 105
8.1.2 Chapter 5: Pyrenylpropyl Phosphonic Acid Surface Modifier 106
8.1.3 Chapter 6: Polymer Spray Coating and Bonding 107
8.2 Comparison with Existing Bonding Approaches 107
8.3 Recommendations 110

APPENDICES: 112

REFERENCES: 134

LIST OF TABLES

Table 1.1 Thermal resistances of bonded CNT thermal interfaces (2010 and prior) compared to conventional TIMs 6

Table 1.2 Overview of dissertation 10

Table 2.1 Aspects of TIM development 15

Table 7.1 Initial guess values and bounds for data fitting 88

Table 7.2 CNT forest thermal properties. See Appendix D for a more rigorous treatment of the uncertainty in these results using a preliminary Monte Carlo method and additional discussion. 98

Table 8.1 Thermal resistances of bonded CNT forest TIMs compared to conventional TIMs 108

LIST OF FIGURES

Figure 1.1 Heat dissipation in typical flip-chip architecture 2

Figure 1.2 Close-up view of a solid-solid interface illustrating (a) heat conduction across contacting surface asperities, and (b) a thermal interface material (c) temperature profile across the TIM 3

Figure 2.1 Thermal resistance of conventional TIMs 11

Figure 2.2 (a) roll of solder film (b) thermal grease (c) application of thermal grease to a heat spreader........ 12

Figure 2.3 (a) double-sided thermal adhesive (b) thermal pad 13

Figure 2.4 Thermal Contact Resistance Triad illustrating the relationship between factors contributing to thermal contact resistance 22

Figure 2.5 (a) Constriction of heat flow from a half-space to a circular contact of radius a (b) top view showing multiple contacts and flux tubes 23

Figure 2.6 SEM images illustrating the bending of CNT tips to form cylinder-plane contacts with opposing surfaces 28

Figure 2.7 Cylinder-plane contact formed between a CNT tip and opposing substrate. Over the contact area the graphitic planes of the CNT sidewall are oriented parallel to the surface 28

Figure 3.1 SEM image of a CNT forest (left) and TEM image of an individual CNT (right), characteristic of those used in this research 34

Figure 3.2 Raman spectra of a CNT forest, representative of those used in this research, with the with characteristic G and D band peaks used to infer CNT quality 34

Figure 3.3 CNT Forest grown on both sides of a metal foil to create a thermal interposer 35

Figure 3.4 Schematic of the PA system used to measure the total resistance of CNT forest TIMs 36

Figure 3.5 (a) CNT forest properties used to plot (b) the sensitivity of the PA measurement to unknown parameters 38

Figure 3.6 Two theoretical fits to PA data collected on a 10 μm tall CNT forest in dry contact with Ag foil. The total resistance was identifiable with PA, however the component resistances were not. 39

Figure 3.7 Schematic of a two-color TDTR system similar to that used in the NEST lab to characterize CNT forest TIMs 40

Figure 3.8 TDTR sample configuration with a transparent top substrate and bi-directional heat flow a) originally used to measure the thermal conductivity of liquids, b) adapted in this research to characterize bonded/pressed CNT forest contacts 42

Figure 3.9 Side-view schematic of the linear-compression cell used to apply pressure to CNT forest contacts during TDTR measurements............................ 42

Figure 4.1 Illustration of inter-CNT vdW interactions being attenuated by liquid, decreasing the stiffness of the CNT forest, and increasing the contact area (b), over the dry state (a).. 44

Figure 4.2 Capillary induced deformation of CNT forests into cellular structures 45

Figure 4.3 Illustration of capillary forces during evaporation of liquid from a CNT forest pulling a CNT tip into contact with the opposing substrate 46

Figure 4.4 Illustration of the WCD process 1) CNT forest is wet with a liquid, 2) the wet CNT forest is compressed against the opposing substrate, 3) the liquid evaporates from the compressed CNT forest, and 4) the dry structure undergoes thermal or mechanical testing 47

Figure 4.5 (a) Contact angle of 90° formed by water on Ag, and (b) illustration of surface forces acting on a droplet on a surface. The force normal to the surface is proportional to the liquid-vapor surface tension and the sine of the contact angle... 49

Figure 4.6 a) Total thermal resistance of short CNT forests is reduced by ~70 after the WCD process with water or hexane, b) the total thermal resistance of short CNT forests prepared under compressive pressures of 35, 70, 105, and 140 kPa are comparable after the WCD process, c) the total thermal resistance of tall CNT forests was reduced by 30-40% from the WCD process and was unaffected by a thermal bake at 140 ˚C for two hours, and d) shear adhesion of CNT forests to glass at unprecedentedly low pressures is enabled by the WCD process 51

Figure 4.7 Coarse-grain mechanics simulations of CNT forests with reduced inter-CNT van der Waals interactions due to liquid infiltration exhibit enhanced contact area over dry forests 53

Figure 4.8 Top view SEM images of a) short CNT forests, and b) tall CNT forests, before and after the WCD process. The morphology of the short CNT forests remains unchanged, while the tall CNT forest exhibits lateral clumping due to capillary forces during drying. Insets display higher magnification images 56

Figure 4.9 Capillary forces arising during evaporation act predominantly in the lateral direction 57

Figure 5.1 Synthesis of pyrenylpropyl phosphonic acid. **1** iodide precursor, **2** phosphonate, and **3** phosphonic acid 60

Figure 5.2 Modification of CNTs and copper oxide with phosphonic acid. a) Comparison of the UV-Vis spectra of the CNTs, phosphonic acid moiety, and the modified CNTs. b) XPS survey spectra of the modified and unmodified copper substrate 61

Figure 5.3 Sample and photoacoustic measurement configuration. a) Representative SEM image of a CNT forest used for PyprPA interface coupling. b) Photoacoustic measurement configuration (left) used to measure the thermal resistance of CNT forests coupled to oxidized Cu surfaces with the PyprPA modifier (right) 62

Figure 5.4 Photoacoustic characterization of CNT forests in dry contact and PyprPA coupled configurations. a) Coupling the CNT tip interface with the PyprPA modifier reduces the thermal resistance of the interface material by 85–75% on average and alleviates the pressure dependence. Error bars include measurement uncertainty and variations in thermal resistance from multiple measured samples. b) A representative photoacoustic measurement data set for a PyprPA coupled CNT forest, including theoretical curve fits to the data and to data sets shifted by the measurement uncertainty of ±1 degrees (solid lines) 63

Figure 5.5 Effect of solvent on thermal resistance at 7 kPa. Coupling the interface with solvent and a monolayer of PyprPA increases the contact area and enables the formation of additional π-π bonds with the PyprPA:CuO. Results shown for the Solvent-Only configuration were collected before delamination occurred 65

Figure 5.6 a) TGA of PyprPA modified and unmodified loose CNTs showing a 22% mass loss that commenced at 200 °C. b) Normal attachment strength of PyprPA coupled interfaces was measured through a tensile failure mode to be 340 ± 50 kPa 67

Figure 5.7 a) Sample configuration for 2-probe electrical characterization of CNT-PyprPA:CuO coupled interfaces. b) Current-voltage scan illustrating a

~90% reduction in electrical resistance for PyprPA coupled interfaces over dry contact interfaces ... 68

Figure 5.8 (a) Benzene-BisPA, (b) Octane-BisPA modifiers used in Strategy 1; (c) Strategy 2 ... 70

Figure 6.1 Airbrush used to deposit nanoscale polymer coatings onto CNT forests ... 72

Figure 6.2 Illustration of the polymer spray coating and bonding process. (1) Spray deposition of polymer onto the top of the CNT forest. (2) The polymer coating dries, causing clumping of the CNT tips. (3) Solvent (CHCl3) is applied to the top of the CNT forest to wet and reflow the polymer coating. (4) Still wet polymer coating is brought into contact with Ag foil and placed under 140 kPa of pressure for 5 h while the interface dries ... 74

Figure 6.3 SEM images of bare and polymer spray coated CNT forests. The spray coating process deposits nanoscale coatings of polymer to the tips and sides of the CNT forest. The amount of polymer visible on the CNT forests increases with the number of sprays. No morphological differences were observable between PS and P3HT. (c) and (e) were spray coated with P3HT, and (d) and (f) were spray coated with PS ... 74

Figure 6.4 SEM images of a polymer (a) dip coated, and (b) spray coated CNT forest showing that spray coating reduces capillary driven clumping of CNTs. Clumping due to capillary forces in dip coated samples leads to CNT tear out at the growth substrate ... 75

Figure 6.5 TEM image showing a P3HT chain wrapped around a CNT ... 76

Figure 6.6 (a) Thermal resistance of polymer coated and bare CNT arrays in dry contact. (b) Thermal resistance of PS bonded interfaces (PA cell pressure = 7 kPa) compared to the dry contact interfaces (PA cell pressure = 140 kPa). (c) Thermal resistance of P3HT bonded interfaces (PA cell pressure = 7 kPa) compared to dry contact interfaces (PA cell pressure = 140 kPa). (d) Thermal resistance of polymer bonded samples before and after being baked at 130 °C for 110 h ... 77

Figure 6.7 Schematic of the die shear apparatus and sample configuration used to measure the shear attachment strength of polymer spray coated and bonded interfaces 79

Figure 6.8 SEM images comparing the surface roughness of short and tall CNT forests. (a) Top view of a 5 μm tall forest, and (b) top view of a 70 μm tall forest ... 80

Figure 6.9 (a) SEM image of the top of a CNT forest after one spray of P3HT and bonding. (b) SEM image of the top of a CNT forest after five sprays of

P3HT and bonding. (c) and (d) Illustrations of CNT dry contact and polymer bonded contact configurations respectively and the associated thermal resistance network 82

Figure 7.1 Sample configuration for (a) PA and (b) TDTR of CNT forests 86

Figure 7.2 Representative TDTR data and best-fit solution for a Glass-Al sample 92

Figure 7.3 Sensitivity plots for Glass-Al at a) 3.6 MHz, and b) 1.2 MHz, showing equal sensitivity to thermal conductivity and heat capacity and relatively low sensitivity to the Glass-Al interface resistance 92

Figure 7.4 TDTR data at (a) 3.6 and (b) 1.2 MHz for Glass-Al and Glass-Al-Dry Contact CNTs are indistinguishable, indicating that the differences in interface resistance for these sample types cannot be resolved with TDTR at the modulation frequencies used 93

Figure 7.5 Actual Glass-Al-Dry Contact CNT data compared to theoretical Glass-Al-CNT data at 3.6 MHz with varying Al-CNT interface resistances illustrating the resolution of TDTR for characterizing dry contact CNT forests 94

Figure 7.6 (a) Representative Dry and WCD CNT data at 3.6 MHz illustrating the shift in the signal associated with the WCD process. (b) TDTR data at 3.6 MHz for bonded CNT interfaces is indistinguishable, indicating that the differences in interface resistance for these sample types cannot be resolved with TDTR at the modulation frequencies used 95

Figure 7.7 Representative three frequency data fit for P3HT bonded CNTs 96

Figure 7.8 TDTR Data for Glass-Al-PyprPA bonded CNTs and theoretical fits with fixed Al-CNT interface resistances at 6.3 MHz used to determine the measurement resolution for characterizing bonded CNT forests 97

Figure 7.9 TDTR measurement sensitivity to CNT properties as a function of the effusivity of the backing substrate 101

Figure 8.1 Ratio of the CNT free tip contact resistance to the total resistance after processing with the methods developed in this research, illustrating the diminished role of the contact resistance. The CNT free tip resistance is set to 0.5 mm2-K/W and the growth substrate resistance to 1 mm^2-K/W 104

NOMENCLATURE

Symbol	Parameter [units]
R	area specific thermal resistance [mm^2-K/W]
k	thermal conductivity [W/m-K]
L	bond-line thickness [m]
A	contact area [m^2]
τ	transmission coefficient
ω	angular frequency [rad/s]
q	heat flux per unit area [W/m^2]
D	density of states
T	temperature [K]
$\hbar$	planck's constant / 2π [J-s]
υ	velocity [m/s]
θ	zenith angle [rad]
φ	azimuthal angle, phase shift [rad]
j	phonon mode index
κ_B	boltzmann constant [J/K]
ρ	density [kg/m^3]
Γ	hemispherical transmissivity
ψ	depth parameter
a	contact radius [μm]
b	flux tube radius [μm]
F	constriction alleviation factor

n	number of contacts
K	spring constant [N/m]
C	heat capacity per unit volume [J/kg-m^3]
Kn	knudsen number
λ	phonon mean free path [m]
t	time [s]
δ	thermal penetration depth [m]
α	thermal diffusivity [m^2/s]
P	pressure [Pa]
E	modulus of elasticity
f	force [N]
r	CNT contact half width [m]
d	CNT diameter [m]
t	distance: depth or thickness [m]
σ_r	CNT forests resistance to compression [Pa]
Φ	volume fraction of CNTs in the forest
B	effective bulk compressive modulus [Pa]
S	sensitivity coefficient
V	voltage [μV]
p	alternate parameter in model [designated]
δ	uncertainty in a parameter [designated]
Δ	TDTR signal difference
e	thermal effusivity [J/m^2-K-s$^{1/2}$]

Frequently Used Abbreviations

TIM	thermal interface material
CTE	coefficient of thermal expansion
CNT	carbon nanotube
MWCNT	multiwall carbon nanotube
TBR	thermal boundary resistance
AMM	acoustic mismatch model
DMM	diffuse mismatch model
SEM	scanning electron microscope
TEM	transmission electron microscope
PA	photoacoustic
TDTR	time-domain thermoreflectance
FDTR	frequency-domain thermoreflectance
WCD	wet-compressed-dried
vdW	van der Waals
PyprPA	pyrenylpropyl phosphonic acid
UV-vis	ultraviolet-visible
XPS	x-ray photoelectron spectroscopy
TGA	thermogravinometric analysis
BisPA	bisphosphonic acid
PS	polystyrene
P3HT	poly(3-hexylthiophene)

SUMMARY

The continued miniaturization and proliferation of electronics is met with significant thermal management challenges. Decreased size, increased power densities, and diverse operating environments challenge the limitations of conventional thermal management schemes and materials. Thermal interface materials (TIMs) that are used to enhance heat conduction and provide stress relief between adjacent layers in an electronic package must be improved. Forests comprised of nominally vertically aligned carbon nanotubes (CNTs), having outstanding thermal and mechanical properties, are excellent candidates for next-generation thermal interface materials (TIMs). However, despite nearly a decade of research, TIMs based on vertically aligned CNT forests have yet to harness effectively the high thermal conductivity of individual CNTs. One of the key obstacles that has limited the performance of CNT TIMs is the presence of high thermal contact resistances between the CNT free ends and the surfaces comprising the interface. A related limitation is that accurate measurement of theses resistances is challenging. The aim of this research is to better understand the mechanisms by which the thermal contact resistance of CNT forest thermal interfaces can be reduced through combined synthesis and measurement, and to use this understanding towards the design of effective TIMs and scalable processing methods.

Contact area and weak bonding between the CNT tips and opposing surface are identified as factors that contribute significantly to the thermal contact resistance. Three strategies are explored that utilize these mechanisms as instruments for reducing the contact resistance; *i)* liquid softening, *ii)* bonding with surface modifiers, and *iii)* bonding with nanoscale polymer coatings. All three strategies are found, using detailed custom thermal metrology, to reduce the thermal contact resistance at the CNT forest tips to below 1 mm^2-K/W, a value to where it is no longer the factor limiting heat conduction in CNT forest TIMs. These strategies are also relatively low-cost

and amenable to scaling for production when compared to existing metal-based bonding strategies.

Liquid softening of CNT forests is demonstrated as a method to enhance the contact area at the CNT forest tip interface by as much as ~80%. In the process the CNT forest is infiltrated with a liquid, compressed in the interface, and allowed to dry. Infiltrating the CNT forest with a liquid diminishes inter-CNT van der Waals (vdW) interactions within the forest, effectively reducing its stiffness. By then compressing the forest in the wet state the CNT forest more readily deforms leading to increased contact area between the free tips and opposing surface. The contact area enhancement achieved with this approach is found to reduce the total thermal resistance of the interface by as much as ~80% and to facilitate excellent dry shear adhesion of CNT forests, as high as 24 N/cm^2, at unprecedentedly low compressive pressures, 35 kPa.

Surface modifiers are demonstrated as a highly controlled effective approach for replacing the weak vdW interactions between the CNT tips and a surface. Using a pyrenylpropyl phosphonic acid surface modifier the vdW interactions between the CNT tips and a metal oxide surface are replaced with stronger covalent and π-π stacking interactions. In doing so the thermal and electrical contact resistance at the CNT forest tips is reduced by 9-fold.

Nanoscale polymer coatings are deposited onto CNT forests using a spray coating procedure. The spray coating procedure restricts the polymer deposition to the outer surfaces of the CNT forest, thereby preserving the internal microstructure (vertical alignment). Rewetting and bonding CNT forests with coatings of the polymers - polystyrene and poly(3-hexylthiophene) - is observed to decrease the total thermal resistance of CNT forests to levels comparable to conventional solder TIMs. The polymer coatings reduce the thermal resistance by locally increasing the contact area at individual CNT tip contacts.

CHAPTER 1

INTRODUCTION

1.1 Motivation

The continual miniaturization and proliferation of electronics is met with significant thermal management challenges [1-6]. Insufficient heat removal from devices can lead to reduced performance, accelerated degradation, and even premature device failure. Despite tremendous technological advancements in electronic devices and the advent of several of promising thermal management concepts, most practical thermal management schemes have changed little over the past several decades. Limitations on size, cost, and available power have necessitated that the vast majority of applications remain air-cooled. In most conventional packaging architectures, heat is dissipated from the device through several layers of packaging to an eventual heat sink or heat spreader where it is dumped to the ambient via forced convection, as in the case of servers and desktop computers, or by natural convection in handheld devices. Figure 1.1 shows a typical flip-chip packaging architecture for a processor in a desktop computer or server. There are two primary impediments to heat transfer from the processor device, or die, to the ambient in such packaging schemes: *i)* the thermal resistance of the heat spreader/sink, and *ii)* the thermal resistance of the multiple interfaces along the path of heat transfer [7]. Because heat-sink technology is relatively mature, most emerging thermal management strategies, including microchannel heat sinks, thermoelectric coolers, and flat heat pipes [8], replace heat sinks within the package. In emerging and especially in conventional thermal management schemes reducing the thermal resistance at the interfaces presents a significant opportunity for improving heat dissipation from the package. The aim of thermal interface materials (TIMs) is to enhance heat transfer across the interfaces, and mitigate this bottleneck to effective heat dissipation. Carbon nanotube forests are promising candidates for high-performance TIMs that could both enhance

heat dissipation and improve thermomechanical reliability, enabling the continued advancement of electronics.

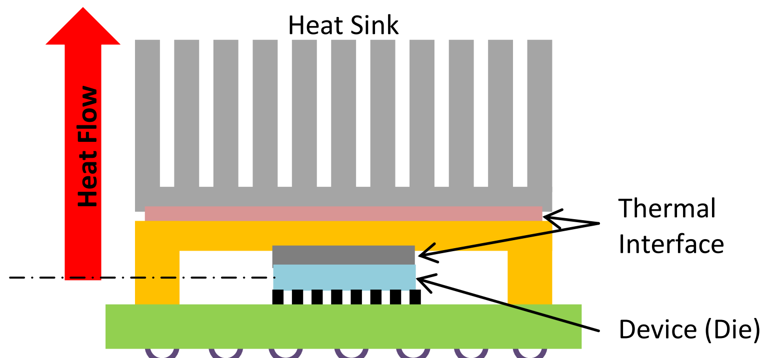

Figure 1.1: Heat dissipation in typical flip-chip architecture [9].

1.2 Thermal Interface Materials

Figure 1.2(a) shows a close-up view of an interface to illustrate the micro- or nanoscale surface features of the two solids comprising the interface. The root-mean-square roughness and peak-to-valley asperity heights for polished heat sink or heat spreader surfaces in contact with a die typically range from ~ 0.1 to 10 μm [10], depending on the surface preparation technique. Both roughness parameters for polished Si dies are on the scale of one to tens of nanometers [11] and can in many cases be neglected compared to the roughness of the heat-dissipating device. However, roughness between a heat spreader and heat sink in a multi-interface stack can be of the same order. Because of surface roughness, the real contact area at the interfaces is usually less than 1% of the apparent area [12]. Heat transfer across the interface is generally dominated by heat conduction between contacting surface asperities since the thermal conductivity of the air filled gaps is only ~0.02 W/m-K [13]. Heat transfer by radiation could be significant in applications at very high temperatures. A number of excellent summaries on the mechanics of contact and thermal resistance at solid-solid interfaces are available [12, 14, 15]. A TIM is added

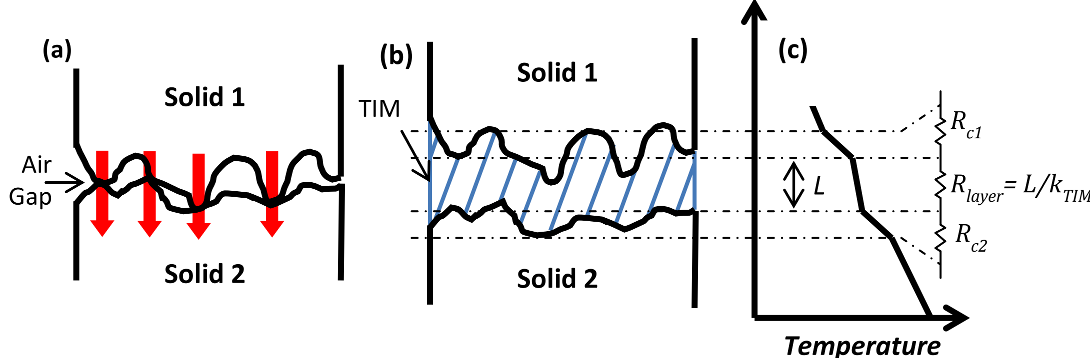

Figure 1.2: Close-up view of a solid-solid interface illustrating **(a)** heat conduction across contacting surface asperities, and **(b)** a thermal interface material. **(c)** Temperature profile across the TIM [9].

to the interface to reduce the thermal contact resistance, as shown in Figure 1.2(b). TIMs reduce the thermal contact resistance by filling the interstitial air gaps with a thermally conductive material. Approximating the heat transfer across the TIM as one-dimensional it can be modeled using a thermal resistance network, analogous to an electrical circuit, and is shown in Figure 1.2(c). In this model, the total thermal resistance of the interface, R_{Tot} is given as the sum of the component resistances

$$R_{Tot} = R_{c1} + L/k_{TIM} + R_{c2}, \tag{1.1}$$

where R_{c1} and R_{c2} are the thermal contact resistances at each side of the TIM [mm^2-K/W], L is the thickness of the TIM [μm], typically referred to as the bond-line thickness, and k_{TIM} is the thermal conductivity of the TIM [W/m-K]. Depending on the physical characteristics of the TIM and adjacent packaging materials, one or all the component resistances can significantly contribute to the total resistance. A detailed summary of the mechanisms contributing to thermal contact resistance is provided in section 2.2.

Although the primary function of a TIM is to enhance thermal transport across the interfaces in a package, other factors relating to the TIMs installation and long-term reliability are also important. It is typically necessary for a TIM to be mechanically compliant in order to

alleviate stresses arising from differences in the coefficient of thermal expansion (CTE) of adjacent packaging components. Semiconductors, i.e. electronic devices, typically have linear CTEs from 1-5 μm/m-K, whereas metals, i.e. solders, heat spreaders, and heat sinks generally have CTEs an order of magnitude larger, 10-25 μm/m-K. A significant bond-line thickness is usually required to accommodate thermal expansion of the substrates without degrading the TIM. This thickness scales proportionally to the modulus of the TIM [16] – thus metallic TIMs usually require much thicker bond lines than polymers, gels, or grease. Additional requirements that are also commonly placed on TIMs include, but are not limited to; chemical stability at high temperatures, electrical isolation of the device from packaging, the mechanical joining of packaging components, ability to be reworked, and low cost. Ultimately, the properties required of a TIM depend on the application. The desired attributes for TIMs in assorted applications can be found in references [9, 17]. A survey of these applications shows that there is especially a need for mechanically compliant TIMs with very low thermal resistance (< 10 mm^2-K/W), and chemical stability at elevated temperatures (> 130 °C).

1.3 Carbon Nanotube Forest TIMs

Forests comprised of nominally vertically aligned carbon nanotubes have several attributes that are attractive for advanced TIMs. Most notably, carbon nanotubes have been theorized to possess the highest thermal conductivity of any known material [18, 19]. Theoretical and experimental studies have reported single tube thermal conductivities from ~200 W/m-K for highly defective multiwall CNTs to as high as 6600 W/m-K for single-wall CNTs [20-24]. Despite having a high modulus of elasticity, nearing 1 TPa [25], an order of magnitude larger than that of steel, individual CNTs can be grown to aspect ratios in excess of 10^6 making them exceptionally flexible and candidates for accommodating large differences in substrate CTE. Furthermore, well-graphitized CNTs can be chemically stable up to approximately 700 °C in air, suitable for high-temperature or harsh environment applications [26]. TIMs based on forests of nominally

vertically aligned CNTs attempt to exploit these attractive properties and the preferential alignment of individual CNTs within the forest.

It wasn't until the mid 2000's that chemical vapor deposition (CVD) methods had been sufficiently developed to produce dense vertically aligned CNT forests with heights on the order of micrometers, enabling the first studies of CNT forest TIMs [27-29]. In 2006 Xu and Fisher [30] measured the thermal resistance of multi-wall CNT forests 10-15 μm in height on Si substrates using a 1D reference bar apparatus. They reported total thermal resistances as low as 19.8 mm^2-K/W at 445 kPa of applied pressure. While their measurement technique didn't permit resolution of the contact and layer resistances, calculations of the layer resistance based on current data for CNT forest thermal conductivities suggested that the total thermal resistance was dominated by the resistance of the contacts. Shortly thereafter, Hu et al. [31] measured the thermal conductivity and thermal contact resistance of CNT forests in dry contact with a SiN passivation layer using the three omega method. The thermal contact resistance between the CNT tips and the passivation layer was found to be prohibitively high, ~15 mm^2-K/W at an applied pressure of 100 kPa. Subsequent studies by Tong et al. [32] and Cola et al. [11] using phase sensitive thermoreflectance and photoacoustic measurement techniques respectively confirmed that the thermal resistance of CNT forest TIMs of modest height (< 50μm) is dominated by the thermal contact resistance between the CNT tips and the opposing substrate.

Accordingly, the majority of research on CNT forest TIMs has since focused on developing methods for bonding the free ends of the CNTs to the interface to mitigate the contact resistance [32-35]. The majority of these efforts have utilized metal films to join the CNT tips to the opposing surface under high pressure and temperature. A few of the more successful bonding methods that were developed prior to the onset of this research, though 2010, are summarized in Table 1.1, alongside several conventional TIMs for comparison. An updated table, including the methods developed as part of this research, is given in Chapter 8. While many of the methods

Table 1.1 Thermal resistance of bonded CNT forest TIMs (2010 and prior) compared to conventional TIMs

Interface	CNT Forest Height [μm]	Measurement Pressure [kPa]	Thermal Resistance [mm^2-K/W]	Implementation Process
Bonded CNT Forests:			**Bonded/Dry Contact:**	
Si-MWCNT-In-SiO_2[32]	10	0	$R_{CNT\ tips} \approx R_{total}$: ~1/11	Metal Evaporation, Bonding (Pressure NA[a], 180 °C)
Si-MWCNT-Au-Ag[34]	30	0	R_{total}: 4.5/NA[a]	Metal Evaporation, Bonding (Pressure NA[a], 220 °C)
Si-Au-Patterned MWCNT-Au-Si[35]	~60	63	R_{total}: 62/336[b]	Metal Evaporation, Bonding (63 kPa, 150 °C)
Cu-MWCNT-Si[33]	NA	0	R_{total}: 10/50	Spin Coating, Microwave Bonding (6.425 GHz, 750 kPa, 160 °C)
Conventional Materials [17]:				
Greases			20-100	
Gels			40-80	
Pads			100-300	
Phase Change			30-70	
Solder			5	

[a] NA: Data not available [b] The reported area specific thermal resistances were recalculated using the total area of the interface (4 mm^2) instead of only the patterned CNT area (1.13 mm^2) to reflect the effective thermal resistance, as would be experienced by a real device

have produced TIMs with thermal resistances that are comparable to conventional metallic solder TIMs (5 mm^2-K/W) [36], they are generally challenging to implement consistently, or require cumbersome processing. Specifically, Tong et al. [32] using indium to weld multiwall CNT (MWCNT) tips to glass noted that while thermal resistances on the order of 1 mm^2-K/W were measured, the thermal resistance across the entire area of the sample varied significantly, a result they attributed to inconsistent bonding at the interface. Several authors [34, 35, 37] have coated both MWCNT tips and the surface of the interface with films of Au and diffusion bonded the MWCNT tips under high temperature and pressure to produce resistances as low as ~ 4 mm^2-K/W. However, unlike bonding with In or other solders, Au does not melt and reflow during the bonding process and is instead restricted to diffusing between contacting surface asperities,

limiting the contact area and making it difficult to achieve adequate bonding. As stated by Wasniewski et al. [37], Au diffusion bonding "results proved very difficult to replicate; challenges with achieving strong, uniform diffusion bonds… precluded positive test results." The remaining approaches summarized in Table 1.1 similarly produced either relatively high thermal resistances (over 5 mm^2-K/W), and/or required processing that could not be scaled in a practical manner. The method developed by Lin et al. [33] to chemically modify and anchor MWCNTs to Si substrates includes spin coating followed by a two-stage microwave bonding process lasting 1.5 hours with a peak temperature and pressure of 160 °C and 750 kPa respectively. As such, there remains a significant need for a method of bonding CNT free ends that can repeatedly produce low thermal contact resistances uniformly over device areas, 1-4 cm^2, with minimally harsh and scalable processing.

Despite the development of multiple bonding methods, their effect on the transport physics is rarely discussed and is overall not well understood. Thermal transport at interfaces in general is a complex problem. Phonon transmission for the simplified case of planar interfaces is dependent on many parameters including the phonon density of states of the materials and the nature of the chemical bonding at the interface. For the case of CNT forests the sheer number, nanometer scale, and variability of the free tip contacts greatly complicates the problem. While simplified analytical [38-40] and computational [41-43] models have been developed to describe thermal transport at individual CNT contacts, and are reviewed in 2.3, physical interpretation of contact resistance data at the scale of an entire CNT forest interface has been met with limited success [44-46]. This is especially true for the case of bonded CNT forest TIMs since it is often unknown how the bonding affects the, the final interface chemistry, transport physics, CNT tip morphology, and contact area. To develop effective methods for reducing the thermal contact resistance of CNT forest TIMs the physical mechanisms by which bonding methods enhance thermal transport and their capacity for doing so must be better understood.

1.4 Objectives and Overview

In this research I explore alternative methods of bonding CNT forests as TIMs with three objectives in mind; *1)* understanding the physical mechanisms by which the bonding methods reduce the thermal contact resistance, *2)* identifying the merits and limitations of each method, and *3)* identifying methods that are effective over device sized areas and amenable to scaling for commercial production. A graphical overview of the specific bonding methods evaluated in this research is given in Table 1.2 below. The findings of this work are anticipated to have implications for electrical applications of CNTs, CNT forest gecko-mimetic adhesives, and other applications of nanoscale filamentary materials.

The contents of this dissertation are organized as follows:

Chapter 2: provides relevant background information on conventional thermal interface materials, the physical mechanisms contributing to thermal contact resistance at interfaces and theoretical frameworks used to describe it, and a discussion of thermal transport at CNT forest contacts.

`*Chapter 3:* reviews the experimental methods utilized in this research, including; the CNT forest synthesis procedure and methods used to measure the thermal resistance of CNT forest TIMs.

Chapter 4: investigates infiltrating CNT forests with liquid as a mechanism to enhance contact area at the free tips. Specifically, this chapter examines the interplay between inter-CNT van der Waals interactions, the bulk stiffness of the forest, and the contact area at the free tip interface. The possibility of capillary driven contact area enhancements resulting from the evaporation of the liquid is also studied.

Chapter 5: explores surface modifiers as a method for enhancing bond strength at CNT forest contacts. The effect of the surface modifiers on the thermal contact resistance, normal adhesion, and electrical resistance of CNT forests is experimentally studied.

Chapter 6: examines the use of nanoscale polymer coatings as a material for bonding CNT forests in a scalable and low-cost manner. The influence of polymer chemistry and quantity on thermal resistance is examined for CNT forests of assorted heights.

Chapter 7: time-domain thermoreflectance is utilized to determine the specific contribution of the CNT forest tip interface to the total thermal resistance. The capabilities and limitations of the method for characterizing bonded or pressed contacts are established.

Chapter 8: concludes the dissertation by examining the broader implications of this research for CNT TIMs.

Table 1.2 Overview of the dissertation.

Topic	Methods	Major Results	Chapter
Liquid softening	• Photoacoustic • Die Shear	• Contact area explicitly identified as a major contributor to the thermal resistance of CNT forest contacts • By compressing CNT forests in the wet state the contact area at the free tips can be increased by ~80% • Wet compression facilitates record approaching shear adhesion, 10-24 N/cm^2, at an order of magnitude lower preload, 35-105 kPa	4
Enhancing bond strength with surface modifiers	• Photoacoustic • 2-probe electrical	• Bond strength explicitly identified as a major contributor to the thermal resistance of CNT forest contacts • Replacing van der Waals interactions at CNT contacts with covalent and π-π bonds can reduce the thermal contact resistance (and electrical) by > 80% repeatedly over device-sized areas	5
Bonding with nanoscale polymer coatings	• Photoacoustic	• Spray coating demonstrated as a method for applying nanoscale coatings of soluble materials to the surfaces of CNT forests, while preserving the internal microstructure of the forest • Bonding of CNT forests with polymers at room temperature and low pressure (140 kPa) reduced the thermal resistance of the CNT forest tip interface by as much as ~75%, although the process had control/repeatability issues	6
Resolving the resistance of CNT forest contacts	• Time-domain thermoreflectance	• Free tip contact resistance of CNT forests bonded with PyprPA modifier, polymer coatings, and wet compressed < $1 mm^2$-K/W. No longer dominates total resistance	7

CHAPTER 2

BACKGROUND

This chapter aims to provide useful background information for understanding and interpreting this research. It begins with a review of conventional commercial TIMs and highlights their merits and weaknesses. It then transitions to a discussion of the physical mechanisms governing thermal transport at interfaces and the current theoretical frameworks used to describe it. The chapter concludes with a discussion of the transport physics and theory specific to CNT forest tip contacts.

2.1 Existing and Emerging TIMs

2.1.1 Conventional TIMs

Conventional TIMs include metallic solders, greases, adhesives, phase change materials (PCMs), gels, and pads. A brief description of each TIM class and their merits and weaknesses [17, 47, 48] is given below. Figure 2.1 summarizes conventional TIMs based on thermal resistance and Figure 2.2 displays a few conventional TIMs.

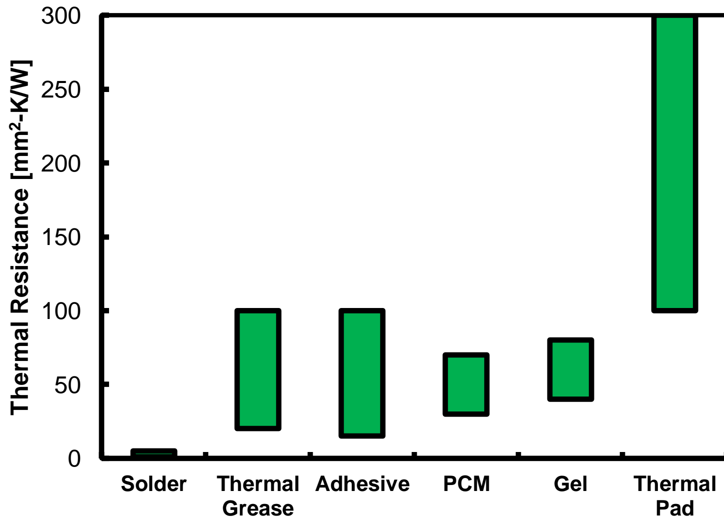

Figure 2.1: Thermal resistance of conventional TIMs [9].

Solder: Solder joints are comprised of low melting point metals such as In or Sn in either pure form, or as a component of an alloy. For implementation, solder is placed into the interface under pressure, heated above its melting point, and cooled. In the molten state, solder is readily able to conform to asperities in the interface. Voiding is a concern for reliability. Also, the relative high cost and complexity of implementation typically restricts use to applications requiring low resistance.

Greases: Thermal greases, commonly referred to as pastes and compounds, consist of a low-cost spreadable polymer for maximizing contact area. Greases are typically silicone based and may contain metal, ceramic, or carbon fillers to enhance thermal conductivity. They
can also be messy and challenging to apply uniformly. Long-term concerns include pump-out and dry-out.

Figure 2.2: **(a)** roll of solder film [49] **(b)** thermal grease [50] **(c)** application of thermal grease to a heat spreader [51].

Adhesives: Thermal adhesives come in both solid and liquid forms. In solid form the adhesive is essentially a double-sided tape. In liquid form thermal adhesives are generally epoxy resins and require curing. They may also contain metal, ceramic, or carbon fillers to enhance thermal conductivity. An advantage of adhesives is that they do not require a clamp or alternate form of applied pressure. Thermally induced fatigue and delamination due to CTE mismatch is a concern.

Phase change materials (PCMs): Phase change materials generally consist of paraffin or an alternative polymer matrix embedded with high conductivity metal, ceramic, or carbon particles. The melting point of the matrix is typically low, ~50 °C for paraffin, above which it behaves like a grease. A clamp or alternate source of applied pressure is required.

Gels: Gels are similar to greases in that they are typically silicone based and often contain metallic, ceramic, or carbon particles to enhance conductivity. However, unlike greases, gels are cured after application and behave like a low modulus polymer. Cured gels are generally adhesive, but can be susceptible to delamination.

Pads: Thermal pads consist of an elastomeric material, typically filled with high conductivity metal, ceramic or carbon particles. Pads require a clamp or application of an adhesive. Some advantages of pads include the ability to cut to shape, absorption of vibration, and accommodation of variations in assemblies.

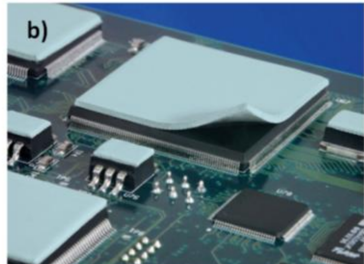

Figure 2.3: (a) double-sided thermal adhesive [52] **(b)** thermal pad [50].

2.1.2 Emerging Nanostructured TIMs

In response to the pressing need for improved TIMs an entire branch of research dedicated to the subject matter has emerged. The vast majority of efforts in this area look to nanostructuring to enable the development of materials with unprecedented properties or combinations thereof, and can be lumped into five main categories; *i)* dispersed nanocomposites *ii)* aligned nanocomposites, *iii)* aligned nanostructure arrays (including polymer and metal), *iv)* aligned

graphite laminates, and *v)* sintered nanoparticle beds. I lead a recent comprehensive review of these emerging nanostructured TIMs that can be found in reference [9]. Although many of these emerging nanostructured TIMs have demonstrated significant advancements over the past several years, none hold the combined potential for extraordinary thermal conductivity, mechanical compliance, and chemical stability as do vertically aligned CNT forests.

2.1.3 Evaluating TIM Performance

TIMs must ultimately be tested in their application to conclude their merits [53, 54]. During earlier stages of development, however, several standard tests are usually employed to evaluate key TIM performance metrics (introduced in section 1.2). These include assessments of thermal resistance (of a bonded TIM or as function of applied pressure), mechanical attachment strength, and thermal and environmental chemical stability, and reliability. Table 2.1 below illustrates these facets of TIM development. The thermal resistance of TIMs can be measured using numerous methods [9], although standardized methods, including the ASTM D5470 [55] are typically used in industry. The mechanical attachment strength of TIMs is typically measured through a shear failure mode using a die shear apparatus, although other tensile and flexure-based methods exist. The thermal stability of TIMs is typically evaluated by baking at high temperature for extended periods of time, as shown in Table 2.1. The thermal resistance of the TIM before and after the high temperature exposure is usually measured to assess any degradation in performance. The reliability of TIMs is generally concerned with the long-term chemical and mechanical stability of the TIM within package due to extended use. Therefore, reliability is usually assessed by cycling the entire package from low to high temperatures many times to simulate the lifetime of a device. Examples of unreliable TIM performance include cracking/delamination of the TIM from the package, voiding as in the case of solders, or thermally driven flows that excrete the TIM from the interface (referred to as pump-out). An equally important aspect of TIM performance is referred to as the rework-ability of the TIM, i.e. the ease with which the TIM can be implemented, removed, and reinstalled in the package. This

aspect of TIM performance is assessed qualitatively, although it can typically be related to quantitative metrics such as the time or cost required to rework the TIM.

Table 2.1 Aspects of TIM development

	Thermal Resistance	Mechanical Attachment	Thermal Stability	Reliability	Rework
Method:	Assorted Metrologies	Die Shear	Thermal Bake	Thermal Cycling	Qualitative

2.2 Thermal Transport at Contacts and Interfaces

This section provides a more detailed description of the fundamental factors contributing to thermal contact resistance. It is these physical mechanisms that necessitate the use of a TIM and should be used to guide their design. We begin by discussing thermal transport between dissimilar materials in the ideal case of a planar interface with perfect contact. We then add the complexity of surface roughness and imperfect contact area and finish by discussing additional impediments to thermal transport that occur when the contact sizes approach nanoscale dimensions. The emphasis throughout this discussion will remain on analytical developments, although, because of advancements in computational resources, molecular dynamics and other simulation methods are becoming increasingly useful tools for studying interfacial thermal transport.

2.2.1 Thermal Transport between Dissimilar Materials

To begin we consider the case of perfect contact area between dissimilar materials. A scenario that closely approximates solid-liquid interfaces, like those observed in cryogenics, as well as

solid-solid interfaces, such as those between an evaporated metal film and its substrate. For simplicity and generality we first discuss the case of a planar atomically perfect interface between two semi-infinite materials. Furthermore, we will restrict the scope of the discussion to only consider phonon transport, i.e. the case when at least one of the two materials is an insulator, although similar mechanisms are of consideration for materials where electrons contribute significantly to interfacial thermal transport. For this ideal case, and for situations in which surface roughness effects are limited, the thermal resistance of an interface is typically referred to as thermal boundary resistance (TBR), or in the case of solid-liquid interfaces the Kapitza resistance [56]. Phonons incident on this ideal interface will "*scatter*" due to the differences in the vibrational properties (mass, atomic structure, the phonon density of states, etc.) between the two materials, and can either be transmitted through the interface or reflected. Only a fraction of the incident phonons will transmit through the interface amounting to a thermal boundary resistance. The probability of a phonon transmitting from side 1 to side 2 is designated as the transmission coefficient $\tau_{1\to2}$. In general, the transmission coefficient is dependent on the phonon mode, wave vector, frequency, and temperature. Neglecting the temperature dependence of the transmission coefficient and considering the materials on either side of the interface to be isotropic the heat flux emanating from side 1 into side 2 is given by

$$q_{1\to2} = \frac{1}{4\pi}\sum_{j}\int_{0}^{2\pi}\int_{0}^{\frac{\pi}{2}}\int_{0}^{\omega_{1max}} \tau_{1\to2}(\omega,\theta,j)D_{1,j}(\omega,T_1)\hbar\upsilon_{1,j}\cos\theta\sin\theta\, d\omega d\theta d\varphi, \qquad (2.1)$$

here j is an index for the phonon mode, ω is the phonon frequency, $D_{1,j}$ is the product of the phonon density of states and the Bose-Einstein distribution, υ is velocity, θ is the zenith angle (between the interface normal and the direction of phonon propagation), and φ is the azimuthal angle [57]. The net heat flux across the interface is given by the difference between $q_{1\to2}$ and $q_{2\to1}$ and the thermal boundary resistance, R_{bd}, by

$$R_{bd} = (T_1 - T_2)/(q_{1\rightarrow 2} - q_{2\rightarrow 1}), \tag{2.2}$$

where T_1 and T_2 are the temperatures of incoming phonons on the respective sides of the interface. In reality, appropriate definition of these temperatures in nontrivial, but will not be considered here [57-59]. Determination of the transmission coefficients and boundary resistance is a complex problem and in most cases to date is intractable. And we are still considering an idealized and simplified interface! However, with additional simplifying assumptions the transmission coefficients can be obtained. Two such reductions that have proved to be very useful are the acoustic mismatch model (AMM) [58, 60] and the diffuse mismatch model (DMM) [57]. While these two models do not accurately represent most real interfaces, they are often useful for comparison with data. In the subsequent formulations of the AMM and DMM we follow the constructions of references [57, 61].

The Acoustic Mismatch Model: The AMM was originally developed by Khalatnikov in 1952 for solid-liquid interfaces [60] and extended to solid-solid interfaces by Little in 1959 [58]. In the acoustic mismatch model it is assumed that phonon transport within the two materials is governed by continuum acoustics. By invoking this assumption phonons are represented by plane waves in semi-infinite continua joined by a planar interface. With these assumptions the discrete nature of the lattice is neglected and phonon reflection at the interface is perfectly specular and elastic (frequency is conserved), although mode conversion is permitted. The angle of phonon reflection or transmission and the transmission coefficients are governed by the acoustic analogs of Snell's Law and the Fresnel Equations respectively. Even with these simplifications calculation of the transmission coefficients is challenging due to the dependence on the incident angle and the fact that there are three modes. Consequently, the materials are typically assumed to be isotropic and density of states is represented using the Debye approximation. The Debye approximation implies that for frequencies below the Debye frequency

$$D_{1,j}(\omega,T)d\omega = \frac{\omega^2 d\omega}{2\pi^2 v_{1,j}^3[\exp(\hbar\omega/\kappa_B T) - 1]}, \tag{2.3}$$

where $\hbar$ is the Planck constant divided by 2π and κ_B is the Boltzmann constant. In this case the transmission coefficient for a longitudinal phonon mode incident from side 1 without mode conversion is

$$\tau_{1\to 2} = \frac{4\rho_1\rho_2 v_{l1}^2 \cos\theta_1 \cos\theta_2}{(\rho_1 v_{l1}\cos\theta_2 + \rho_2 v_{l2}\cos\theta_1)^2}, \tag{2.4}$$

where ρ is density and the subscript l denotes a longitudinal mode. The polar angles θ_1 and θ_2 are related to the velocities by (Snell's Law): $v_{l2}\sin\theta_1 = v_{l1}\sin\theta_2$. All phonons incident at angles greater than the critical angle, θ_c, on the side of the interface with lower phonon velocity will be reflected. For the case of $v_{l1} > v_{l2}$ the critical angle is given by $\theta_c = \sin^{-1}(v_{l2}/v_{l1})$. To further simplify expressions for the net heat flux across the interface and the TBR, the transmission coefficients are frequently integrated over all incoming angles and expressed as a hemispherical transmissivity

$$\Gamma_{1,j} = \frac{1}{\pi}\int_0^{2\pi}\int_0^{\frac{\pi}{2}} \tau_{1\to 2}(\theta,j)\cos\theta_1 \sin\theta_1 \, d\theta_1 d\varphi = 2\int_0^{\theta_c} \tau_{1\to 2}(\theta,j)\cos\theta_1 \sin\theta_1 \, d\theta_1, \tag{2.5}$$

Recasting Equation 2 the net heat flux according to the AMM for an isotropic Debye solid is given by

$$(q_{1\to 2} - q_{2\to 1}) = \frac{1}{4}\sum_j \frac{\Gamma_{1,j}}{v_{1,j}^2}\frac{\kappa_B^4}{8\pi^2\hbar^3}\left(T_1^4\int_0^{x1}\frac{x^3 dx}{e^x - 1} - T_2^4\int_0^{x2}\frac{x^3 dx}{e^x - 1}\right), \tag{2.6}$$

where $x_i = \hbar\omega/\kappa_B T_i$. Recall that the AMM assumes the interface to be planar and the materials on either side of the interface to be semi-infinite continua. These assumptions are best satisfied when the phonon wavelength is much larger than both the interfacial roughness and the average

interatomic spacing. Therefore, the AMM is typically most accurate for very smooth surfaces at low temperatures. Taking the low temperature limit of Equation 2.6 and assuming the temperature difference across the interface to be small the TBR can be expressed as

$$\lim_{T\to 0}(R_{bd,AMM}) = \frac{30\hbar^3 T^{-3}}{\pi^2 \kappa_B^4 \sum_j \Gamma_{1,j} \upsilon_{1,j}^{-2}}, \tag{2.7}$$

The Diffuse Mismatch Model: For interfaces that are not atomically smooth and/or at temperatures above a few mK the specular behavior of the interface described by the AMM becomes inaccurate as scattering becomes increased. In an effort to incorporate scattering effects into a model for TBR Swartz and Pohl introduced the DMM in 1989 [62]. In contrast with the AMM, where phonon behavior at the interface is perfectly specular, the DMM assumes perfectly diffuse scattering. Swartz and Pohl defined a diffuse scattering event as one in which the wave vector and mode of a scattered phonon are entirely independent of its wave vector and mode upon incidence. The only property correlated to the initial state in a diffuse scattering event is the energy, that is to say that only elastic scattering is considered. Under these assumptions the transmission coefficients are determined by the mismatch in the phonon density of states of the two materials and the principal of detailed balance. Since a diffusely scattered phonon carries with it no recollection of its previous state (with the exception of energy) it is impossible to determine whether it was reflected or transmitted. Therefore, it follows that the probability of it being reflected and the probability of transmitted to its current state must be equal: $1 - \tau_{1\to 2} = \tau_{2\to 1}$ and vice versa. The principle of detailed balance dictates that the number of phonons of frequency ω per unit area per unit time leaving side i is equal to the number of phonons at frequency ω per unit area per unit time leaving the opposite side (3-i):

$$\sum_j \upsilon_{i,j} D_{i,j}(\omega,T)\tau_{i\to 3-i}(\omega) = \sum_j \upsilon_{3-i,j} D_{3-i,j}(\omega,T)[1-\tau_{i\to 3-i}(\omega)], \tag{2.8}$$

where the index i can take on the value 1 or 2 and has been adopted for generality. Equation 2.8 can then be rearranged to solve for the transmission coefficients,

$$\tau_{i\to 3-i}(\omega) = \frac{\sum_j v_{3-i,j} D_{3-i,j}(\omega, T)}{\sum_j v_{i,j} D_{i,j}(\omega, T) + \sum_j v_{3-i,j} D_{3-i,j}(\omega, T)}. \quad (2.9)$$

Invoking the Debye approximation, Equation 2.6 for the net heat flux can again be used; however, in this case the hemispherical transmissivities are obtained through integration of Equation 2.9. In the limit of low temperature the TBR for the DMM can be expressed as

$$\lim_{T\to 0}(R_{bd,DMM}) = \frac{60\hbar^3 T^{-3}}{\pi^2 \kappa_B^4} \frac{\sum_{i,j} v_{i,j}^{-2}}{\sum_j v_{i,j}^{-2} \sum_j v_{3-i,j}^{-2}}. \quad (2.10)$$

Due to the extreme descriptions of scattering in the AMM and DMM and the assumptions implicit to their derivation they seldom predict the TBR of real interfaces [57, 63]. This is especially true for rough interfaces and at temperatures above a few K, where the possibility for multiple scattering events and inelastic scattering is increased. As a result, many attempts have been made to adapt these models to account for certain deficiencies and improve their accuracy. A number of studies have examined using more realistic representations of the density of states [64-66], models that account for both specular and diffuse scattering [67], and incorporating surface roughness [68], which has been experimentally observed to increase the boundary resistance by as much as 15% [69]. However, these approaches are often cumbersome to implement and remain limited in applicability to low temperatures as they still fail to adequately account for more than a single scattering event. In an effort to incorporate near interface scattering and model TBR at noncryogenic temperatures Prasher et al. [70] developed a modified version of the AMM. The model can be used to predict the TBR based on ineleastic scattering processes using material properties as an input. Nonetheless, it still typically underpredicts experimental data, due to the presence of additional non-accounted for scattering processes resulting from the non-ideal structure of real interfaces. When the model is fit to experimental

data by adjusting the scattering parameter good agreement can be obtained. In an effort to account for interfacial mixing and multiple scatterings events Beechem et al. [71] modified the DMM to include an additional "virtual" layer of material at the interface, where the virtual layer represents the mixed region. The boundary resistance of the real interface is then taken as the sum of the boundary resistances between each material and the virtual layer. To calculate the TBR between each material and the virtual layer, the Debye approximation is invoked and the virtual layer is assigned phonon velocities based on the rule-of-mixtures. By using the rule-of-mixtures the extent of mixing can be varied continuously. The transmission coefficients are then calculated using the reduced version of Equation 2.9. To account for the thickness of the virtual layer, and the probability of multiple scattering events within it, the boundary resistances between the materials and the virtual layer are scaled by a dimensionless depth parameter, ψ. The depth parameter represents the ratio of the thickness of the virtual layer to an estimate of the phonon mean free path within the layer. The TBR of the interface is then given by

$$R_{DMM,Tot} = \sum_{j} \psi_j R_{DMM,1\rightarrow VL,j} + \sum_{j} \psi_j R_{DMM,VL\rightarrow 2,j}\,, \tag{2.11}$$

where the boundary resistances at the virtual interfaces are expressed for a single phonon mode to permit different phonon mode velocities in calculation of the depth parameter. This model was found to be within 18% agreement with experimental data for Cr/Si interfaces at room temperature. Unfortunately, the use of the model relies on knowledge of the extent and composition of mixing at the interface.

2.2.2 Thermal Transport between Contacting Surfaces; the Effect of Surface Roughness

Real surfaces are almost never atomically smooth. Therefore, when two surfaces are brought into contact, as is often the situation for nanostructured TIMs, the surfaces typically only contact at discrete points, as is shown in Figure 1.2. The cumulative contact area between the points, i.e. the real contact area, is often well below 2% of the nominal area [72]. As a result, the flow of heat

between the bodies is severely constricted at the contact points. This constriction of heat flow at a microscale contact amounts to a thermal resistance, classically referred to as a constriction, or spreading resistance. The combination of the limited real contact area and the thermal constriction resistance at the contacts manifests macroscopically as thermal contact resistance. Developing theories for thermal contact resistance is a complex problem, as it requires a detailed understanding of the surface topologies, contact mechanics, and heat transfer [12]. To illustrate the interplay between these contributing factors, Yovanovich introduced the concept of the Thermal Contact Resistance Triad, shown in Figure 2.4 [15]. Since the emphasis of this section is on the physical mechanisms contributing to the thermal transport at interfaces, we will limit the scope to a general discussion of the thermal constriction-spreading resistance at a single contact and the extension to the case of multiple contacts for the thermal contact resistance of entire interfaces [14]. The details of the contact mechanics problem, and mechanical-thermal considerations are not discussed, although they are of significance in the design of TIMs. Furthermore, only heat conduction is considered, radiation and convection is ignored.

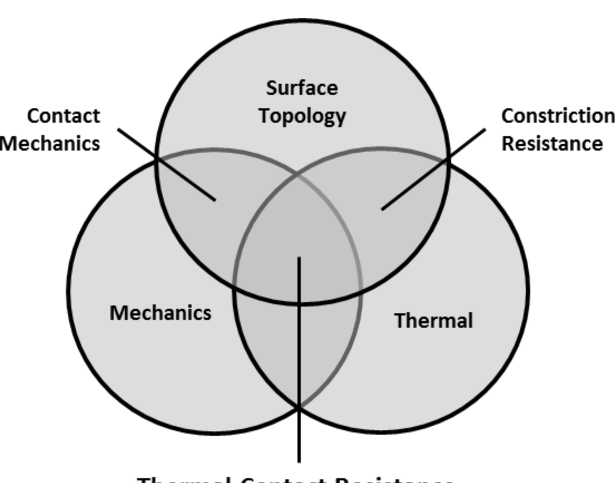

Figure 2.4: Thermal Contact Resistance Triad illustrating the relationship between factors contributing to thermal contact resistance.

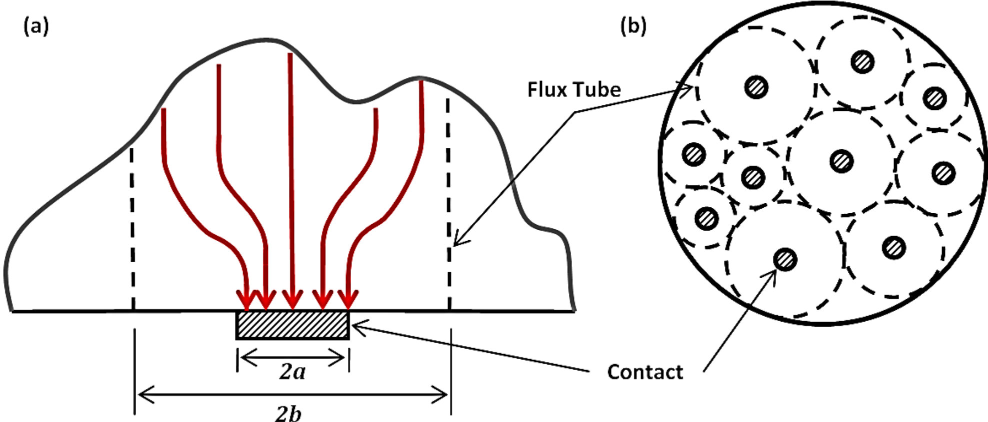

Figure 2.5: **(a)** Constriction of heat flow from a half-space to a circular contact of radius a **(b)** top view showing multiple contacts and flux tubes [9].

Thermal Constriction-Spreading Resistance: When a one-dimensional flow of heat is disrupted by a change in the cross-sectional area the effect of the convergence, or divergence, of the heat flow in the vicinity of the area change can be captured as a thermal resistance, referred to as the constriction or spreading resistance. Constriction-spreading resistances are encountered in a vast number of engineering applications, including thermal contact resistance, and have been studied extensively since the 1950s. Expressions for the constriction-spreading resistance have been formulated for a vast assortment of geometries using analytical, numerical, and experimental methods [14, 72]. For the rather generic case of a circular contact the flow of heat through the contact can be approximated as converging from a larger diameter cylinder, referred to as a flux tube, shown for a single contact in Figure 2.5(a) and for multiple contacts in Figure 2.5(b). Analytical solutions for the heat diffusion in this case are complicated but they have been obtained [73]. The constriction-spreading resistance, $R_{c\text{-}s}$, between the flux tube to the circular contact is given by

$$R_{c-s} = \frac{F(a/b)}{4ka}, \tag{2.12}$$

where F is the constriction alleviation factor, and a and b are radii of the contact and flux tube respectively. The constriction alleviation factor is a function of only the two radii and in the form of an infinite series. Tabulated values for F are available in reference [14]. For contact between two materials the constriction-spreading resistance from sides 1 and 2 can be added in series to give the total constriction-spreading resistance of the contact as

$$R_{c-s} = F/[4ak_1] + F/[4ak_2] = F/[4ak_m], \tag{2.13}$$

where $k_m = 2k_1k_2/[k_1 + k_2]$. The constriction-spreading resistance for n contacts at an interface is then simply the sum of the resistances of the single contacts. If an average contact radius, a_m, is assumed the total constriction-spreading resistance of the entire interface, $R_{c-s,int}$, is

$$R_{c-s,int} = F/[2na_mk_m]. \tag{2.14}$$

Equation 2.14 is coupled to the contact mechanics problem through the parameters n and a_m, and therefore it must be solved before the contact resistance can be calculated. Numerous iterations of the contact mechanics problem for pure elastic, pure plastic, and elastoplastic contacts have been developed and are available in the literature, many of which are featured in the review by Yovanovich [15].

Historically, when solutions to the thermal constriction-spreading resistance have been obtained analytically the effect of thermal boundary resistance was neglected. To illustrate the validity of this assumption, consider the constriction-spreading resistance for a 1μm diameter contact area in a material with a thermal conductivity of 100 W/m-K. Equation 2.12 gives a constriction resistance of approximately 500 to 2000 mm^2-K/W for a/b values of 0.6 and 0.1 respectively. On the other hand, thermal boundary resistance values for assorted metal-dielectric interfaces are on the order of 0.01 mm^2-K/W [74]. As such, the thermal boundary resistance is not a significant factor for contacting rough surfaces.

2.2.3 Additional Impediments to Interfacial Thermal Transport

The structure and strength of the chemical bonding at the interface can also influence thermal transport. The notion that strength of bonding affects transport is longstanding, yet only in the past few years has it been directly studied [75-79]. Losego et al. [79] completed the first systematic experimental study on the relationship between interface bond strength and the thermal boundary resistance in 2012. The terminal group of a self-assembled monolayer (SAM) was varied to create bonding interactions with an Au film that varied from weak van der Waals type interactions to strong covalent bonding. The thermal boundary resistance was observed to decrease ~50% from van der Waals to covalent bonding. The previously presented theories for the AMM and DMM presumed perfect bonding at the interface. In the AMM, perfect bonding was implied through the boundary conditions placed on the interface – continuity in stress and displacement. In an effort to remove this restriction and to incorporate non-ideal bonding, Prasher [78] considered the interface between the two materials to be mediated by a spring, as is often done in non-destructive interface assessment [80]. The transmission coefficient for the modified model is given by

$$\tau_{1\to2} = \frac{4\rho_1\rho_2 v_1 v_2 \cos\theta_1 \cos\theta_2}{(\rho_1 v_1 \cos\theta_1 + \rho_2 v_2 \cos\theta_2)^2 + \left(\frac{\omega}{K}\right)^2 (\rho_1\rho_2 v_1 v_2 \cos\theta_1 \cos\theta_2)^2}, \tag{2.15}$$

where spring constant, K, can be assigned from an interatomic potential or experimentally observed values. In the limit of a perfectly stiff spring, $K\to\infty$, the unmodified AMM is recovered.

For interfaces where the characteristic dimensions of the surface features conducting heat approach the nanoscale additional factors can significantly influence thermal transport. Specifically, simulations of thermal transport at abrupt junctions, such as those between a one or two-dimensional nanostructure and a bulk surface, suggests that phonon coupling to surface modes impedes transport comparably to the mismatch in vibrational characteristics. The result is an additional source of thermal resistance that is present even at junctions between identical

materials [81]. Furthermore, for thermal transport at contacts where the dimension of the contact area is of comparable length scale to the phonon mean free path the transport transitions from being diffusive to ballistic in nature. Prasher [38] developed a simple expression from the DMM to quantify the thermal resistance due to ballistic transport. Assuming the phonon velocities are frequency independent and identical for each mode the thermal resistance due to ballistic effects is

$$R_{ballistic} = \frac{4(C_{l,1}v_1 + C_{l,2}v_2)}{C_{l,1}v_1 C_{l,2}v_2}, \tag{2.16}$$

where C_l is the lattice heat capacity per unit volume. The total thermal resistance of a contact is given by the sum of the constriction-spreading resistance and the ballistic resistance. The relative contributions of each can be indicated by the dimensionless Knudsen number (*Kn*), given by

$$Kn = \lambda/a, \tag{2.17}$$

where λ is the phonon mean free path, and a is the characteristic radius of the contact area. When $Kn >> 1$ the ballistic resistance will dominate the total resistance, whereas when $Kn << 1$ the constriction-spreading resistance will dominate transport. In the intermediate regime, $Kn \sim 1$, both the ballistic and constriction-spreading resistance will contribute to the total thermal resistance of the contact.

Unfortunately, a unifying theory for thermal transport at interfaces that accounts for all of the aforementioned mechanisms does not exist. For the case of CNT forest interfaces the sheer number, nanometer scale, and variable orientation of the free tip contacts further complicates the problem. Nonetheless, several insightful analytical frameworks for thermal transport at CNT forest contacts have been developed and are reviewed in the following section.

2.3 Thermal Transport at Carbon Nanotube Forest Contacts

To describe thermal transport at the CNT forest free-tip interface the contact mechanics problem and heat transfer problem must be addressed at both the scale of an individual CNT contact and at the scale of a CNT forest. Here, overviews of the relevant analytical frameworks for these problems at both scales are presented. These frameworks are revisited in subsequent chapters to analyze several of the processing methods developed.

2.3.1 Thermal Transport at Individual CNT Contacts

The increased horizontal orientation of the CNT tips in the distal crust layer [82, 83], and their propensity to bend under loading [44] causes the majority of CNT tips to lay parallel to the opposing surface, contacting it with their side-walls, as is shown in Figure 2.6. Considering the ideal case of no surface roughness, the contacts can be viewed as cylinder-plane contacts, depicted in Figure 2.7. In this contact-mode the graphite layers comprising the CNT side-wall are oriented parallel to the contact plane, i.e. the surface normal is aligned with the c-axis, across the entire contact area. For this reason, CNT contacts are frequently analyzed as graphite contacts. The CNT forests utilized in this research are grown via a base-growth mechanism and feature closed tips. Therefore, even in the event that a CNT tip should contact the opposing surface perpendicularly or at an intermediate angle, the contact still features graphite planes oriented parallel to the contact plane. Cases where open-ended CNTs are in perpendicular contact the surface, such as the growth substrate have also been analyzed [40, 44], but are not reviewed here since this research is focused on CNT forest free tip interfaces. Due to the abrupt change in area and the nano dimension of CNT contacts constriction-spreading (section 2.2.2) and ballistic effects (section 2.2.3) can significantly influence thermal transport.

As in the generic treatment of interfacial thermal transport, covered in section 2.2, to describe the heat transfer at a CNT contact it is essential to determine the contact area.

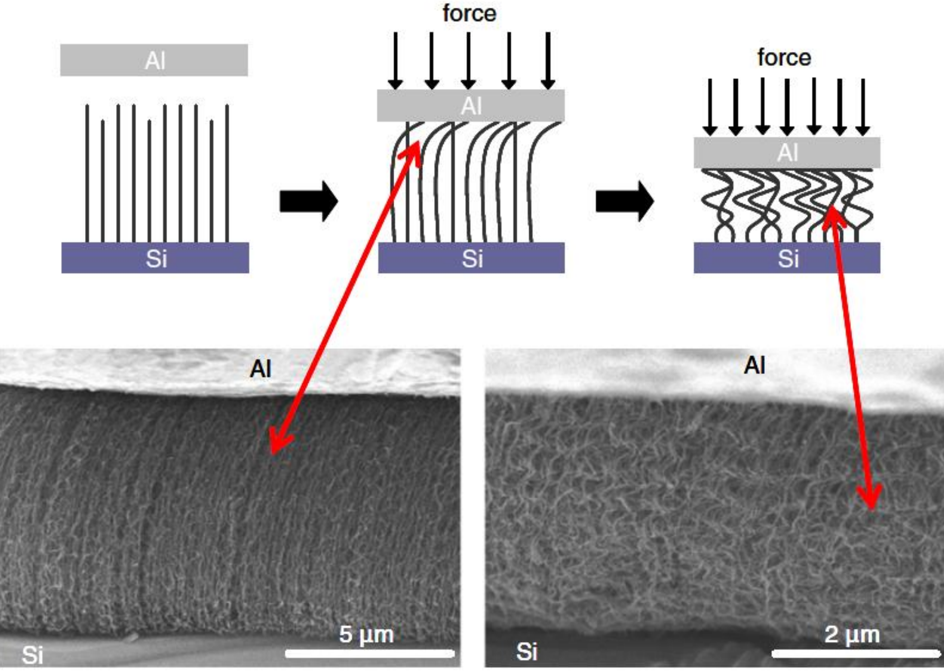

Figure 2.6: SEM images illustrating the bending of CNT tips to form cylinder-plane contacts with opposing surfaces [44].

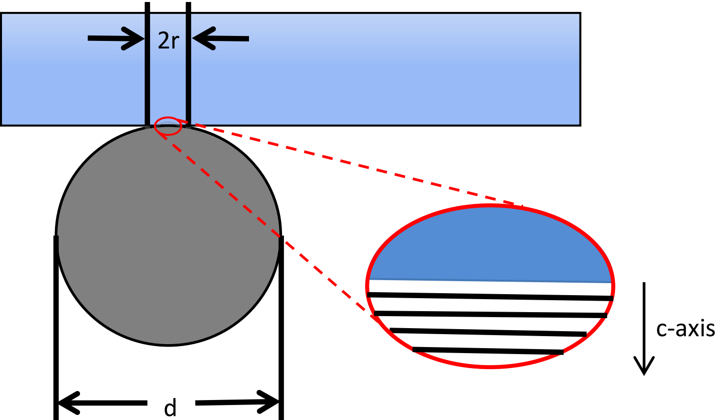

Figure 2.7: Cylinder-plane contact formed between a CNT tip and opposing substrate. Over the contact area the graphitic planes of the CNT sidewall are oriented parallel to the surface.

Considering van der Waals interactions, elastic contact, and the idealized cylinder-plane contact configuration of Figure 2.7, a CNT of diameter d will form a contact width, 2r, given by

$$2r = \left(\frac{16 f_{vdW} E_m d}{\pi}\right)^{1/2}, \tag{2.18}$$

where f_{vdW} is the net contact force per unit length due to vdW interactions and E_m is the effective modulus of elasticity [40, 84]. Multiwall CNTs typically have diameters between 5-50 nm, which using the parameters in reference [40] correspond to contact widths of ~0.75-2.5 nm respectively. Thermal transport within CNTs and at CNT contacts, even those with a metal, is dominated by phonons [20, 40]. The mean free path of phonons in crystalline solids is typically on the order of several hundred nanometers, although it can be as short as 4 nm [85] in defective muti-wall CNTs and in excess of 1 μm for both crystalline Si [86] and well graphitized CNTs [22]. Accordingly, the Knudsen number (Equation 2.17) for CNT contacts is typically ~1 or greater, confirming that ballistic effects significantly influence thermal transport and must be considered. The expression for the ballistic resistance given in Equation 2.16 is appropriate for CNT contacts.

The expressions for the constriction-spreading resistance of CNT contacts differ from those given in Equations 2.12-2.14, due to the difference in the contact geometry. Expressions for the constriction-spreading resistance of a cylinder-plane contact have been developed by McGee et al. [87] and applied to nanotube/nanowire contacts in several studies [38, 44, 84]. As in the generic case of a circular contact an expression for the constriction-spreading resistance based on the flux tube geometry on either side of the interface are developed separately and then added to represent the effective constriction resistance of the junction. The constriction-spreading resistance from the cylinder to the contact width 2r is

$$R_{c-s,cyl} = \frac{2r}{\pi k_{cyl}} \ln\left(\frac{2d}{r}\right) - \frac{r}{k_{cyl}}. \tag{2.19}$$

Defined in similar fashion, the constriction-spreading resistance for the substrate side of the interface is given by

$$R_{c-s,sub} = \frac{2r}{\pi k_{sub}} \ln\left(\frac{d}{\pi r}\right). \tag{2.20}$$

Cola et al. calculated the constriction and ballistic resistances for CNTs in contact with a variety of metals using the thermal properties of graphite and found that the ballistic resistance, ~10^{-3} mm^2-K/W, was typically two orders of magnitude larger than the constriction resistance, ~10^{-5} mm^2-K/W [44]. As was the case for theories describing transport at plane interfaces the assumption of perfect bonding generally causes the models describing transport at CNT contacts to under predict of the actual resistance. Estimates of the contact resistance of individual CNTs interacting with surfaces through vdW interactions from experiments and simulations are generally an order of magnitude larger, on the order of 0.02 mm^2-K/W [20, 41].

2.3.2 Contact Mechanics and Thermal Transport at the Scale of CNT Forests

Extending the analysis at individual CNT contacts to a CNT forest requires solving the contact mechanics problem to determine the contact area. The sheer number of CNTs in a forest and the inherent variability in their arrangement makes the extension of atomistic scale models, such as molecular dynamics [41] or atomistic greens function [88], of individual CNT segments to entire CNT forests computationally intractable. Micro-scale models using techniques such as coarse-graining have had some success capturing the microstructure dependent mechanical and thermal behavior of CNT forests and sheets (bucky papers), however simulations are typically restricted to around 100 CNTs five micrometers or less in length [89, 90]. Here, a semi-empirical model developed by Cola et al. is reviewed [44]. The model uses wool fiber compression theory, load-displacement data from real CNT forests, and classical contact mechanics to predict the contact area at the CNT tip interface.

In the 1940s van Wyk derived a theoretical model to describe the compressive behavior of entangled wool fibers for the textile industry [91]. Using fiber bending mechanics, a statistical description of the orientation of individual fibers, and inter-fiber mechanical interactions van Wyk was able to theoretically capture the experimentally observed compressive behavior of

wool fiber masses. Specifically, van Wyk was able to describe the inverse proportionality between the volume of a fiber mass and the cube root of the pressure applied to the mass using simple parameters like the volume fraction of the fibers in the uncompressed mass. A half-century later Cola et al. [44] noticed that CNT forests exhibited similar $V \alpha P^{-1/3}$ compressive behavior and adapted an extension of van Wyks model [92] to describe the compressive behavior of CNT forests. In the model the height, or thickness t, of the CNT forest is related to the applied compressive pressure by the expression

$$t = t' + (t_0 - t') \cdot \left(\frac{P_f}{\sigma_R} + 1\right)^{-\frac{1}{3}}, \tag{2.21}$$

where t' is the incompressible thickness, t_0 is the thickness under no compressive load, P_f is a contact area corrected pressure, and σ_R is a parameter describing the forests resistance to compression. P_f is expressed in terms of CNT forests characteristics through the expression

$$P_f = \frac{P}{\left(\Phi \frac{2r}{d}\right)}, \tag{2.22}$$

where P is the compressive pressure applied to the forest, Φ is the volume fraction of CNTs in the forest, r is the contact half-width (Figure 2.7) formed by a CNT of average diameter d in the forest. The CNT forests resistance to compression is given by

$$\sigma_R = c_1 \cdot E_b \cdot \Phi^3, \tag{2.23}$$

where c_1 is a fitting parameter to account for variations in CNT characteristics and E_b is the average bending modulus of a CNT in the forest. Cola et al. validated the model by successfully fitting it to multiple sets of published CNT forest load-displacement data, and noting that fit values for t_0 closely matched the height of uncompressed CNT forests as measured by SEM.

To determine the contact area at the CNT free tip interface the pressure-thickness relation of Equation 2.21 is used to derive an analytical expression for the bulk compressive modulus of a CNT forest. Specifically, the thermodynamic definition of bulk compressive modulus is used

$$B = -t(dP/dt). \tag{2.24}$$

Finally, this bulk compressive modulus is used as an input in classical contact theory [12, 14] to predict the contact at the CNT forest tip interface using the relation

$$\frac{A_{CNT\ tips}}{A_{total}} = \frac{2P}{B}. \tag{2.25}$$

The contact area is related to the thermal resistance by the expression

$$(R_{OS\text{-}CNT}/R_{CNT\ tip}) = (A_{CNT\ tips}/A_{total}), \tag{2.26}$$

where the subscript OS-CNT is used to denote the effective thermal resistance between the CNT forest and an opposing substrate. Experimental results or thermal models like those reviewed in section 2.2.2 or elsewhere for individual CNT contacts can be used for $R_{CNT\ tip}$ in Equation 2.26 to calculate the thermal resistance of the entire CNT free tip interface.

CHAPTER 3

EXPERIMENTAL METHODS

This chapter describes the methods by which CNT forest TIMs were fabricated and characterized in this research. Specifically, it describes the CNT forest synthesis procedure and the thermal characterization methods; photoacoustic, and time-domain thermoreflectance. The processes developed for mitigating the contact resistance at the CNT forest tip interface are discussed in their respective chapters.

3.1 Carbon Nanotube Forest Synthesis

For the majority of experiments nominally vertically aligned forests of CNTs were grown on 1x1 cm^2 single-crystal Si substrates. Ti, Al, Fe films in thicknesses of 30, 10, 3 nm were consecutively evaporated onto the Si as support and catalyst layers for CNT growth. CNT forests were grown using a low pressure chemical vapor deposition (LPCVD) process at 850 °C and 10 mbar in an *Aixtron Black Magic*© reactor (maintained by the Georgia Tech Institute for Electronics and Nanotechnology) with acetylene (C_2H_2) as the carbon source gas. The growth time was varied from 30 s to 15 min to grow forests of multiwall CNTs ranging from 5 to 150 μm in height with an average CNT diameter of 8 nm and an average of 7 walls. To minimize variability in the CNT growth the Si substrates were sequentially rinsed in acetone, methanol, and isopropyl alcohol before the catalyst deposition and a 5 min O_2 plasma clean recipe was executed prior to each growth. A representative scanning electron microscope (SEM) image of a CNT forest and a transmission electron microscope (TEM) image of an individual CNT, are shown in Figure 3.1. Raman spectroscopy was used to interrogate the chemical structure and "quality" of the CNTs. Figure 3.2 shows the Raman spectra for a CNT forest with the characteristic D (disordered/defective carbon), ~1350 cm^{-1}, and G (graphitic carbon) , ~1590 cm^{-1}, band peaks [93]. An intensity ratio I_G/I_D of ~1.1 was typical.

For the majority of applications it is not feasible to synthesize CNT forests directly on the surfaces of components comprising the interface. Therefore, CNT forests were also grown on both sides of 10 µm thick Al foil (*Alfa Aesar 41798*) to create a thermal interposer, similar to that

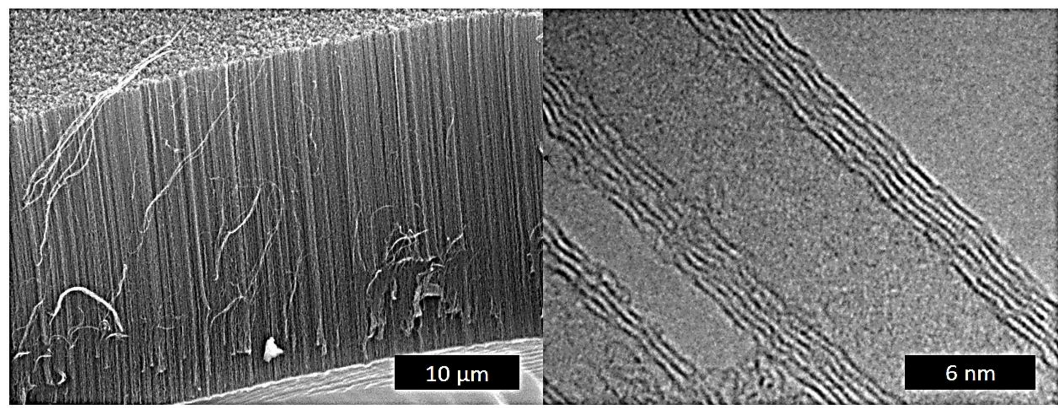

Figure 3.1: SEM image of a CNT forest (left) and TEM image of an individual CNT (right), characteristic of those used in this research.

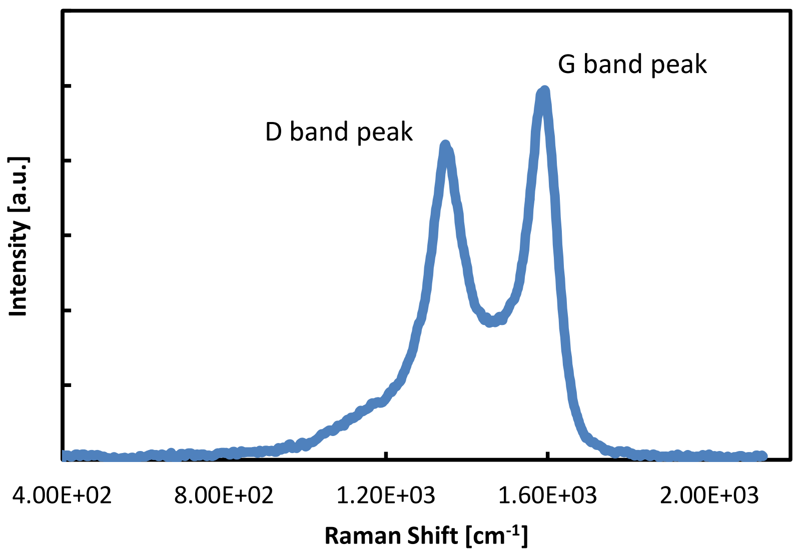

Figure 3.2: Raman spectra of a CNT forest, representative of those used in this research, with the with characteristic G and D band peaks used to infer CNT quality.

shown in Figure 3.3, for demonstrations of how the methods developed in this research might be implemented in industry. An identical growth process was employed except that 100 nm of Ni

was added to the bottom of the catalyst stack as a diffusion barrier and the temperature of the growth stage was lowered to 750 °C (a pyrometer measured the actual sample temperature to be approximately 630 °C, which is less than the melting temperature of Al).

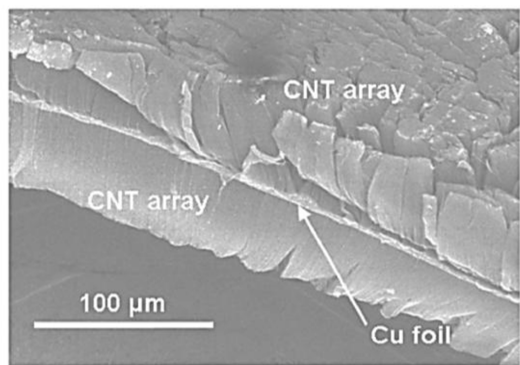

Figure 3.3: CNT Forest grown on both sides of a metal foil to create a thermal interposer [94].

3.2 Thermal Metrology

The efficacy of the methods developed in this research for mitigating the contact resistance in CNT forest TIMs are evaluated by experimental measurement of thermal resistance. Two steady periodic photothermal techniques, photoacoustic and time-domain thermoreflectance are used. Both of these techniques use modulated lasers to induce steady periodic surface heating in CNT structures. The spatial dimension profiled by these structures can be approximated by the thermal penetration depth, t_p, is given by

$$t_p = (2\alpha/\omega)^{1/2}, \tag{3.1}$$

where α is the thermal diffusivity of the material being heated and ω is the angular frequency of heating, equal to the laser modulation frequency [95]. The techniques used in this research use vastly different heating frequencies to profile the thermal resistance of CNT forest TIMs at different length scales.

3.2.1 Photoacoustic

Photoacoustic (PA) is a steady periodic technique photothermal technique for measuring the thermal properties of thin films, interfaces, and buried layers [11, 96, 97]. In PA a continuous wave laser (1100 nm wavelength) is square-wave modulated using an acousto-optic modulator before irradiating the sample of interest. The laser energy is absorbed in the sample and conducted as heat both downward into the sample, as well as upward into a sealed transparent gas filled chamber. The periodic nature of the heating causes periodic pressure fluctuations in the gas that are detected using a microphone embedded in the chamber wall. Lock-in amplification is used to extract the phase and amplitude of the microphone response at the modulation frequency and constitutes the measurement signal. A schematic of a PA experimental setup is shown in Figure 3.4.

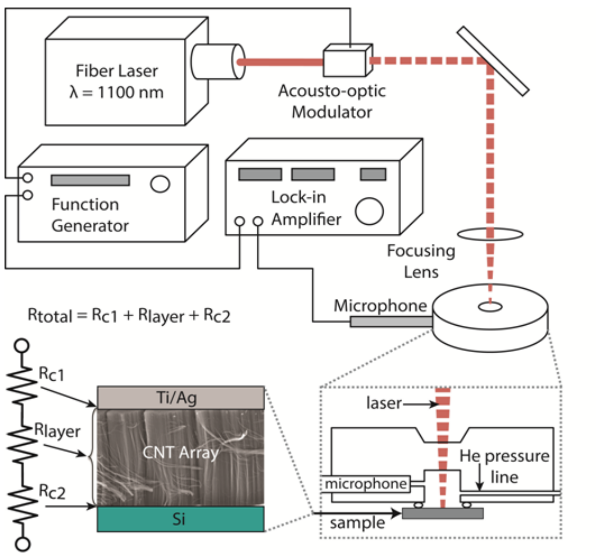

Figure 3.4: Schematic of the PA system used to measure the total resistance of CNT forest TIMs.

In a PA measurement the microphone response to a range of modulation frequencies, typically tens to several thousand Hz, is used to thermally profile the sample. By varying the modulation frequency, i.e. the frequency of heating, the thermal penetration depth (Equation 3.1)

is altered. In the PA experiments conducted for this research a frequency range of 300-4000 Hz was used to effectively profile entire CNT forest TIMs and their contact interfaces. The phase shift vs. frequency data is used in a theoretical model describing one-dimensional heat transfer through the sample layer(s) and the thermodynamics in the gas chamber, to extract unknown thermal properties [96]. Depending on the sample configuration and knowledge of the sample properties, the measurement can be used to extract thickness, thermal diffusivity, and thermal conductivity of the sample layer(s), in addition to thermal contact resistances between layers.

To evaluate the CNT TIMs developed in this research the free-tips of CNT forests on their Si growth substrates were contacted, or bonded, to a metal foil to simulate an interface, illustrated in Figure 3.4. The metal foil, typically 25 μm thick silver (*Alfa Aesar 11498*), is chosen as the top substrate because of its high thermal conductivity. As such, it has minimal thermal resistance and thereby maximizes the measurement sensitivity to the CNT underlayer. Uncertainty in the measurement primarily stems from uncertainty in the measured phase shift, typically ± 1 deg. or less. For vertical CNT TIMs uncertainties in thermal resistance values as low as 0.4 mm^2-K/W have been reported [11]. A feature of PA that can be useful for studying CNT TIMs is the ability to precisely control the pressure applied to the sample during the measurement. The measurement pressure, above the few kPa required to seal the chamber against the sample, is set via the base pressure of the He gas in the acoustic chamber. Pressures ranging from approximately 5-200 kPa are feasible.

The sample configuration used to characterize CNT forest TIMs with PA contains several unknown or difficult to determine parameters, including the thermal conductivity, heat capacity, and thickness of the CNT forest, in addition to the contact resistances of the Ti-Ag, Ag-CNT, and CNT-Si interfaces. The influence each of these parameters has on the PA signal is described by the sensitivity. In a PA experiment the sensitivity to a parameter, p, denoted as S_p, is given by

$$S_p = (\partial \varphi / \partial p) p, \tag{3.2}$$

where φ is the measured phase shift [97]. Figure 3.5 shows the sensitivity of the PA experiment to the aforementioned parameters for a 15 µm tall CNT forest with generic properties and Ag-CNT and CNT-Si interface resistances of 2 mm^2-K/W. As is shown in Figure 3.5, the PA signal depends on all of the parameters, with the exception of the CNT forest thermal diffusivity. For this reason all of these parameters were treated as unknowns during data fitting. Data fitting was conducted using a Levenberg-Marquardt non-linear least squares algorithm [98]. To ensure that the algorithm converged to a global minimum each fitting parameter was separately varied by 5, 20, 500, and 2,000% to create four additional sets of guess values. Since there were typically six fitting parameters in this research the data was usually fit using 24 additional sets of guess values. Due to the large number of fitting parameters, the specific sample structures, and the upper limit on heating frequencies (6-8 kHz) that can be tested with PA the confidence interval was too large to meaningfully resolve parameters on an individual basis. To illustrate this an experimental data set for a CNT forest is shown in Figure 3.6 with two theoretical fits. The two fits are indistinguishable and yield the same value for the total resistance; however, the component resistances for the two fits differ considerably. As a result, a unique solution could only be obtained for the total resistance of CNT forest TIMs with PA.

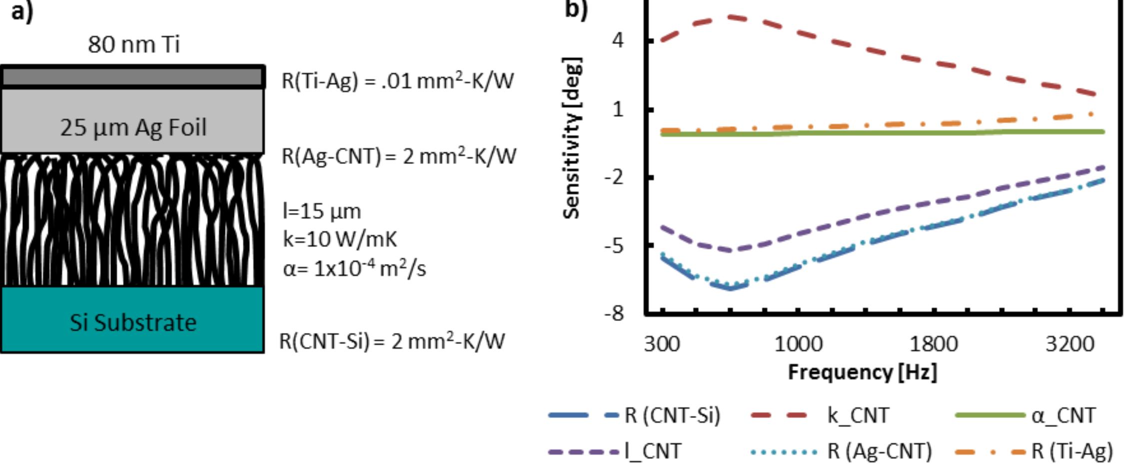

Figure 3.5: **(a)** CNT forest properties used to plot **(b)** the sensitivity of the PA measurement to unknown parameters.

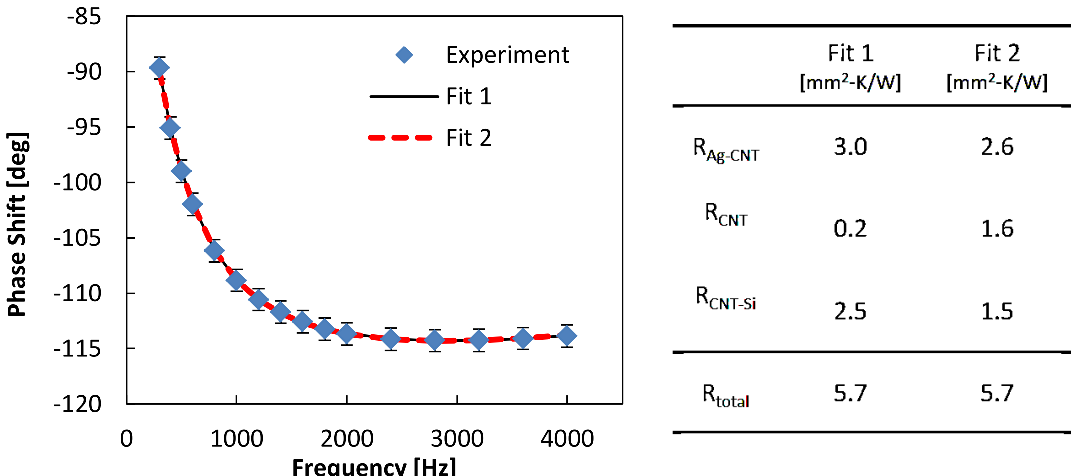

	Fit 1 [mm²-K/W]	Fit 2 [mm²-K/W]
$R_{Ag\text{-}CNT}$	3.0	2.6
R_{CNT}	0.2	1.6
$R_{CNT\text{-}Si}$	2.5	1.5
R_{total}	5.7	5.7

Figure 3.6: Two theoretical fits to PA data collected on a 10 μm tall CNT forest in dry contact with Ag foil. The total resistance was identifiable with PA, however the component resistances were not.

3.2.2 Time-Domain Thermoreflectance

Time-Domain thermoreflectance (TDTR) is a steady periodic photothermal technique for measuring the thermal properties of bulk materials, thin-films, and interfaces. TDTR is a subset of a broader class of photothermal spectroscopies referred to as pump-probe thermoreflectance methods, which include nanosecond thermoreflectance [45] and frequency-domain thermoreflectance (FDTR) [99]. In all pump-probe thermoreflectance techniques two laser beams are required. The frequency modulated pump beam is irradiated onto a metal film, typically 100 nm in thickness, coated onto the sample surface to induce a heat flux. The probe beam incident at the same location on the sample measures indirectly the surface temperature change through changes in the reflectivity of the metal film. Metal films with a high temperature coefficient of reflectivity at the wavelength of the probe beam (predominantly Al at 800 nm) are used to maximize measurement signal [100].

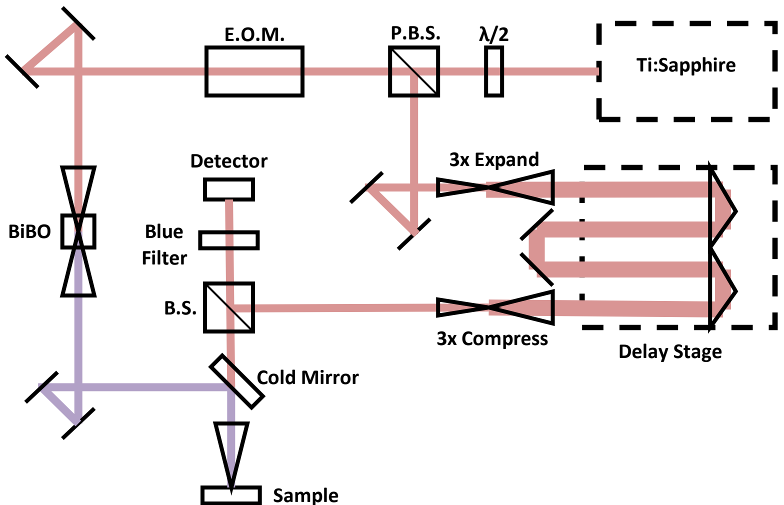

Figure 3.7: Schematic of the two-color TDTR system used in the NEST lab to characterize CNT forest TIMs.

A schematic of a TDTR system in the NEST lab at Georgia Tech is displayed in Figure 3.7. In TDTR a Ti-sapphire ultrafast laser oscillator that emits 800 nm wavelength light pulses ~100 fs in duration at a frequency of 80 MHz is used. The emission from the oscillator is split using a polarizing beam-splitter to form the pump and probe beams. The pump beam is frequency modulated using an electro-optic modulator at a frequency that is an order of magnitude or two lower than the frequency of the oscillator to facilitate lock-in detection of the probe response. The modulated pump beam is then frequency doubled to 400 nm using a BiBO crystal. This enables the pump and probe beams to be configured co-linearly as they approach the sample, but separable through the use of spectral filters. The path length traversed by the probe beam is adjusted using a linear stage to control its arrival at the sample surface relative to the pump beam. The reflected probe beam is captured with a photodetector and lock-in amplification is used to extract the component at the modulation frequency of the pump beam. By measuring the changes in the reflected probe energy at time delays from zero to several nanoseconds the transient temperature response of the sample surface is recorded. The reflectance data, typically the ratio of the in-phase and out-of-phase components, is used in a theoretical heat transfer model [101-103]

to extract unknown parameters by fitting the model to the data. In general TDTR can be used to measure in-plane and cross-plane thermal conductivity, heat capacity, and contact resistance. Owing to the high modulation and pulse frequencies used in TDTR experiments the spatial-temporal scales profiled (Equation 3.1) are typically on the scale of picoseconds and nanometers, and are favorable for interrogating thermal transport at interfaces. In particular, TDTR is well-suited to characterize the interface between the metal transducer layer and the sample [69, 79, 104, 105]. Uncertainties in the thermal resistance of the transducer-sample interface on the order of $\pm$ 0.1 mm^2-K/W have been reported [79] for these configurations.

Nanosecond thermoreflectance and FDTR have been previously used to study the thermal properties of CNT forests [45, 46, 106]. In these experiments the metal transducer film was deposited directly onto the free tips of the CNT forest, resulting in a conformal coating across the entire surface of the CNT forest. To study the processes developed in this research it is essential that CNT forests contact the free surface of a pre-existing transducer to accurately capture the mechanics and CNT tip morphology of bonded or pressed contacts. In 2008 Schmidt et al. adapted the TDTR technique for measuring the thermal conductivity of liquids [103]. In the experiment, illustrated in Figure 3.8 a small amount of liquid is pressed between two glass microscope slides, one of which has the Al transducer film deposited on the inner surface. The pump and probe beams pass through the transparent glass slide and are incident on the transducer film. Heat generated in the transducer is conducted both into the sample layer and back into the glass cover slide. As such the measurement becomes sensitive to not only the thermal properties of the sample layer, but also those of the glass slide. Schmidt modified the original TDTR theory to account for the bidirectional flow of heat and validated its use by measuring the thermal conductivity of several liquids. Here, the bidirectional heat flow model is used to characterize CNT forests bonded to Al transducer films deposited on glass microscope slides [107]. Specifically, it is used to measure the interface resistance between the CNT forest tips and the Al transducer to assess the efficacy of the processes developed in this research. To control the

pressure applied to the CNT forest-Al transducer interface a compact linear-compression cell with a load capacity of 445 N was constructed and is illustrated schematically in Figure 3.9.

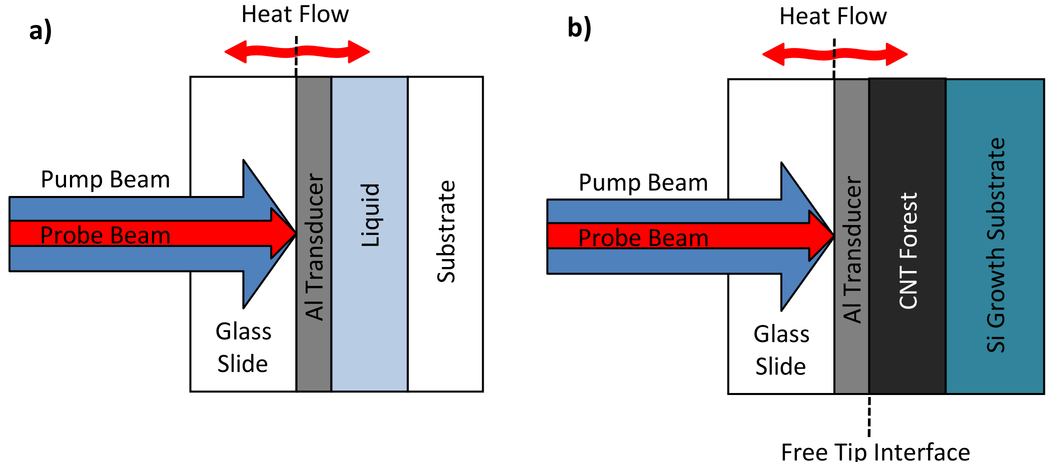

Figure 3.8: TDTR sample configuration with a transparent top substrate and bi-directional heat flow **a)** originally used to measure the thermal conductivity of liquids, **b)** adapted in this research to characterize bonded/pressed CNT forest contacts.

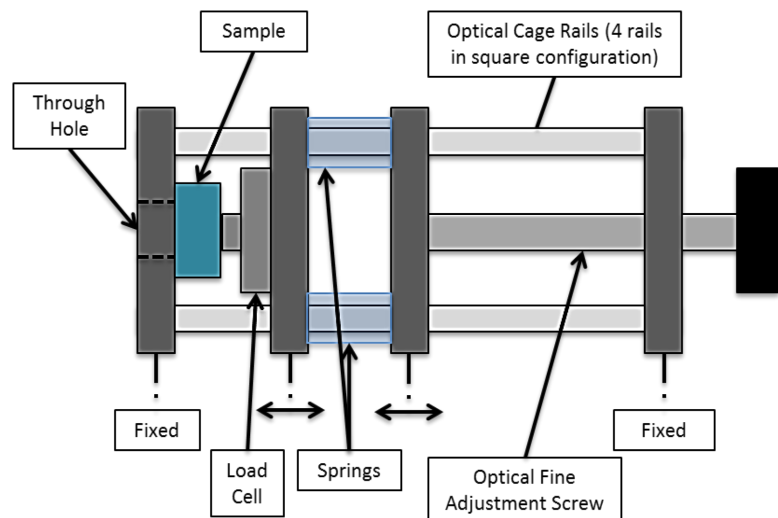

Figure 3.9: Side-view schematic of the linear-compression cell used to apply pressure to CNT forest contacts during TDTR measurements.

In TDTR a number of system parameters can be tuned to influence the measurement. Most notably, the pump-beam modulation frequency can be adjusted to alter the thermal penetration depth, Equation 3.1. The measurement signal in TDTR experiments is typically on the order of microvolts, and can be challenging to isolate from background noise. A resonant filter is often used to increase the signal to noise ratio. Based on commonly available inductor sizes for constructing the resonant filter, modulation frequencies of 9.8, 6.3, 3.6, and 1.2 MHz are feasible. The TDTR system in the NEST lab has been verified at each of these frequencies using known materials. In this research, multiple modulation frequencies are often utilized to facilitate identification of multiple unknown parameters. For example, the measurement signal at 1.2 MHz might be more sensitive to unknown parameter “A” and much less sensitive to parameter “B”, but at a modulation frequency of 6.3 MHz more sensitive to parameter B than A. By performing TDTR at both of 1.2 and 6.3 MHz the ability to separately resolve both parameters A and B is improved [108, 109]. Factors that can also influence a TDTR measurement are the pump and probe beam diameters and powers. These parameters generally impact the magnitude of the measurement signal, the steady state temperature rise, and radial transport [102, 110]. In this research the pump-beam diameter was set to 70 μm and the probe beam diameter to 28 μm. A pump beam power of 20-30 mW and a probe beam power of ~5 mW were used to minimize the steady state temperature rise in the sample, while maintaining a sufficient signal/noise ratio. Radial transport is not expected to play a significant role under these conditions and given the highly anisotropic nature of CNT forests. Nonetheless, it is accounted for in the theory used to model the data [103].

CHAPTER 4

ENHANCING CONTACT AREA: LIQUID SOFTENING

4.1 Introduction

A strikingly simple and straight-forward approach for improving contact to CNT forests is developed. The approach involves wetting the CNT forest with a liquid, pressing it into contact with the surface, and then allowing it to dry under pressure. It was discovered through a control experiment for the research presented in Chapter 5. The approach has ramifications for not only CNT forest TIMs, but also gecko-mimetic CNT forest adhesives where the contact area directly impacts the achievable adhesion.

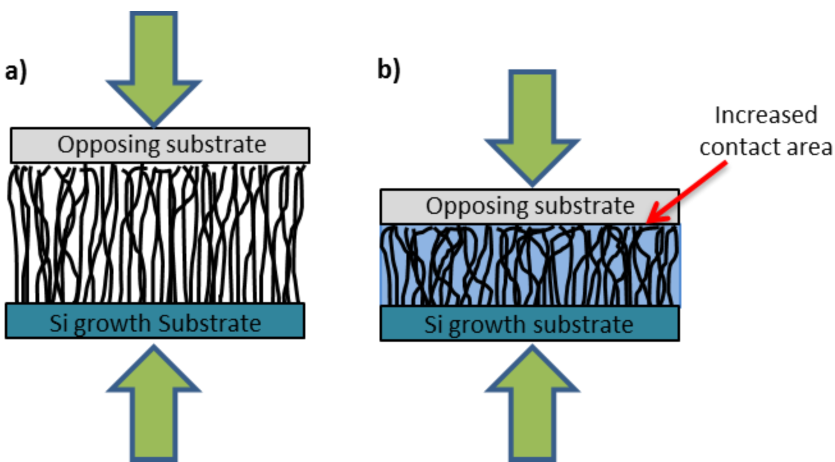

Figure 4.1: Illustration of inter-CNT vdW interactions being attenuated by liquid, decreasing the stiffness of the CNT forest, and increasing the contact area **(b)**, over the dry state **(a)**.

4.1.1 Hypothesis

There are two plausible mechanisms by which the infiltration, compression, and subsequent evaporation of liquid from CNT forests against a surface might increase the contact area. The first

is related to the attenuation of inter-CNT vdW interactions. It is well established that vdW interactions at CNT-CNT contacts contribute to the mechanical behavior of CNT forests [111-114]. Only recently has it been shown that by infiltrating the CNT forest with a liquid the vdW interactions within the forest can be diminished leading to a significant reduction in the mechanical stiffness [115-117]. Decreasing the mechanical stiffness of the forest enables it to deform more readily under a compressive load and may ultimately increase the contact area at the CNT tip and opposing surface interface [12, 44], as illustrated in Figure 4.1.

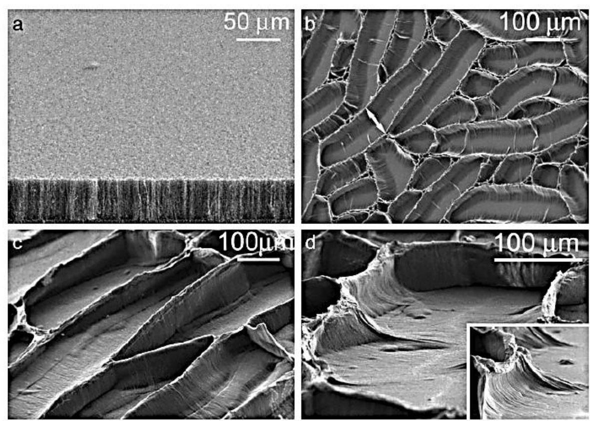

Figure 4.2: Capillary induced deformation of CNT forests into cellular structures [118].

The second potential mechanism is attributed to capillary forces that arise during the evaporation process. The capacity for capillary forces to deform CNT forests has been widely demonstrated and has even been tailored for densification and the formation of complex microstructures [118-121], an example is shown in Figure 4.2. It is conceivable that while liquid evaporates from a CNT forest capillary stresses pull near-surface CNT segments into contact with the surface and increase the contact area, illustrated in Figure 4.3. The capacity for both of these mechanisms to enhance contact between a CNT forest and a free surface is investigated.

4.2 Methods

The CNT forests used in this research were fabricated on 1 cm^2 Si tabs, as described in section 3.1. The growth time was tuned to produce CNT forests 5-10 μm (short) and 60 μm (tall) in height.

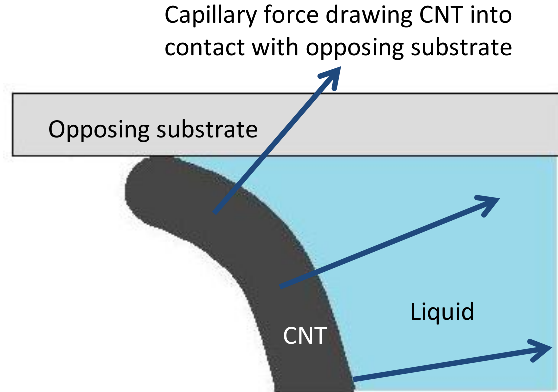

Figure 4.3: Illustration of capillary forces during evaporation of liquid from a CNT forest pulling a CNT tip into contact with the opposing substrate.

4.2.1 The Wet-Compress-Dry (WCD) Process

To understand the influence of liquid infiltration and drying on CNT tip contact two sample configurations were studied. For the first configuration the as-grown CNT forests were compressed against opposing substrates for subsequent thermal or mechanical characterization. In the second configuration, the as-grown CNT forests were wet with liquid from a pipette, compressed against the opposing substrate, and allowed to dry under pressure. The wetting, compressing, and drying procedure is illustrated in Figure 4.4. These sample configurations are referred to as dry, and wet-compressed-dried (WCD) hereafter.

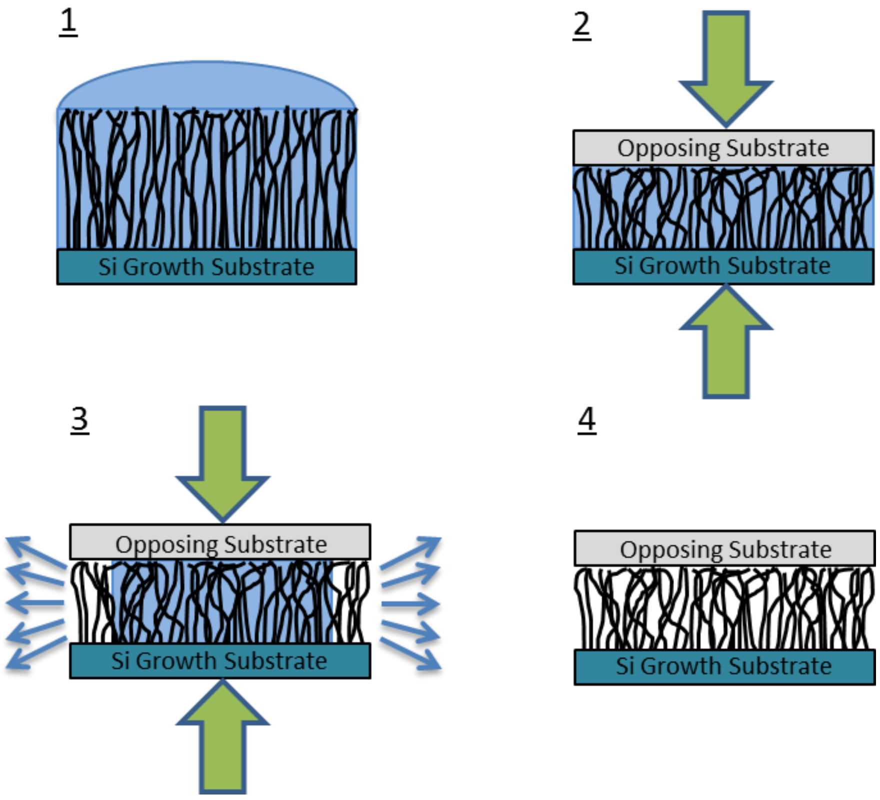

Figure 4.4: Illustration of the WCD process 1) CNT forest is wet with a liquid, 2) the wet CNT forest is compressed against the opposing substrate, 3) the liquid evaporates from the compressed CNT forest, and 4) the dry structure undergoes thermal or mechanical testing.

4.2.2 Photoacoustic

The photoacoustic method, implemented as described in section 3.2.1, was used to measure the total thermal resistance of dry and WCD CNT forests. The CNT forests were compressed against the opposing Ag substrates for at least five hours prior to execution of the experiment. This was done to ensure that the liquid fully evaporated from the WCD samples. The compressive load was provided by the helium gas in the acoustic chamber (Figure 3.4) and remained applied to the sample during the measurement. To understand any influence the compression pressure might have on the results PA experiments were conducted at pressures of 35, 70, 105, and 140 kPa. Additionally, PA experiments were conducted on CNT forests wet with liquid and allowed to dry before being placed in contact with the Ag foil. For this sample configuration only capillary forces can influence the contact area.

4.2.3 Shear Adhesion

The adhesion of dry and WCD CNT forests was assessed through a shear failure mode using a *Dage 4000* commercial die shear apparatus. For the shear tests the CNT forests were compressed against glass substrates. During the test the glass substrates were held fixed, while a lateral force was applied to the Si growth substrate to shear the CNT forest from the glass substrate. As in the PA experiments the CNT forests were compressed against the opposing glass substrates for at least five hours prior to execution of the experiment to ensure that the liquid fully evaporated from the WCD samples. For the adhesion measurement the compressive load was applied via weights placed upon the sample, and was removed after the five hour drying period. No compressive pressure was applied to the sample during shear tests. To understand any influence the compression pressure might have on the results die shear experiments were conducted at pressures of 0, 35, 70, 105, and 140 kPa.

4.2.4 Capillary Forces

The CNT forests used in thermal measurements were wet with either water or hexane with the intent to modulate the magnitude of the capillary forces present during the drying process. Water is a highly polar solvent with a dipole moment of ~1.85 D and a surface tension in air of ~72 mN/m. In contrast, hexane is a virtually non-polar solvent with a dipole moment of ~0 D and a surface tension in air of only ~18mN/m [122]. The contact angle of both water and hexane on CNT forests and on the Ag opposing substrates used in PA measurements were measured using a goniometer (*Rame-hart 250*). Water had an average contact angle of 90° on Ag (Figure 4.5(a)) and 115° on CNT forests, before slowly infiltrating the forest. Contact angle measurements were not feasible for hexane, as it wet nearly perfectly to both surfaces and evaporated rapidly. Since the component of the capillary force normal to a surface scales with the product of the surface tension and the sine of the contact angle (Figure 4.5(b)), the magnitude of the capillary forces are expected to be significantly stronger for water than hexane. WCD samples for shear adhesion tests were prepared exclusively with hexane.

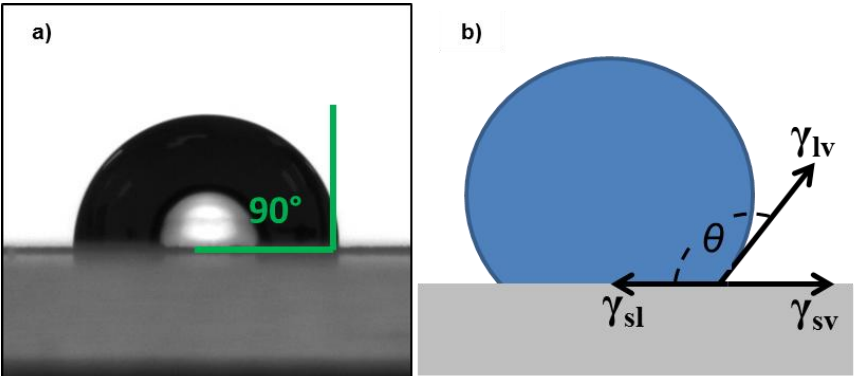

Figure 4.5: (a) Contact angle of 90° formed by water on Ag, and (b) illustration of surface forces acting on a droplet on a surface. The force normal to the surface is proportional to the liquid-vapor surface tension and the sine of the contact angle.

4.2.5 Coarse-Grain Mechanics Simulations

To further investigate the extent to which relaxing inter CNT vdW interactions within the forest improves tip contact a coarse-grain model of short CNT forests [89, 90] was employed by collaborators Mr. Sridhar Sadasivam and Professor Timothy S. Fisher at Purdue University. The model uses an energy minimization routine to predict the microstructure, and thereby the contact area, of CNT forests compressed against a flat smooth surface. The total energy of the system in the coarse-grain model is given by

$$U = U_{str} + U_{bnd} + U_{vdw} = \sum_{pairs} \frac{1}{2} k_r (r - r_0)^2 + \sum_{triples} \frac{1}{2} k_b (\theta - \theta_0)^2 + \sum_{pairs} LJ(r), \qquad (4.1)$$

where U_{str}, U_{bnd} *and* U_{vdw} denote the energies due to axial stretching, bending and vdW interaction among CNTs respectively. k_T, k_b can be related to the Young's modulus and bending stiffness of an individual CNT respectively [90]. In the present work, the Young's modulus of the mulit-wall CNT is assumed to be same as that of graphite and the bending stiffness is fitted to the experimentally measured Young's modulus from nanoindentation experiments. The strength of the Lennard-Jones potential is chosen to match the strength of vdW interaction in a fully atomistic model [90]. We perform coarse-grain simulations of a 5μm tall CNT array with nominal

vdW interaction (to simulate the compression of dry CNT arrays) and with artificially reduced vdW interactions (to simulate the compression of CNT arrays infiltrated with a liquid). All other simulation parameters are consistent in both simulations. The CNT array microstructures are obtained for a series of applied pressures and the microstructures are then analyzed to determine the CNT-substrate contact area.

4.3 Results

4.3.1 Photoacoustic Results

The average total thermal resistance of seven short (5-10 μm) dry CNT forests compressed under 140 kPa was measured to be 10 ± 2 mm^2-K/W. Three of those forests were subsequently wet with water, four with hexane, and compressed again under 140 kPa. The total thermal resistance for these short WCD samples was measured to be 2.5 ± 1.0 and 3.0 ± 1.0 mm^2-K/W for water and hexane respectively, Figure 4.6(a). As such, the WCD process enabled an approximately 70% reduction in the total resistance for both liquids. We attribute the entire reduction in thermal resistance to a change in contact area at the CNT tip interface, i.e. a reduction in $R_{Ag\text{-}CNT}$. It is unlikely that the total resistance is reduced from changes to $R_{CNT\text{-}Si}$ since the vast majority of CNTs are attached to Si substrate via the metal catalyst particles. Likewise, it is unlikely that the reduction in R_{total} stems from a reduction in R_{CNT} since the WCD process doesn't affect the CNT quality and since it is expected to be less than 3 mm^2-K/W for the short CNT forests used in this work [11, 123]. Similar reductions in total resistance were observed for WCD samples compressed with pressures as low as 35 kPa, shown in Figure 4.6(b). None of the short CNT forests tested exhibited noticeable adhesion to the Ag foil.

For many applications a TIM with a thickness, typically referred to as bond-line thickness (Figure 1.2), greater than 10 μm is necessary. Therefore, the thermal resistance of tall CNT forests, ~60 μm, was also measured and is shown in Figure 4.6(c). The total resistance of tall CNT forests was reduced from 32 ± 2 to 17 ± 1 and 54 ± 6 to 34 ± 2 mm^2-K/W by the WCD

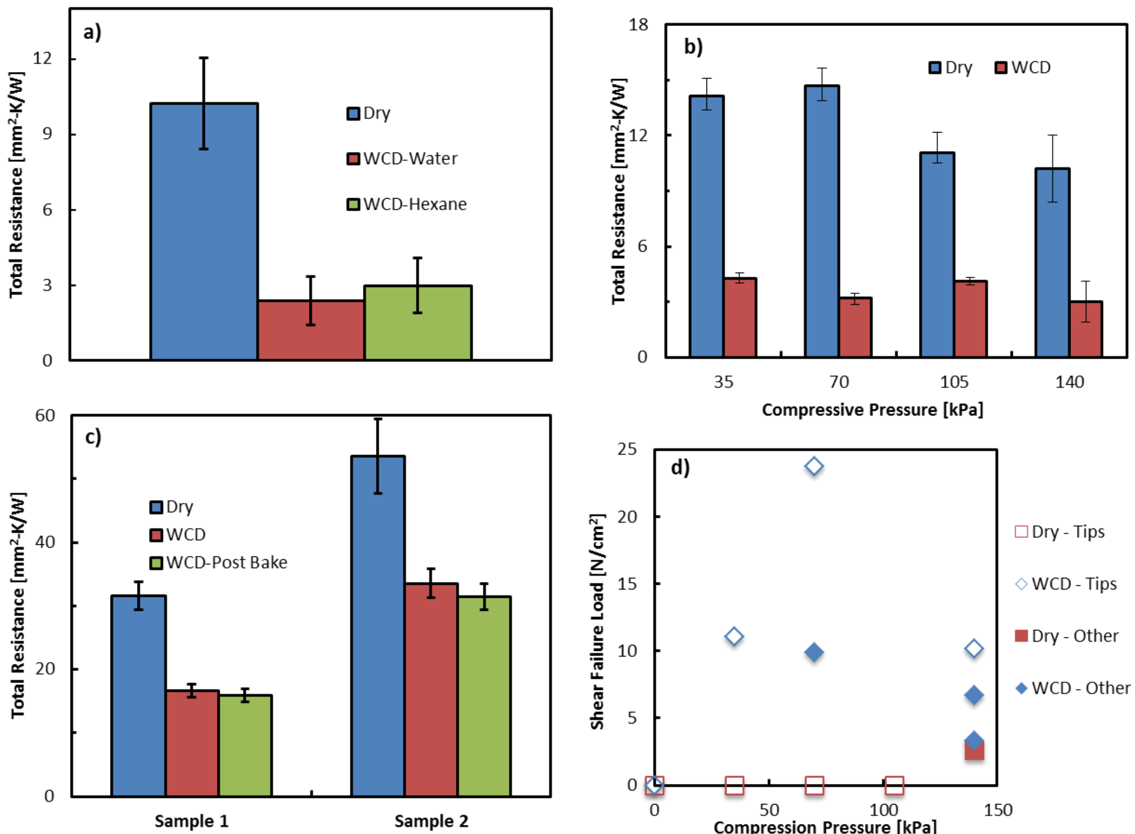

Figure 4.6: (a) Total thermal resistance of short CNT forests is reduced by ~70 after the WCD process with water or hexane, **(b)** the total thermal resistance of short CNT forests prepared under compressive pressures of 35, 70, 105, and 140 kPa are comparable after the WCD process, **(c)** the total thermal resistance of tall CNT forests was reduced by 30-40% from the WCD process and was unaffected by a thermal bake at 140 ˚C for two hours, and **(d)** shear adhesion of CNT forests to glass at unprecedentedly low pressures is enabled by the WCD process.

process. The percent reduction in total resistance for tall CNT forests, approximately 50% and 40%, is less than that of short CNT forests, ~70%, likely due to the decreased contribution of $R_{Ag\text{-}CNT}$ to R_{total}. Although, improving the number of CNTs in contact with the opposing surface could also increase the effective thermal conductivity of the forest [106]. After an initial PA measurement these tall CNT forests were baked at 140 °C in atmospheric for two hours with the intent of removing any residual adsorbed liquid from the interface. The total resistance remained unchanged after the bake, Figure 4.6(c), indicating that the total resistance is not reduced by a change in interface chemistry resulting from an adsorbed layer of liquid [124]. An additional tall

CNT forest was wet with hexane and allowed to dry while not in contact with the Ag foil. The thermal resistance before and after wetting was relatively unchanged, 39 ± 2 and 43 ± 3 mm^2-K/W respectively. The uncertainty in the reported thermal resistance measurements have contributions from data fitting, the resolution of the PA experiment, and for the short CNT forests compressed at 140 kPa variability across multiple samples. The uncertainty is taken as the square root of the sum of the contributions squared.

4.3.2 Shear Adhesion Results

The shear adhesion of dry and WCD CNT forests as a function of compressive pressure are displayed in Figure 4.6(d). Only short CNT forests (5-10 μm) were used in adhesion tests, much shorter than the 150 μm tall forests used in the landmark shear adhesion study [125]. Dry CNT forests generally exhibited no shear adhesion for compressive preloads from 35-140 kPa. This is not surprising since preloads in excess of 1 MPa are typically required to achieve adhesion with CNT forests [125, 126]. Nevertheless, WCD samples exhibited shear adhesion for all samples where a compressive preload was applied. The shear failure load for samples that failed at the CNT tip interface varied from roughly 10 to 24 N/cm^2, comparable to the best performing CNT forest adhesives [125, 127]. However, with no apparent dependence on the compressive pressure the WCD process enables excellent shear adhesion at preloads one to two orders of magnitude lower than previously required. For compressive preloads of 140 kPa samples of both types failed at the growth substrate interface, preventing measurement of the tip adhesion. The failure load for these samples was possibly reduced in-part by buckling-driven delamination of the growth substrate interface [128]. The uncertainty in the shear failure load is less than 2% and is dominated by the uncertainty in the sample area, 0.01 cm^2. Error bars are absent from Figure 4.6(d) for clarity.

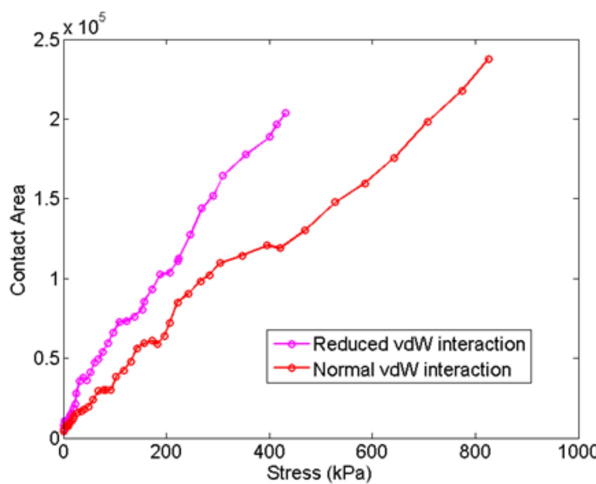

Figure 4.7: Coarse-grain mechanics simulations of CNT forests with reduced inter-CNT van der Waals interactions due to liquid infiltration exhibit enhanced contact area over dry forests.

4.3.3 Simulation Results

The coarse-grain mechanics simulations also revealed an increase in tip contact for CNT forests compressed in a wet state, i.e. CNT forests in which the inter-CNT vdW interactions were diminished, and are shown in Figure 4.7. As expected the contact area is identical for both dry and wet CNT forests under no applied load. As the compressive load increases the CNT tip contact area is observed to increase for both cases, more rapidly for the case with reduced vdW interactions. At compressive loads of 35, 70, 105, and 140 kPa the tip contact area increased by approximately 35, 60, 75, and 40% for wet CNT forests. In contrast with the experimental results, the simulated CNT forests exhibit pressure dependent tip contact. This inconsistency is possibly related to capillary induced effects associated with subsequent drying process, or to slight discrepancies between the stress-strain behavior of the actual and simulated CNT forests. Although the simulations do not perfectly replicate the experimental results, they support the notion that softening of CNT forests via liquid infiltration can lead to significant enhancements in tip contact.

4.4 Discussion

4.4.1 Attenuation of Inter-CNT van der Waals Interactions

The fact that water and hexane decreased the total resistance equally does not provide an indication as to whether or not the attenuation of vdW interactions in the wet state is responsible for increasing the contact area, or to what extent. Indentation tests on CNT forests, similar to the ones used in this study, wet with isopropanol, acetonitrile, or toluene revealed that the reduction in stiffness was not dependent on the dielectric characteristics of the liquid, indicating that all of the liquids tested relaxed the vdW interactions within the CNT forest to a similar extent [116].

To gain insight into the capacity for attenuated vdW interactions to reduce the thermal contact resistance a semi-empirical model developed by Cola et al. [44] for predicting contact area and thermal resistance of CNT interfaces is used. The model is reviewed in detail in 2.3.2. In the model the ratio of the actual contact area between the CNT tips and the opposing substrate to the total apparent area of the interface, $(A_{CNT\ tips}/A_{total})$ is given by Equation 2.25. Infiltration of CNT forests, similar to the ones used in this study, with toluene was found to reduce the stiffness by roughly 80% over the dry state [116]. Since stiffness is directly proportional to compressive modulus for these geometries the model predicts a 5-fold increase in $(A_{CNT\ tips}/A_{total})$ for WCD forests. $R_{Ag\text{-}CNT}$ is related to the contact area ratio by Equation 2.26, repeated here

$$(R_{Ag\text{-}CNT}/R_{CNT\ tip}) = (A_{CNT\ tips}/A_{total}), \quad (4.2)$$

where $R_{CNT\ tip}$ is the thermal resistance of an individual CNT contact [mm^2-K/W]. Assuming $R_{CNT\ tip}$ to remain constant throughout the soaking and drying process, the model predicts that diminishing the inter-CNT vdW forces will reduce $R_{Ag\text{-}CNT}$ by 80%. This is in agreement with the experimentally observed reduction, within the uncertainty, for short CNT forests where $R_{Ag\text{-}CNT}$ is the dominant component and suggests that the attenuation of vdW interactions could be responsible for the entire reduction in the thermal resistance. Likewise, the coarse-grain

mechanics simulations suggest that softening can significantly increase the contact area, 75% at 105 kPa.

4.4.2 Capillary Forces

The difference in the thermal resistance of WCD samples that were wet with water and hexane is within the uncertainty, suggesting that the tip contact area does not depend on the magnitude of the capillary forces. This notion is consistent with the recent findings of Tawfick et al. [129] where it was observed that liquids of differing surface tensions and contact angles, like the water and hexane used in this research, did not affect the extent of capillary driven CNT pillar densification. It was concluded that, regardless of the fluid used, the capillary stress exceeded the stress required to laterally compress CNT forests until extreme strains, ~0.8, approaching the compressible limit of the forest. These observations indicate that the wetting characteristics of the liquid cannot be used as a mechanism for tuning the contact area. They do not preclude, however, significant capillary induced increases in contact area.

WCD samples prepared under no compressive load represent the limiting case where contact enhancement due to the attenuation of van der Waals interactions is minimized. Thermal characterization of CNT forests under no applied pressure is not feasible with the PA method since light pressure is required to seal the sample surface against the acoustic chamber. However, WCD samples for die shear can be readily prepared under the weight of the sample alone. Both dry and WCD samples prepared under this condition demonstrated no adhesion, suggesting that capillary stresses alone do not produce an appreciable increase in contact area. However, it is possible that the effect of capillary forces only comes into play when sufficient contact has already been established in the interfaces, but this could not be tested.

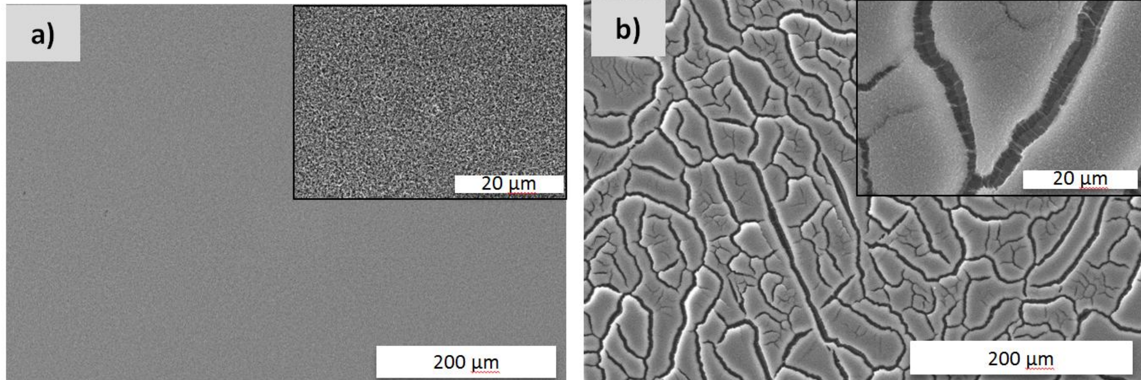

Figure 4.8: Top view SEM images of **(a)** short CNT forests, and **(b)** tall CNT forests, before and after the WCD process. The morphology of the short CNT forests remains unchanged, while the tall CNT forest exhibits lateral clumping due to capillary forces during drying. Insets display higher magnification images.

SEM images of short and tall CNT forests that underwent the WCD process in contact with the Ag foil for PA measurements are shown in Figure 4.8. For the short CNT forests the WCD process had no noticeable effect on the forest morphology. Conversely, tall CNT forests that underwent the WCD process exhibited lateral clumping, similar to that observed in previous studies [118]. When compressed between the growth and opposing substrates the liquid evaporates from the CNT forest along its periphery, as depicted in Figure 4.4 step 3. In this configuration capillary stress at the liquid-vapor-CNT boundary competes with the stiffness of the CNT forest to deform it in synchronization with the receding liquid volume. Since the liquid-vapor interface rests overwhelmingly between adjacent vertical CNTs in this configuration, the capillary stress acts predominantly in the lateral, in-plane direction, as shown in Figure 4.9, and likely overrides any contact enhancements due to stresses normal to the contact plane, as shown in Figure 4.3. In the case of the short CNT forests the pinning of individual CNTs to the growth substrate, CNT tip-opposing substrate contacts, and the increased effect of entanglement of the crust layer, which comprises a large portion of the short forest height, provide sufficient stiffness to prevent noticeable capillary induced deformations [120, 129]. For the tall CNT forests, the entangled crust layer accounts for only the top most fraction of the forest and the net capillary

force is increased proportionally to the increase in forest height, i.e. the length of the liquid-vapor-CNT boundary, leading to the formation of cellular structures [118, 130].

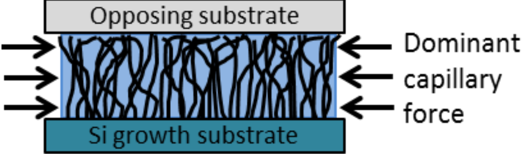

Figure 4.9: Capillary forces arising during evaporation act predominantly in the lateral direction.

Compressing the CNT forest in the wet state, where the stiffness is reduced, will undoubtedly increase the contact area at the CNT tip interface over the dry state, provided that the maximal contact area is not yet achieved. Contact saturation for dry CNT forests typically occurs at compressive pressures on the order of a MPa [44] an order of magnitude higher than those used in this work. Experimental measurement of the total thermal resistance of WCD CNT forests, the contact mechanics model of Cola et al., and coarse-grain simulations of CNT forests suggest that softening of the CNT forest in the wet state could increase the tip contact area between 75 and 80%. Moreover, the lack of dependence on compressive pressure for the WCD samples suggests that the contact area saturation may be achieved. Following compression in the wet state, the liquid evaporates from the CNT forest, during which time capillary stresses contend to deform the CNT forest. At this time there is no clear evidence that these capillary stresses act to further increase or decrease the contact area. In the case of short CNT forests, the stiffness of the forest prevents noticeable deformations altogether. For tall CNT forests the capillary forces are sufficient to laterally deform CNTs, however, it is not clear how or if these deformations affect the contact area at this time. Based on the geometry of the samples and the evaporation profile, the capillary forces will act predominantly in the lateral direction, which may not permit CNT deformation normal to the contact plane that would increase the contact area.

4.5 Summary

Infiltrating a CNT forest with a liquid prior to pressing it into contact with a surface has been demonstrated as a method for dramatically improving contact to the CNT tips. The method reduced the thermal resistance of CNT forests by as much as 80% over those compressed in a dry state. Likewise, the method enabled CNT forest shear adhesion to glass as high as 10-24 N/cm^2, with a compressive preload of only 35 kPa, one to two orders of magnitude lower than that required in previous studies utilizing dry CNT forests. The combination of experiments, coarse-grain mechanics simulations, and theory suggest that softening of the CNT forest in the wet state, due the attenuation of van der Waals interactions at inter-CNT contacts, can increase the contact area between 75 and 80%. No evidence was found to support the hypothesis that capillary induced deformations during drying will also increase contact. The approach can be implemented with any liquid, so long as it can infiltrate the CNT forest. High vapor pressure liquids can be used to reduce drying time. These findings have implications for a broad range of applications relying on contact to filamentary nanoscale materials.

CHAPTER 5

ENHANCING BOND STRENGTH: SURFACE MODIFIERS

5.1 Introduction

It is well established that weak interfacial bonding, like the vdW interactions at dry CNT contacts, significantly attenuates phonon transport at interfaces (reviewed in Chapter 2). Here it is shown that a simple organic surface modifier, a pyrenylpropyl phosphonic acid (PyprPA), can be synthesized and applied in a straightforward approach to improve bonding and consistently reduce the thermal resistance of mutli-wall CNT contacts by approximately 9-fold. The bifunctional interface modifier was designed such that it was terminated at one end with a pyrene moiety that is known to associate with CNT sidewalls through π-π stacking interactions [131, 132]. The opposite end of the molecule is terminated with a phosphonic acid functionality, which has been shown to form robust covalent bonds to native metal oxide surfaces [133-137] that are commonplace in electronic device architectures. This research was conducted in collaboration with Professor Seth R. Marder and Dr. O'Neil L. Smith of the Chemical and Biomolecular Engineering Department at Georgia Tech, who synthesized the PyprPA modifier and independently verified its attachment to both CNTs and metal oxides. The conclusion of the chapter highlights exploratory research examining alternative modifiers and attachment strategies.

5.2 Pyrenylpropyl Phosphonic Acid

The phosphonic acid was synthesized as illustrated in Figure 5.1 in two steps from 1-(3-iodopropyl)pyrene **1**, which was obtained using the method of Gastaldi and Stien [138]. Iodide 1 was then converted to phosphonate **2** and, with subsequent hydrolysis, to phosphonic acid **3**. The ability of the phosphonic acid to successfully modify both the CNTs and Cu oxide surfaces was verified independently using UV–visible (UV–vis) and X-ray photoelectron spectroscopy (XPS), respectively. CNTs were modified with the PyprPA using a protocol similar to that outlined by

Figure 5.1: Synthesis of pyrenylpropyl phosphonic acid. **1** iodide precursor, **2** phosphonate, and **3** phosphonic acid.

Simmons et al. [139]. The Cu surfaces were functionalized with the PyprPA using a protocol analogous to that reported elsewhere for the modification of indium tin oxide with phosphonic acids [137]. The complete synthetic and verification of modification details can be found in Appendix A. UV–vis spectra demonstrating the successful modification of CNTs are shown in Figure 5.2. Here the spectrum of the modified CNTs appears to be a superposition of the absorbance of the pristine phosphonic acid onto the CNT background. Calibration curves for both the pristine CNTs and the phosphonic acid were generated and used to estimate the amount of associated PyprPA per microgram of CNT (1.2×10^{-4} mol/µg; Figure A.2). In a similar manner, XPS was used to confirm the modification of the Cu oxide substrate with the phosphonic acid and evaluate the thickness of the overlayer. Specifically, the survey spectra (Figure 5.2(b)) show an increase in the C 1s signal upon modification of the Cu oxide film with the PyprPA and the high resolution P (2p) scan shown in the inset of Figure 5.2(b) confirms the presence of phosphorus on the surface. An approach previously discussed by Wallart [140], was used to assess the surface coverage of the modifier on the Cu oxide surface. Here the thickness of the PyprPA film was approximated to be 10.4 ± 0.3 Å which is less than the 13.6 Å calculated for a Hartree-Fock optimized geometry of a molecule that is oriented perpendicular to the surface (Figure A.5). This suggests that we did not form multilayers on the Cu oxide surface after sonication in a solution of ethanol:chloroform (1:1) for 5 min to remove excess PyprPA.

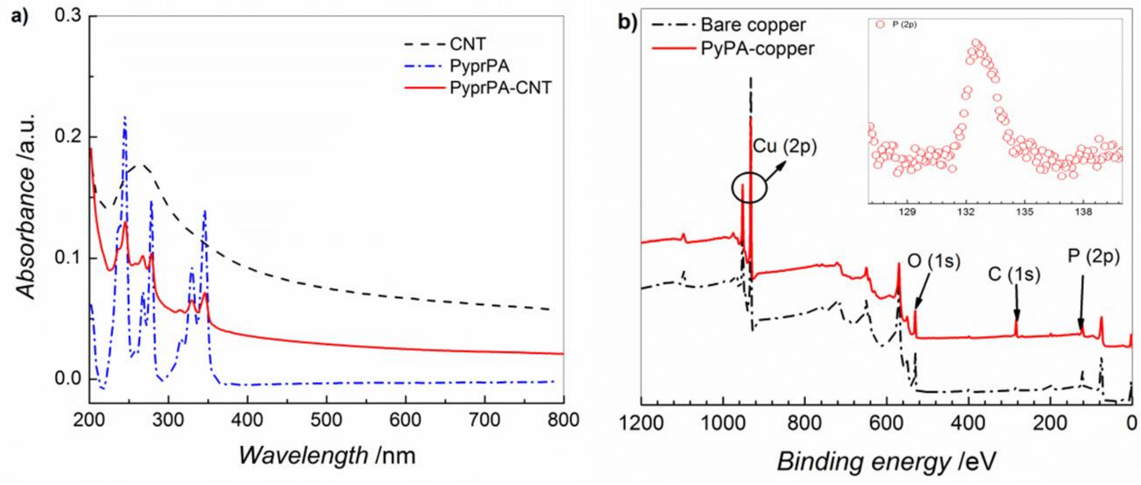

Figure 5.2: Modification of CNTs and copper oxide with phosphonic acid. a) Comparison of the UV-Vis spectra of the CNTs, phosphonic acid moiety, and the modified CNTs. b) XPS survey spectra of the modified and unmodified copper substrate.

5.3 Interface Modification and Coupling Procedure

Before modification took place the as-evaporated Cu films were exposed to an O_2 plasma at 200 mTorr pressure for 2 min to facilitate formation of a consistent surface oxide layer. Upon removal from the plasma chamber the Cu films were immediately placed in a 1.5 mM solution of the PyprPA modifier in ethanol:chloroform (1:1). The Cu films were soaked for at least 1 day, during which time the modification took place. The minimum soak time required to form a monolayer was not explored. For coupling the CNT forests, the PyprPA-modified Cu oxide film (PyprPA:CuO) was removed from the PyprPA solution and sonicated in a solution of ethanol:chloroform (1:1) for 5 min to remove excess PyprPA with the intent of leaving only a monolayer covalently bonded to the Cu oxide surface. The top of the CNT forest was then wet with a few droplets of ethanol:chloroform (1:1) to achieve maximum contact area (Chapter 4) and the PyprPA:CuO film was placed onto the wet forest. 300 kPa of pressure was applied to the still wet interface and it was allowed to dry for at least 5 hours at room temperature.

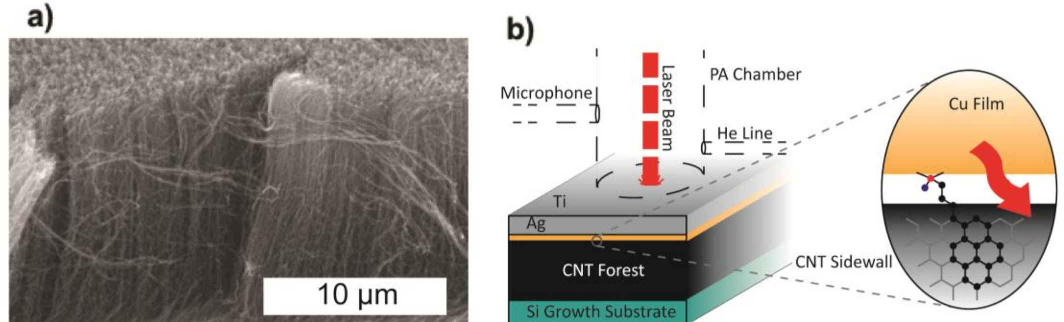

Figure 5.3: Sample and photoacoustic measurement configuration. **(a)** Representative SEM image of a CNT forest used for PyprPA interface coupling. **(b)** Photoacoustic measurement configuration (left) used to measure the thermal resistance of CNT forests coupled to oxidized Cu surfaces with the PyprPA modifier (right).

5.4 Total Thermal Resistance of PyprPA Coupled CNT Forests

For thermal characterization the PyprPA modifier was used to couple the free tips of vertical multi-wall CNT forests, roughly 15 µm in height, synthesized as described in section 3.1 and shown in Figure 5.3(a), to 300 nm thick Cu films evaporated on 25 µm Ag foil substrates. A surface oxide layer was established on the Cu films as described in the experimental section to facilitate experimental control, although the native oxide layer may be sufficient for the coupling process. The final sample configuration for thermal measurements can be seen in Figure 5.3(b). The thermal resistance of both CNT forests coupled with the PyprPA and those in dry contact with oxidized Cu films was measured using the PA technique, as described in section 3.2.1. PA tests were conducted at cell pressures of 7 kPa, a slight positive pressure to ensure that the chamber was filled with helium, and 140 kPa, to apply modest pressure to the interface. Five samples treated with the PyprPA modifier were prepared and PA tests were conducted at 3–4 different locations on each sample, providing 16 total measurements. Similarly, four dry contact samples were prepared and measurements were taken at 2–3 different locations on each sample, providing 11 total measurements. The beam diameter at the sample surface was approximately 1

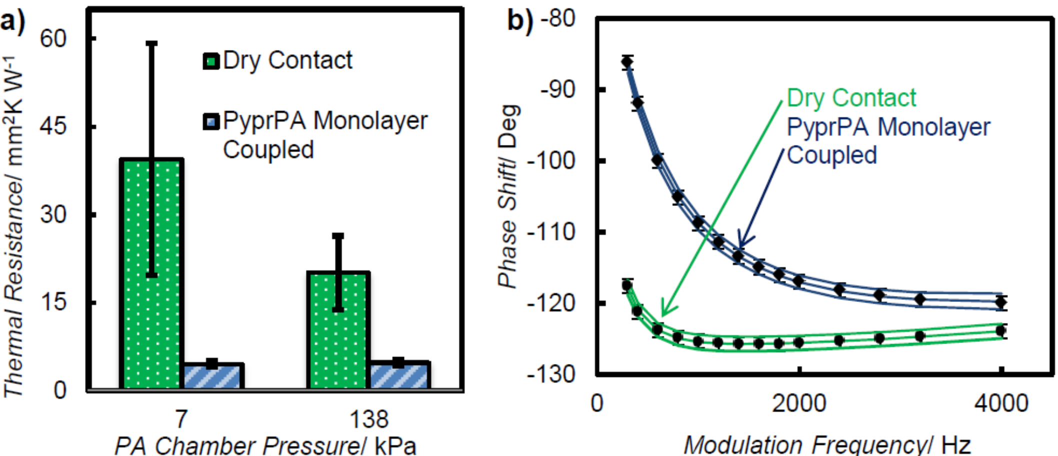

Figure 5.4: Photoacoustic characterization of CNT forests in dry contact and PyprPA coupled configurations. **(a)** Coupling the CNT tip interface with the PyprPA modifier reduces the thermal resistance of the interface material by 85–75% on average and alleviates the pressure dependence. Error bars include measurement uncertainty and variations in thermal resistance from multiple measured samples. **(b)** A representative photoacoustic measurement data set for a PyprPA coupled CNT forest, including theoretical curve fits to the data and to data sets shifted by the measurement uncertainty of ±1 degrees (solid lines).

mm and the surface area of each sample was 1 cm^2. By testing 2–4 different locations on the surface of each sample the efficacy of the coupling procedure over device-sized areas was examined. The total thermal resistance, comprised of the sum of the contact resistance at the CNT tip-Cu interface, the resistance of the CNT forest, and the contact resistance at the CNT-Si growth substrate interface, for both sample configurations and both PA chamber pressures is displayed in Figure 5.4(a). The error in the measurement has contributions from both the resolution of the experimental setup and variations in thermal resistance from sample to sample. The total thermal resistance of the dry contact samples was measured to be 40 ± 20 and 20 ± 6 mm^2-K/W at pressures of 7 and 140 kPa, respectively. Analogous trends have been observed in previous studies [11, 35] and were analyzed theoretically by Cola et al. [44]. In essence, increasing the pressure applied to the interface compresses the CNT forest and brings additional CNTs into contact with the Cu surface in addition to increasing the contact length of CNTs already in contact with the surface. The net effect is an increase in the contact area, or the area available for

heat conduction, resulting in a decrease in the thermal contact resistance. The total thermal resistance of the samples coupled with a monolayer of the PyprPA modifier using the procedure outlined above was measured to be 4.6 ± 0.5 and 4.9 ± 0.5 mm^2-K/W at pressures of 7 and 140 kPa respectively. The PyprPA modification and coupling procedure reduced the thermal resistance of the CNT forest by 88%-76% on average. The fact that the thermal resistance of the coupled samples did not exhibit a significant dependence on pressure, over the range considered, suggests that the contact area is constant and that the interface is well bonded. Moreover, the low thermal resistances achieved by coupling were consistent across the entire area of the sample (1 cm^2) demonstrating the strong uniform bonding over device-sized areas. Two additional PyprPA-coupled samples were fabricated in which the PyprPA:CuO was not sonicated prior to coupling this surface to the CNT forest. This was done to assess whether steps to attempt to create only a monolayer of PyprPA at the interface were required. The thermal resistance of the samples without sonication prior to CNT coupling were measured to be 9 ± 6 and 7 ± 3 mm^2-K/W at PA chamber pressures of 7 and 140 kPa respectively, which is an approximately 45% increase in the thermal resistance over CNT forests coupled to sonicated PyprPA:CuO substrates at 7 kPa. This increase in resistance can be attributed to the disorder and weak bonding associated with multiple layers of PyprPA not removed by the sonication step before coupling the surface to MWCNTs. For all of the aforementioned CNT-PyprPA:CuO samples the CNT forest was wet with a few drops of solvent (ethanol:chloroform (1:1)) and subsequently dried during the coupling process to maximize the contact area, as described in Chapter 4. To isolate the role of the PyprPA modifier two additional sample types were fabricated. For the first type (PyprPA-only) the sample was fabricated following the same PyprPA:CuO-sonication-CNT coupling procedure except no solvent was dripped onto the top of the CNT forest to wet the interface beforehand. For the second type (solvent-only) the CuO film was not modified with PyprPA prior to the coupling process. The thermal resistance of two PyprPA-only samples was measured to be 9 ± 4 and 8 ± 2

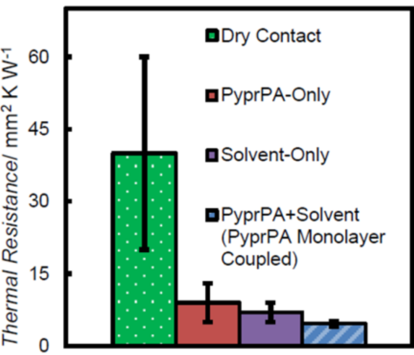

Figure 5.5: Effect of solvent on thermal resistance at 7 kPa. Coupling the interface with solvent and a monolayer of PyprPA increases the contact area and enables the formation of additional π-π bonds with the PyprPA:CuO. Results shown for the Solvent-Only configuration were collected before delamination occurred.

mm^2-K/W at 7 and 140 kPa, respectively (Figure 5.5). Likewise, two solvent-only samples were prepared and the thermal resistance was measured to be 7 ± 2 mm^2-K/W at 7 kPa and 7 ± 1 mm^2-K/W at 140 kPa the first time each sample was characterized using PA. However, the CNT-CuO interface was observed to be very weakly adhered. As such, when the solvent-only samples were removed and reinserted into the PA setup to measure the thermal resistance at a different location on the sample the CNT-CuO interface delaminated and the thermal resistance was measured to increase. After full delamination of the CNT-CuO interface the thermal resistance was measured to be approximately 19 ± 1 and 11 ± 1 mm^2-K/W at 7 and 140 kPa respectively. The exact contributions of the PypPA modifier and solvent cannot be resolved from these results; yet it is clear that both the solvent and PyprPA modifier play significant and different roles in decreasing the thermal resistance of the interface. For the PyprPA-only samples the thermal resistance was roughly ~75% reduced from the dry contact samples at 7 kPa. This demonstrates a significant benefit to having stronger covalent interactions between the phosphonic acid and the Cu oxide and π−π stacking interactions between the pyrenyl group and the CNT forest mediated by the PyprPA modifier, as compared to only having vdW interactions in the dry contact arrangement. The notion that interfacial heat transfer can be enhanced by improving the strength of bonding at the interface is well accepted [75, 78], although it has only recently been observed for surface

modifiers experimentally [79]. It should however be noted that without direct knowledge of the contact area at the interface it remains unclear if the reduction in thermal resistance of the PyprPA-only samples can be entirely attributed to enhanced bond strength as a result of the modifier. For the solvent-only interfaces the thermal resistance was ~80% less than dry contact samples at 7 kPa before delamination occurred. As was demonstrated in Chapter 4 compressing the CNT forest in the wet state, where inter-CNT vdW interactions are attenuated, increases the contact are at the CNT free tip interface. The fact that the reduction in total resistance was significantly less for solvent-only samples than it was for samples coupled with solvent and a monolayer of PyprPA, suggests that wetting the forest with solvent (the WCD process of Chapter 4) increases the contact area and enables additional π-π bonds to be formed between the PyprPA:CuO and CNTs, leading to a further reduction in thermal resistance. After routine handling the vdW bonded CNT-CuO interface of the solvent-only samples delaminated causing the thermal resistance of the samples to increase, whereas all samples coupled with the PyprPA remained adhered further demonstrating the benefit of the stronger covalent and π−π bonding present with the modifier.

5.5 Thermal Stability, Attachment Strength, and Electrical Characterization

To further assess the utility of the CNT-PyprPA:CuO system for thermal and electrical applications the thermal stability of the PyprPA molecule, and the attachment strength and current-voltage characteristics of CNT-PyprPA:CuO interfaces were examined. The thermal stability of the CNT-PyprPA:CuO interface was studied via thermogravimetric analysis (TGA) of PyprPA modified loose CNTs, shown in Figure 5.6(a). Approximately a 22 wt% loss that commenced at around 200 °C, well above the typical operating temperatures of electronic devices. The attachment strength of the PyprPA coupled samples used in PA tests (3 total) was measured through a tension failure mode, as shown in Figure 5.6(b), to be 340 ± 50 kPa, which is of similar order to the strength of Au-Au diffusion bonded CNT forest interfaces [34]. All samples failed at the PyprPA:CuO interface and no appreciable differences in attachment strength

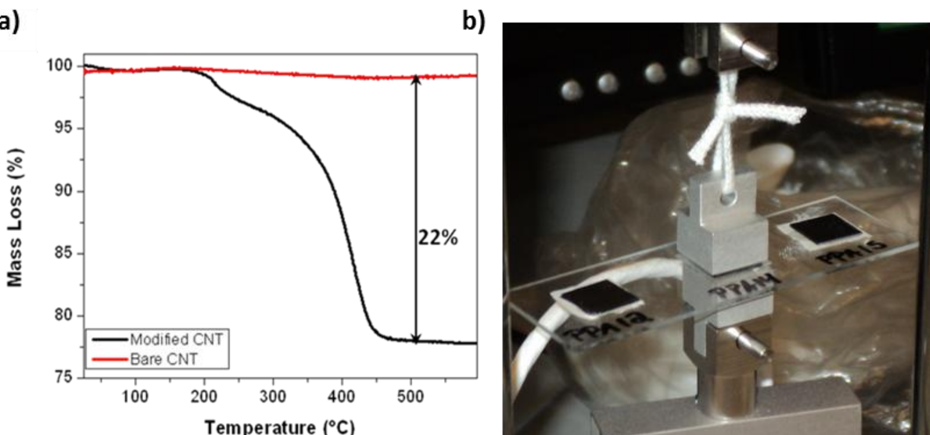

Figure 5.6: a) TGA of PyprPA modified and unmodified loose CNTs showing a 22% mass loss that commenced at 200 °C. **b)** Normal attachment strength of PyprPA coupled interfaces was measured through a tensile failure mode to be 340 ± 50 kPa.

were observed between all three PyprPA coupled interface configurations (i.e., solvent, with and without sonication, and dry coupled interfaces).

Samples for current-voltage scans were fabricated by growing CNTs on electrically conductive Cu substrates (*Alfa Aesar 13382*) and coupling them to PyprPA:CuO films on glass. The CNTs synthesis procedure was identical to that described in section 3.1 except 100 nm of Ni was added to the bottom of the catalyst stack as a diffusion barrier. Current-voltage scans were conducted using a 2-probe technique by contacting the Cu growth substrate and modified Cu surface, as illustrated in Figure 5.6(a). As such the measurement includes contributions from the oxidized Cu film, CNT forest, Cu growth substrate and all intermediate interfaces; hence, it is not meaningful to extract the resistance from this data. Furthermore, the measurement is sensitive to the separation distance between the probes and the pressure applied to them. Care was taken to place the probes as consistently as possible; however, it was not precisely controlled. Coupling the CNT tip interface with a monolayer of PyprPA reduced the total electrical resistance by approximately 90% over dry contact, shown in Figure 5.6(b). The reduction in electrical resistance was approximately 85% for samples that were not sonicated to facilitate the presence of a monolayer of PyprPA in the interface. All PyprPA coupled interfaces displayed a linear

relationship, suggestive of ohmic behavior, over the scan range from –0.45 to + 0.45 V and therefore might be useful for CNT interconnects.

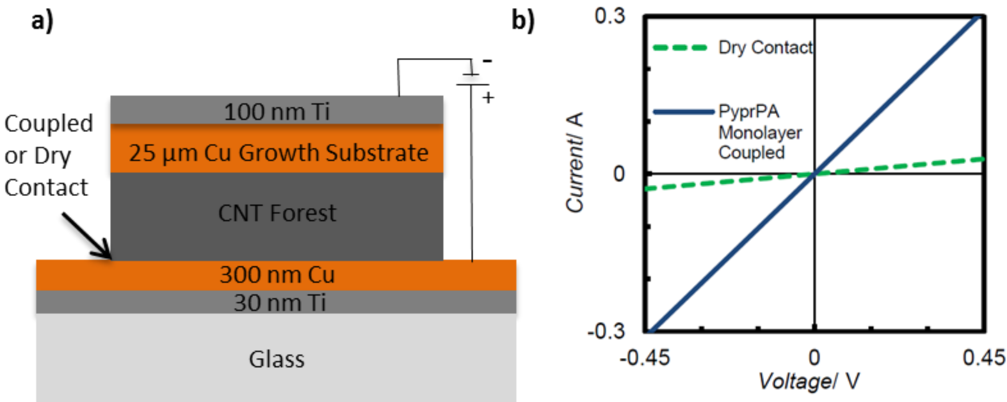

Figure 5.7: (a) Sample configuration for 2-probe electrical characterization of CNT-PyprPA:CuO coupled interfaces. **(b)** Current-voltage scan illustrating a ~90% reduction in electrical resistance for PyprPA coupled interfaces over dry contact interfaces.

5.6 Exploration of Additional Modifiers

Coupling of CNTs to metal oxide surfaces with several additional modifiers was explored and is summarized in detail in Appendix B. For these studies the CNT forests were conformally coated with a few nm of Al_2O_3 using atomic layer deposition (ALD) to facilitate covalent bonding at both ends of the modifier with phosphonic acids. Coating the CNT forests with Al_2O_3 also increases the effective electrical resistivity of the forest, which is attractive for applications where an electrically insulating TIM is required.

Two different approaches were considered for covalently linking oxide coated CNTs to metal-oxide surfaces. The first, *Strategy 1*, centered on using linear carbon molecules terminated at each end with a phosphonic acid functionality, which we refer to as a Bisphosphonic acid (BisPA). From the plethora of possible BisPA molecules a (1,4-phenylenebis(methylene))diphosphonic acid (Benzene-BisPA) and a 1,8-Octanediphosphonic

acid (Octane-BisPA) were selected for testing and are illustrated in Figure 5.8(a) and (b). The selection of these two molecules was motivated by the differences in the length of their carbon backbones. The second strategy, *Strategy 2*, involved using two different phosphonic acid terminated molecules to separately modify the oxide coated CNTs and the metal oxide surface, and to then join them via a reaction between the opposing terminations of the two modifiers (Figure 5.8(c)). Specifically, an acrylate-phosphonic acid (Acrylate-PA), CH_2=CH-C(O)O$(CH_2)_{11}PO_3H_2$, and 3-aminopropylphosphonic acid (Amino-PA), $NH_2(CH_2)_3PO_3H_2$, were used to separately modify the oxide coated metal and CNTs, respectively. The two modified surfaces are then brought into contact and joined through Michael-addition between terminal amine and acrylate functionalities [141].

Despite trying a number of modification and bonding procedures the BisPA modifiers (*Strategy 1*) failed to produce noticeable coupling between Al_2O_3 coated CNT forests and Al_2O_3 coated Ag foil. It was found that both BisPA moieties bound to the same surface and failed to bridge the interface. On the other hand, the modification and reaction procedure utilizing acrylate and amino molecules containing phosphonic acid functional groups (*Strategy 2*) was found to successfully bond the interface. In doing so, the procedure reduced the total thermal resistance from roughly 50 to 10 mm^2-K/W, suggesting that the strategy might be used to produce low thermal resistance electrically insulating TIMs, a niche for which there currently aren't any commercial products available. Future research should continue to examine different modifiers and coupling strategies with a focus on gaining a detailed scientific understanding of the chemical linking and the thermal transport across such junctions. Additional studies should also be undertaken to understand the reliability of surface modifier coupled TIMs.

Figure 5.8: (a) Benzene-BisPA, **(b)** Octane-BisPA modifiers used in Strategy 1; **(c)** Strategy 2

5.7 Summary

A pyrenypropyl phosphonic acid modifier was created for coupling CNTs to metal oxide surfaces in a simple and scalable manner to reduce the thermal contact resistance. When used to couple vertical CNT forests to oxidized Cu surfaces the PyprPA modifier reduced the thermal contact resistance by approximately 9-fold over CNT forests in non-bonded dry contact. As a thermal interface material PyprPA coupled CNT forests had a thermal resistance of 4.6 ± 0.5 mm^2-K/W, which is on par with the resistance of conventional thin-film metallic solders [47]. Electrical characterization of PyprPA coupled and dry contact CNT interfaces indicate that the modifier may reduce the electrical contact resistance by a similar magnitude. The results of this work highlight the important role of bond strength in thermal transport at CNT contacts. Furthermore, it demonstrates that surface modifiers, such as the one synthesized here, could be used with relatively simple and repeatable processing steps to significantly reduce contact resistances in CNT based architectures for thermal and electrical transport.

CHAPTER 6

BONDING WITH NANOSCALE POLYMER COATINGS

6.1 Introduction

Previous efforts to bond CNT forests to interfaces and mitigate the contact resistance have focused on using metallic films [32, 34, 35] as a bonding agent (see section 1.3). While these approaches have in some cases produced CNT TIMs with thermal resistances approaching those of conventional TIMs, they often require expensive materials, such as Au or In, and processing, including metal thin film deposition and high temperature and high pressure bonding, that are not favorable for large-scale commercial production. In contrast with metals, polymers are, in most cases, a low-energy and low-cost material to manufacture. Polymers are amenable to both solution-based processing and melt processing at reduced temperatures. This research explores a potentially scalable and low cost process that utilizes spray coating to deposit thin polymer coatings onto the tips of CNT forests for bonding at room temperature.

Although polymers are advantageous for facile processing, bulk polymers, unlike metals, are considered to be thermal insulators with thermal conductivities typically on the order of 0.1 W/m-K. To effectively overcome the contact resistance at the CNT forest tip interface as thin a layer of polymer as possible should be used. Spray coating was examined because of the ability to precisely control the amount of polymer deposited onto the CNTs, the ease with which the process can be scaled, and because it was expected to minimally alter/damage the morphology of the CNT forest. Two polymer systems were studied: the first, polystyrene (PS) was chosen since it is a low cost widely used aromatic polymer that is chemically stable at device operating temperatures [142]; the second, poly(3-hexylthiophene) (P3HT) was chosen because it has been shown to interact strongly with CNTs through π–π bonding and by preferentially wrapping around the nanotube axis [143-145]. Additionally, due to its conjugated back bone, P3HT is

chemically stable at higher temperatures as compared to PS [146]. The height of the CNT forest and the quantity of polymer sprayed were varied individually in an effort to understand their influence on the thermal resistance of the interface. To demonstrate how the spray coating process might be scaled for commercial production, CNT forests were grown on both sides of Al foil to create a thermal interposer, as described in section 3.1, similar to that created by Cola et al. [94]. The CNT coated foil interposer eliminates the necessity to grow or transfer print CNTs directly onto the back of the chip or packaging. The CNT growth and spray coating process can instead take place separately on the metal foil, before being incorporated into the electronic package.

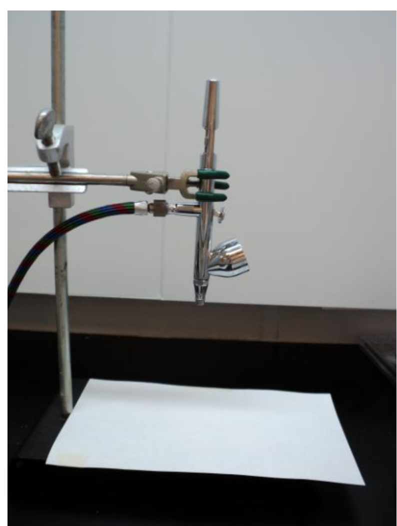

Figure 6.1: Airbrush used to deposit nanoscale polymer coatings onto CNT forests.

6.2 Polymer Coating and Bonding of CNT Forests

6.2.1 Coating and Bonding Procedure

For spray coating polymer solutions, 0.5 mg/mL of P3HT (*regioregular, Sigma Aldrich 445703*) or PS (*MW 35000, Sigma Aldrich 331651*) were prepared by sonicating or stirring for five minutes into $CHCl_3$. The solutions were sprayed in one mL increments onto the CNT tips using an airbrush (*Iwata Eclipse HP-CS Gravity Feed*) with 280 kPa N_2 as the carrier gas. The airbrush

was positioned 10 cm above the CNT forest so that the conical spray profile of the airbrush deposited polymer over an area slightly larger than the area of the CNT forest sample, and is shown in Figure 6.1. It is difficult to quantify the amount of polymer deposited onto the CNT forest for each 1 mL spray; therefore we refer to the quantity of polymer applied to each CNT forest in terms of the number of 1 mL sprays. The number of sprays was altered among 1, 2, and 5 in order to examine the effects of the quantity of polymer on the resultant thermal resistance of the bonded CNTs. Spray coated CNTs on Si substrates were bonded to 1 cm^2 pieces of 25 μm thick Ag foil for thermal characterization with photoacoustic. To bond the polymer coated CNT forests to the Ag foil, the CNT forests were first wet with a few droplets of $CHCl_3$ to reflow the polymer, and then promptly placed into contact with the Ag foil under 140 kPa of pressure. The interface was allowed to dry for at least 5 hours under ambient conditions before the load was removed. The entire spray coating and bonding process is shown schematically in Figure 6.2. In a process similar to that described above, both sides of the CNT coated foil interposer structures were bonded between quartz substrates and Ag foil. However, the bonding pressure was increased to 580 kPa to observe the maximum potential of the structure. In addition to bonded interfaces, two other sample configurations were studied in an effort to better understand the effects of the polymer on the interface resistance: *i)* dry contact: as grown bare CNT forests in dry contact with the Ag foil; and *ii)* polymer coated dry contact: CNT forests spray coated with varying quantities of polymer that were allowed to dry before being placed into dry contact with the Ag foil.

6.2.2 Characteristics of Coated CNT Forests

As is shown in Figure 6.3, the spray coating process restricts the deposition of polymer to the CNT tips and limits clumping due to capillary forces associated with the drying of the solvent. An SEM (*Hitachi 4700 FE*) was used to observe the extent of CNT clumping due to capillary interactions for forests both dip coated and spray coated with polymer. Figure 6.4 shows that spray coating restricted clumping to only the tips of the CNTs, whereas dip coated caused

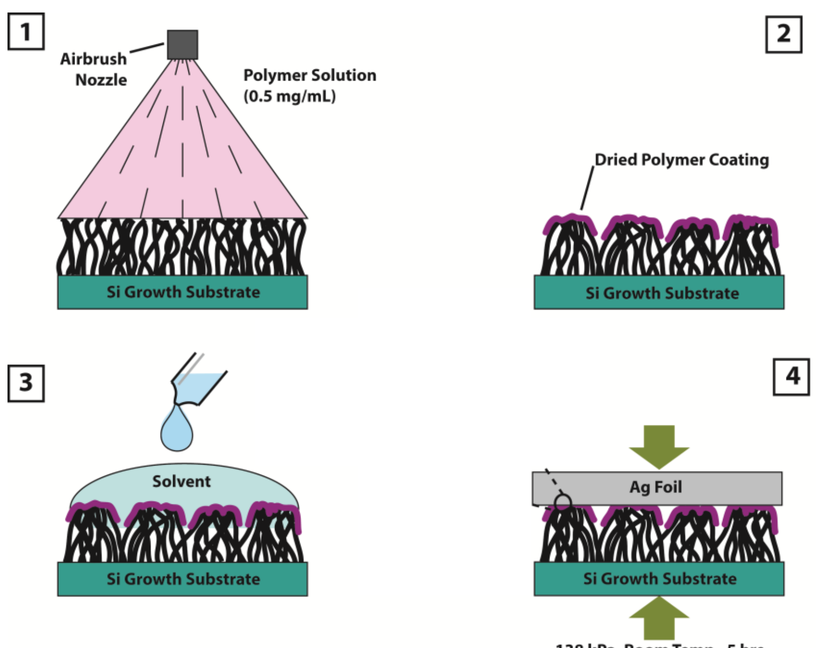

Figure 6.2: Illustration of the polymer spray coating and bonding process. (1) Spray deposition of polymer onto the top of the CNT forest. (2) The polymer coating dries, causing clumping of the CNT tips. (3) Solvent ($CHCl_3$) is applied to the top of the CNT forest to wet and reflow the polymer coating. (4) Still wet polymer coating is brought into contact with Ag foil and placed under 140 kPa of pressure for 5 h while the interface dries.

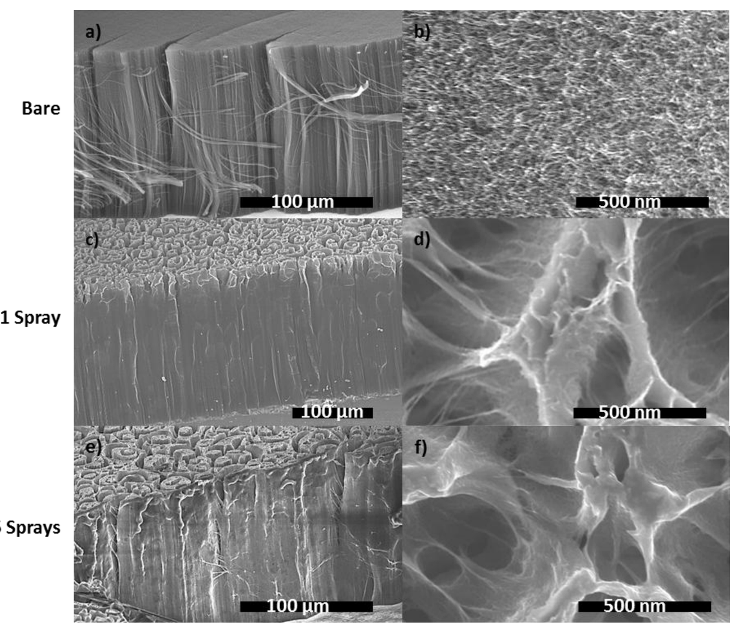

Figure 6.3: SEM images of bare and polymer spray coated CNT forests. The spray coating process deposits nanoscale coatings of polymer to the tips and sides of the CNT forest. The amount of polymer visible on the CNT forests increases with the number of sprays. No morphological differences were observable between PS and P3HT. **(c)** and **(e)** were spray coated with P3HT, and **(d)** and **(f)** were spray coated with PS.

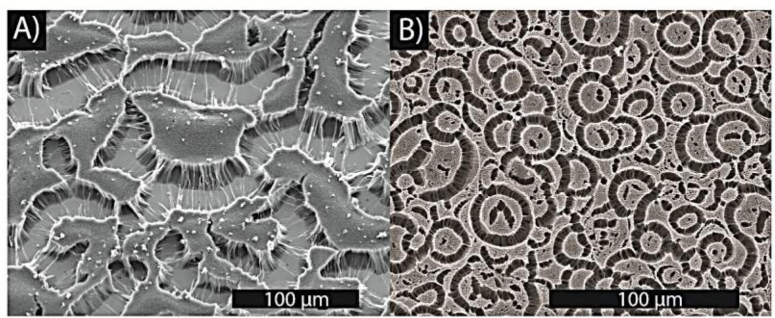

Figure 6.4: SEM images of a polymer **(a)** dip coated, and **(b)** spray coated CNT forest showing that spray coating reduces capillary driven clumping of CNTs. Clumping due to capillary forces in dip coated samples leads to CNT tear out at the growth substrate.

clumping along the entire height of the forest and even resulted in sections of CNTs being torn from the growth substrate. TEM analysis (*JEOL 4000EX*) was conducted on several polymer bonded samples after undergoing PA characterization to observe the CNT-polymer interaction. Samples were prepared by peeling away the Ag foil to expose the CNT forest, and then scraping the exposed forest off the Si substrate and into dimethylformamide (DMF). Neither PS nor P3HT were observed to be soluble in DMF. The solutions were sonicated for roughly one hour to disperse the CNTs before being dropcast onto a carbon TEM grid and allowed to dry. For CNT forests that had been bonded with P3HT polymer chains were observed to wrap around the CNT, shown in Figure 6.5, demonstrating that spray coating and bonding process supported the formation π-π interactions between the P3HT and CNTs. This coincides with prior observations of strong affinity between CNTs and P3HT [143-145].

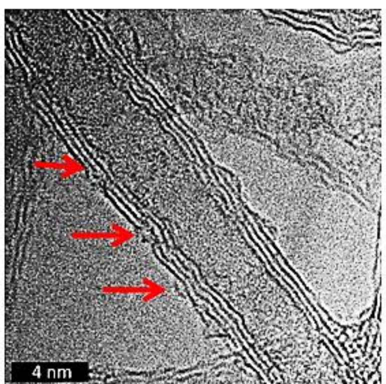

Figure 6.5: TEM image showing a P3HT chain wrapped around a CNT.

6.3 Results

6.3.1 Thermal Resistance of Polymer Coated and Bonded CNT Forests

The total thermal resistance for all three sample configurations (dry contact, polymer coated dry contact, and polymer bonded) is shown in Figure 6.6. Each of these total resistances is the sum of the contact resistance at the CNT tips, the intrinsic thermal resistance of the CNT forest, and the contact resistance at the CNT growth substrate. Measurements for all three sample configurations were conducted at PA cell pressures of both 7 and 140 kPa. All results for the dry contact sample configurations shown in Figure 6.6 are those collected at a cell pressure of 140 kPa. Data collected on dry contact and polymer coated dry contact samples at 7 kPa were inconsistent, likely due to inconsistent and/or poor contact conditions at the interface under this light load. The data collected on bonded samples did not exhibit significant changes with the pressure in the PA cell, indicative of a well-bonded interface, and are shown at 7 kPa in Figures 6.6(b) and (c). All of the data from Figure 6.6(a) for samples less than 125 μm in height are shown in Figures 6.6(b) and (c) for comparison. These data are labeled as 'Dry Contact', although the set includes both the dry contact and the polymer coated dry contact data. The thermal resistance increases with CNT height for all sample configurations. The thermal resistance of polymer coated dry contact samples was higher than those of all but one of the bare CNT dry contact samples. Because the nanoscale polymer coating has relatively negligible thermal resistance, the difference in

performance likely stems from the fact that adding the dried coating of polymer to the interface stiffens the top of the forest, effectively reducing the extent to which it conforms to the Ag foil. This reduces the contact area and increases the thermal contact resistance.

Bonding with both P3HT and PS reduced the thermal resistance of the interface, with the largest reductions occurring at the tallest forest heights. For example, a 58% reduction was observed for PS bonding of forests 115 μm in height. The polymer bonded samples exhibited a weak trend of increased thermal resistance with the number of sprays. However, the trend is considered to be of low significance because it is violated for several samples, and because the

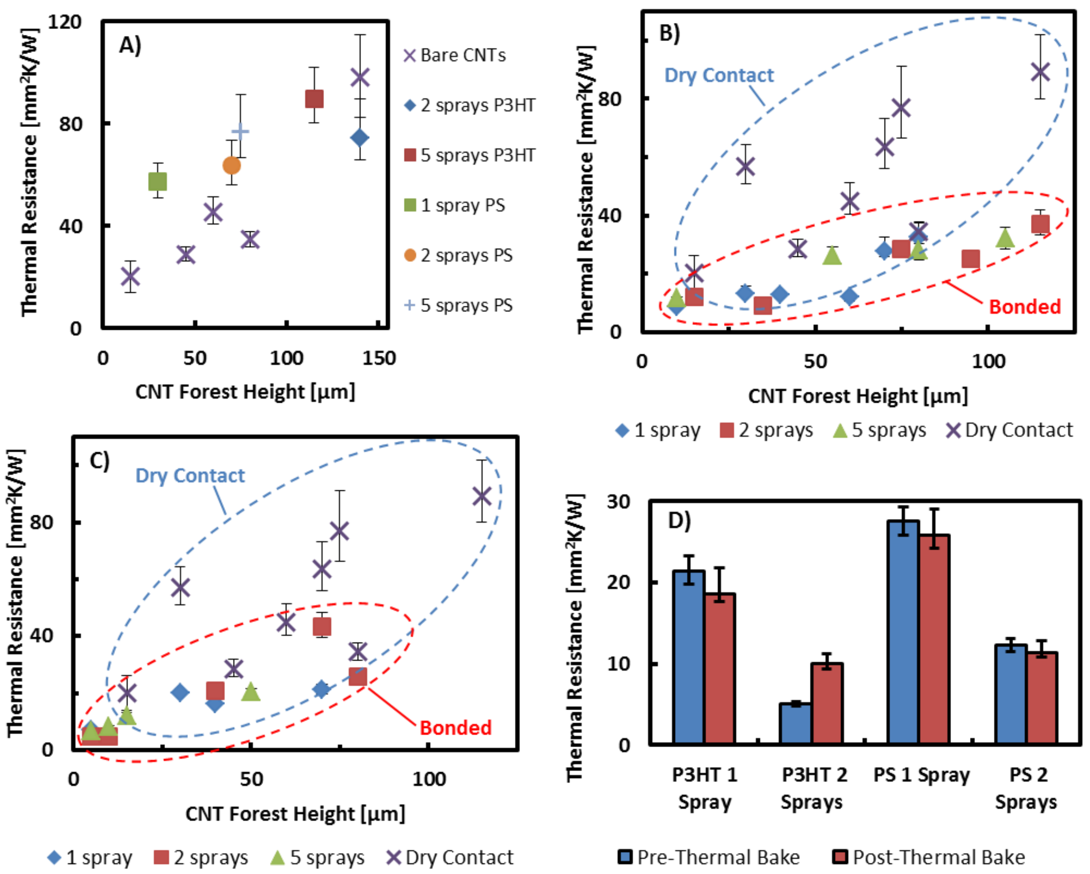

Figure 6.6: (a) Thermal resistance of polymer coated and bare CNT arrays in dry contact. **(b)** Thermal resistance of PS bonded interfaces (PA cell pressure = 7 kPa) compared to the dry contact interfaces (PA cell pressure = 140 kPa). **(c)** Thermal resistance of P3HT bonded interfaces (PA cell pressure = 7 kPa) compared to dry contact interfaces (PA cell pressure = 140 kPa). **(d)** Thermal resistance of polymer bonded samples before and after being baked at 130 °C for 110 h.

magnitude of the differences in resistance with number of sprays is of similar order to the distribution of the data. Overall, bonding with both P3HT and PS was observed to decrease the resistance of CNT forests comparably, ruling out any contributions from polymer structure or differences in the nature of the polymer–CNT interactions. The lowest measured resistances for P3HT bonded, PS bonded, and bare CNT dry contact samples were 4.9 ± 0.3 mm^2-K/W (10 μm tall forest with two sprays), 8.5 ± 0.5 mm^2-K/W (10 μm tall forest with one spray), 20 ± 6 mm^2-K/W (15 μm tall forest), respectively. The reported PA measurement uncertainties have contributions from both the resolution of the experimental setup, estimated to be ± 1° in the measured phase shift, and the repeatability, i.e. variations in the thermal resistance at different measurement locations on a sample. The error bars include contributions from both sources for the dry contact and polymer coated dry contact data. The error bars represent only the resolution of the measurement technique for bonded samples and are too small to be seen for the majority of the data points. The uncertainty associated with repeatability is captured by the distribution of the data for bonded samples.

6.3.2 Thermal Stability of Polymer Coated and Bonded CNT Forests

Thermal degradation, due to chemical stability of the polymers at elevated temperatures, is also a significant concern for polymer based TIMs [147]. Hence, four of the samples, two P3HT bonded and two PS bonded, were subsequently thermally baked at 130 °C and 680 mbar for 110 hours in a vacuum oven to mimic high temperature operating conditions. There was no statistically significant change in the thermal resistance of the samples between before and after baking (Figure 6.6(d)) for three of the four sample types tested. There was a slight increase in the thermal resistance of the two-spray P3HT sample after thermal baking. Both PS and P3HT have been demonstrated to be chemically stable at temperatures above 130 °C [142, 146], so the increase in resistance observed for the two-spray P3HT samples is likely due to other factors such as local spot-to-spot variation in the CNT forest morphology or local delamination of the interface bond

during sample handling. The overall results from thermal baking suggest that the polymer coatings used here are stable over the temperature range studied and that the process may be suitable for integration with high power density devices.

6.3.3 Polymer Coated and Bonded Thermal Interposers

The thermal resistances of bare CNT coated foil interposers in a dry contact arrangement were measured to be 21 ± 4 mm^2-K/W. The thermal resistances of interposers spray coated and bonded with one spray of P3HT were measured to be 9 ± 2 mm^2-K/W; this is an approximate two-fold decrease in resistance. Three samples of each configuration were produced and the uncertainty in the thermal resistance was dominated by the variability between samples.

6.3.4 Shear Adhesion

To measure the attachment strength CNT forests were spray coated and bonded with 2 sprays of P3HT to glass slides coated with 300nm of Ag for consistency with the PA experiments. The shear attachment strength was measured using a die shear apparatus (*Nordson DAGE 4000*), as illustrated in Figure 6.7. All samples failed at the polymer interface and the average shear attachment strength was measured to be 29 N/cm^2.

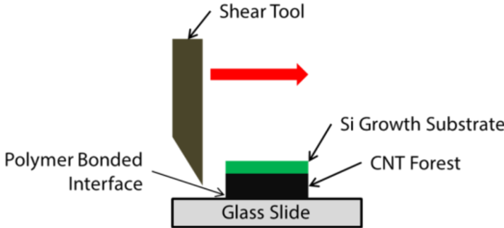

Figure 6.7: Schematic of the die shear apparatus and sample configuration used to measure the shear attachment strength of polymer spray coated and bonded interfaces.

6.4 Analysis

6.4.1 Effect of CNT Forest Height

The thermal resistance increased with increasing CNT forest height for each of the sample configurations studied. One cause for the observed trend is apparent: increasing the height of the

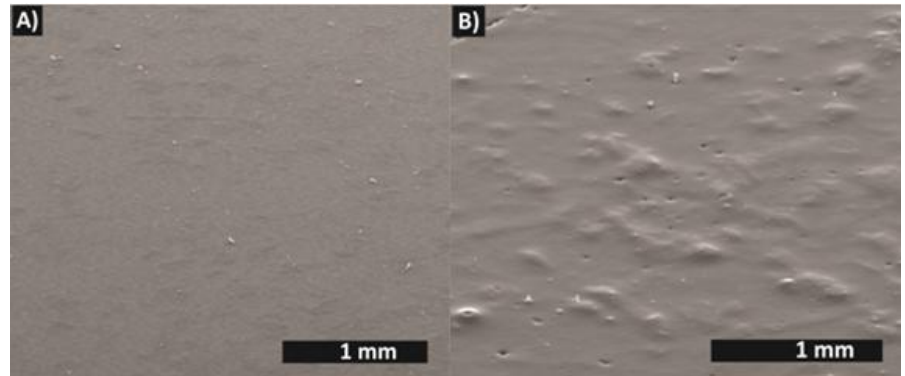

Figure 6.8: SEM images comparing the surface roughness of short and tall CNT forests. (a) Top view of a 5 μm tall forest, and (b) top view of a 70 μm tall forest.

CNT forest increases the amount of material through which the heat must travel, hence increasing the resistance of the CNT layer itself. A second cause is more subtle and is specific to the CNT growth process. During CNT growth, certain regions of the forest grow at greater or lesser rates compared to the average growth rate due to slight discrepancies in the condition of the catalyst particles and their access to the carbon gas source. As the forest grows, the difference in height between the different growth-rate regions is increased, resulting in decreased height uniformity with growth time. The decreased uniformity of the CNT forest is equivalent to an increase in the surface roughness of the CNT forest. This increase in surface roughness can be observed in Figure 6.8, and may lead to a decrease in the contact area at the interface. Additional factors related to growth process, such as CNT pullout at the growth substrate and changes in morphology with growth time, may also contribute to increases in the thermal resistance with increasing forest height [82]. Since the polymer spray coating process was only observed to apply polymer to the CNT tips, it is reasonable to assume that the bonding process only leads to significant changes in the thermal contact resistance at the CNT tips, and that the thermal resistance of the CNT forest and the thermal contact resistance at the growth substrate are not affected significantly.

6.4.2 Thermal Transport at Polymer Coated CNT Contacts

To better understand the source of the reduction in the thermal resistance, we consider how the polymer might affect the heat transfer between a single CNT in side contact with the Ag foil [44], as shown in Figure 6.9(c). To observe the structure of bonded interfaces, spray coated CNT forests were bonded to Si substrates, to which the adhesion was negligible, then disassembled and examined using SEM (Figure 6.9(a) and (b)). On the basis of the SEM images, the configuration of a polymer bonded CNT, shown in Figure 6.9(d), was assumed for the subsequent theoretical heat transfer analysis. Heat transfer for the case without any polymer has been analyzed by several investigators and was reviewed in Chapter 2 section 3. It was shown that due to the nm dimensions of the CNT contacts ballistic effects must be considered [38, 44]. The ballistic resistance describes the flow of phonons through the contact as free molecular flow through an orifice with a transmission coefficient derived from diffuse mismatch assumptions and Chen's gray medium approach [148]. The contact area normalized ballistic resistance, R_b, is given by Equation 2.16. Taking $v_{g,CNT}$ = 1000 m/s as the through basal plane velocity for graphite [40], $C_{l,CNT}$ = 1582 kJ/m^3-K, $v_{g,Ag}$ = 1640 m/s, and $C_{l,Ag}$ = 2362 kJ/m3-K [149, 150], the resistance for a single Ag–CNT contact is $R_{b,Ag-CNT}$ = 3.6x10^{-3} mm^2-K/W. When polymer is added as is shown in Figure 6.9(d), the resistance of the interface can be approximated by the sum of the ballistic resistance between the Ag and the polymer, the ballistic resistance between the polymer and the CNT, and the resistance of the polymer layer itself. The contact area normalized resistance of the polymer layer is given by the classical expression $R_{poly}=l/k_{poly}$, where l is the thickness of the polymer layer and k_{poly} is the polymer thermal conductivity. Assuming l = 10 nm which is reasonable on the basis of the polymer accumulation observed at CNT tips in Figures 6.9(a) and (b), and taking PS as the polymer since its properties are widely known, k_{PS} = 0.25 W/m-K, the contact area normalized resistance for a polymer coated CNT becomes $R_{Ag-PS-CNT}$ = 4.6x10^{-2} mm^2-K/W. This result indicates that under the prescribed assumptions the polymer actually increases

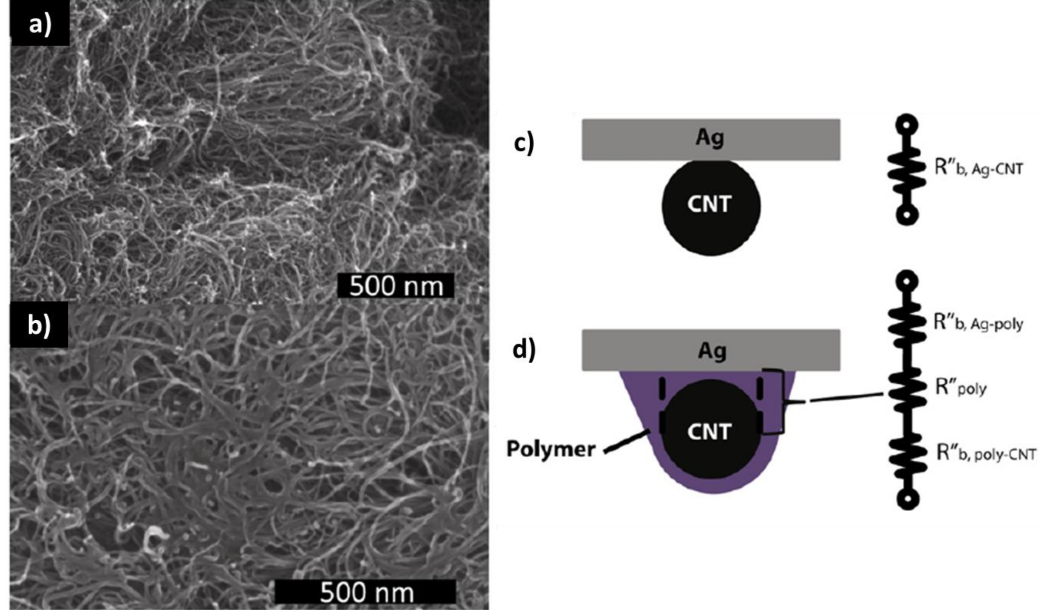

Figure 6.9: (a) SEM image of the top of a CNT forest after one spray of P3HT and bonding. **(b)** SEM image of the top of a CNT forest after five sprays of P3HT and bonding. **(c)** and **(d)** Illustrations of CNT dry contact and polymer bonded contact configurations respectively and the associated thermal resistance network.

the contact area normalized thermal resistance by an order of magnitude. The resistance of the polymer layer, R_{poly}, causes most of this increase because of its low thermal conductivity. Therefore, adding the polymer must increase the contact area by greater than an order of magnitude as compared to CNT dry contact to reduce the total resistance of the interface. This requires a contact area enhancement greater than the 70-80% achieved by wet compression in Chapter 4. Assuming a vdW interaction and elastic contact, a CNT with a diameter of 8 nm will only have a contact width of approximately 1 nm with the Ag foil (detailed in section 2.3.1) [40, 84]. Should the polymer fill the interstitial space between the CNT and the foil to the extent of the CNT diameter, it would increase the contact area by an additional factor of 8.

Measurements of the shear attachment strength of CNT forests that were polymer bonded to glass slides coated with Ag revealed an average attachment strength of 290 kPa (29 N/cm^2). This is a more than threefold increase over reported values for shear attachment strength of CNTs

in dry contact with glass slides [126]. The increase in attachment strength from polymer bonding corresponds to an increase in area that is similar in magnitude to the increase in area that would be achieved from filling the space between the CNT and Ag with polymer (Figure 6.8). This suggests that adding the polymer might increase the contact area in this manner. Furthermore, Cola et al estimated that the real contact area in CNT forest TIMs is only ~1% of the apparent area [44]. Similarly, Panzer et al. estimated that only 0.35% of the volume fraction of CNT forests effectively participate in heat transfer in CNT forest TIMs [45]. Therefore, the polymer might also increase the contact area by engaging additional CNTs near to, but not in contact with the Ag foil. As was pointed out in Chapter 2, in the above calculations the ballistic resistance assumes that the interface is bonded perfectly. This assumption is clearly not valid for the weak vdW interactions present at both the dry contact and polymer bonded interfaces. As a result, the above calculations for the CNT–Ag, CNT–polymer, and Ag–polymer contacts underpredict the thermal resistance significantly. The actual resistances of the contacts might be one to two orders of magnitude higher than the estimates based on perfect bonding, because phonon transmission is attenuated by weak interfacial bonding [78, 79]. As a result, the resistance of the polymer layer, R_{poly}, at a thickness of 10 nm would be on par with or an order of magnitude less than the thermal resistances of vdW contacts. The higher end of the expected surface resistance considering vdW bonding would allow the polymer layer to be as thick as several 100 nm without dominating the total resistance at CNT–polymer–Ag contacts; the polymer layer could be even thicker if its bulk thermal conductivity was enhanced by nanostructuring [151-153]. While it is difficult to accurately calculate or measure the thermal resistance of a CNT tip in both dry contact and polymer bonded arrangements, the simple analysis presented here has shown that adding polymer does not reduce the area normalized thermal resistance of CNT contacts; it instead extends the area available for heat transfer at the contacts to CNT tips.

6.5 Summary and Recommendations

Polymer spray coating and bonding was demonstrated as an effective means for increasing the contact area and reducing the thermal resistance of CNT forest thermal interfaces. In addition to the contact area enhancements from wet-compression (Chapter 4) the bonding process added nanoscale coatings of polymer around individual CNT contacts to locally increase contact area, and potentially penetrated into the forest to engage additional CNTs close to the interface to further increase the contact area. Spray coating with polystyrene and poly(3-hexylthiophene) produced CNT TIMs with thermal resistances of 8.5 ± 0.5 and 4.9 ± 0.3 mm^2-K/W respectively, comparable to conventional solder TIMs. The thermal resistances did not change significantly after baking at 130 °C for 110 hours. The thermal resistances of dry and polymer bonded CNT interfaces were found by PA measurement to increase with CNT forest height because of the increased surface roughness of taller forests. The relatively low cost of polystyrene in addition to favorable bonding conditions, i.e. room temperature and low pressure (140 kPa), make the spray coating and bonding process attractive for large-scale implementation. As a demonstration of how the process might be scaled, CNT forests were grown on both sides of Al foil to create an interposer material with a thermal resistance of 9 ± 2 mm^2-K/W when bonded.

While these results demonstrate that the polymer spray coating and bonding process can be a viable method for reducing the thermal resistance of CNT forest contacts, the results were challenging to reproduce with rigid opposing substrates. Specifically, it was difficult to achieve strong uniform bonding between CNT forests coated with polymer and rigid metal surfaces for thermal characterization with an ASTM D5470 [55]. Future research should focus on improving the robustness of this approach through process optimization, improved process control, and the identification of soluble polymers with excellent adhesion to a variety of metal and semiconductor surfaces.

CHAPTER 7

RESOLVING THE CNT FOREST TIP INTERFACE RESISTANCE WITH TIME-DOMAIN THERMOREFLECTANCE

7.1 Introduction

Up to this point PA has been used to measure the total thermal resistance of CNT forests – that is, the sum of the contact resistances at the growth substrate and free tip interfaces, plus the resistance of the CNT layer. The heating frequencies suitable for the PA technique correspond to thermal penetration depths (Equation 3.1) that profile the entire CNT forest TIM structure, shown again for convenience in Figure 7.1(a). Consequently, the PA measurement signal depends on the thermal properties of the Ti absorption layer, Ag foil, and CNT forest as well as the thermal resistance between those layers and at the Si growth substrate interface. Many of these properties are unknown or difficult to measure. In the PA measurements of this research the Ti-Ag, Ag-CNT, and CNT-Si interface resistances, and the thermal conductivity, heat capacity, and thickness (height) of the CNT forest layer were all treated as unknowns when fitting the theoretical model to the data. Since the PA method is sensitive to each of these parameters they could not be identified on an individual basis. Instead a unique solution could only be obtained for the total resistance, a lumped parameter (shown in section 3.2.1).

To measure the thermal resistance at the CNT tip interface exclusively, and more rigorously assess the merits of the strategies developed in this work, TDTR is used. The modulation frequencies applicable for TDTR, typically 1-10 MHz, correspond to thermal penetration depths on the order of 0.1-10 μm, and are favorable for interrogating thermal transport at interfaces. In particular, TDTR is well-suited to characterize the interface between the metal transducer layer and the sample [69, 79, 104, 105]. Here it is used to characterize the interface between CNT forests and an Al transducer layer, as shown in Figure 7.1(b).

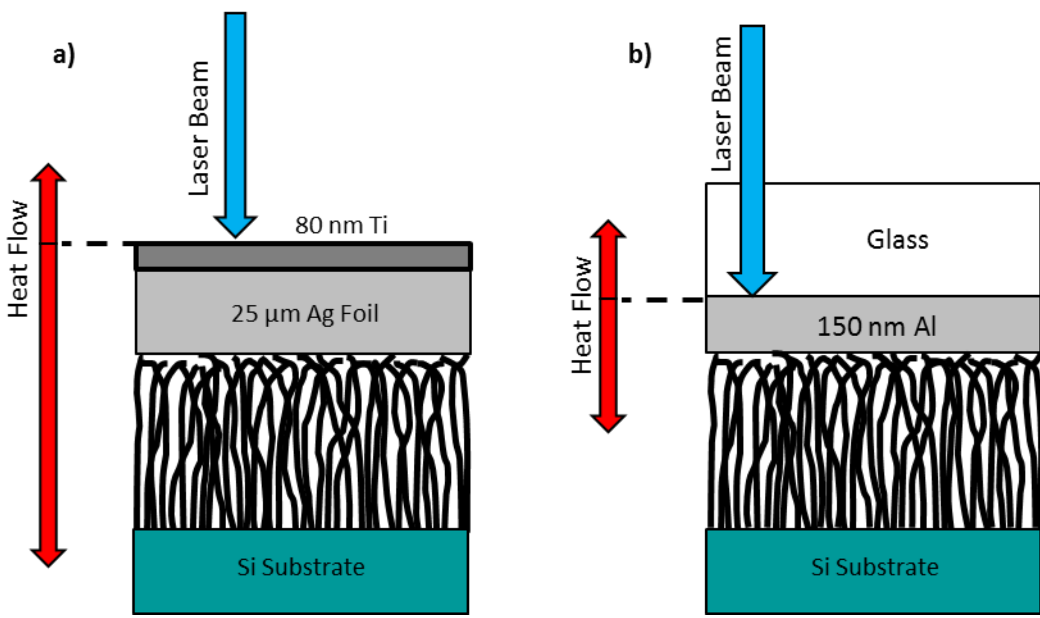

Figure 7.1: Sample configuration for **(a)** PA and **(b)** TDTR of CNT forests.

Specifically, it is used to resolve the thermal contact resistance of CNT forest-Al interfaces that have been processed using the methods developed in Chapters 4, 5, and 6.

7.2 TDTR of CNT Forest Contacts

7.2.1 Samples

A total of four CNT forest sample types were evaluated with TDTR; *i)* dry contact, *ii)* WCD (Chapter 4), *iii)* PyprPA monolayer coupled (Chapter 5), and *iv*) P3HT spray coated and bonded (Chapter 6). These samples were assembled from 30 µm tall CNT forests grown on 1 cm^2 Si substrates using the recipe described in section 3.1, and the sample configuration described in 3.2.2 and shown in Figure 7.1(b) above. The dry contact CNT forests were characterized at compressive pressures of 90-220 kPa. One of the dry CNT forests were then wet with hexane, while remaining compressed at 220 kPa and allowed to dry for over 5 hours to be characterized as a WCD sample. PyprPA samples were fabricated using the procedure outlined in Chapter 5 for samples coupled with a monolayer of PyprPA and solvent. The only differences being that the modification was executed on the Al-glass transducer substrates, without plasma pretreatment,

and at a bonding pressure of 300 kPa. The P3HT bonded samples were prepared using the procedure detailed in Chapter 6 with two sprays of P3HT and bonding at 300 kPa.

7.2.2 Measurement Strategy

To reduce the number of fitting parameters in the measurement of CNT forest contacts TDTR was first carried out on the Al coated glass slides to determine the thermal conductivity and heat capacity of the glass in addition to the thermal interface resistance between the Al and glass. Measurements of Al coated glass were conducted at two modulation frequencies, 1.2 and 3.6 MHz with the intent of identifying both the thermal conductivity and heat capacity of the glass [108, 109]. In total over 25 TDTR scans were performed across multiple Al-glass samples and multiple locations on each sample. Once the properties of the Al-glass structure were determined TDTR scans were conducted on CNT forest samples WCD with hexane and bonded with PyprPA and P3HT at modulation frequencies of 1.2, 3.6, and 6.3 MHz to measure the interface resistance between the CNT forest and Al, as well as the CNT forest thermal conductivity and heat capacity.

In addition to the thermal properties of the glass and CNT forest layers and their interfaces TDTR measurements are also sensitive to thickness of the Al transducer layer. In fact, measurements are typically most sensitive to this parameter [154]. All of the Al transducers used in this work were deposited using electron beam evaporation during the same deposition to minimize variations in the film thickness and properties. An Al film thickness of 150 nm was targeted to ensure the formation a continuous opaque film. The film thicknesses were measured using a stylus profilometer (*KLA-Tencor P-15*) with a resolution of less than 0.1 nm. 55 step-edge measurements of the Al film revealed an average thickness of 150 nm with a standard deviation of 10 nm. Determination of the Al thickness using picosecond acoustics was attempted, however, no acoustic echo was observed, likely due to the low acoustic impedance mismatch between glass and Al [155].

7.2.3 Data Fitting

Data fitting was conducted using a Levenberg-Marquardt non-linear least squares method [98]. For the glass-Al samples the fitting parameters were the thermal conductivity and heat capacity of the glass and the thermal interface resistance between the Al and glass layers. The initial values and bounds used to fit for those parameters are given in Table 7.1. All other parameters were considered known and held constant throughout data fitting. The uncertainty in the thickness of the Al layer was propagated into the uncertainty in the unknown fitting parameters after data fitting. A layer of air with properties at 300 K and 100 kPa was included in the model on the backside of the Al layer to account for the possibility of heat leakage into the ambient, although it has been shown previously that the Al-air interface can be modeled as an adiabatic boundary without a loss in accuracy [103].

Table 7.1: Initial guess values and bounds for data fitting.

Glass-Aluminum-Air			
Parameter	Initial	Lower Bound	Upper Bound
k_{Glass} [W/m-K]	1.2	0.8	1.5
C_{Glass} [kJ/m^3-K]	1650	1100	1980
$R_{Glass\text{-}Al}$ [mm^2-K/W]	.01	.002	0.2
Glass-Aluminum-CNT Forest			
k_{CNT} [W/m-K]	3.5	0.1	10
C_{CNT} [kJ/m^3-K]	21	.03	60
$R_{Al\text{-}CNT}$ [mm^2-K/W]	1	0.1	100

For the glass-Al-CNT samples the fitting parameters were the thermal conductivity and heat capacity of the CNT layer and the thermal interface resistance between the CNT forest and Al layers. The initial values and bounds used to fit for those parameters are also given in Table 7.1. The initial guess value for the CNT forest thermal conductivity was taken from recent measurements of CNT forests similar to those used in this work [123, 156]. The initial guess value for the heat capacity was set as the product of the specific heat of graphite [157] and the mass density of CNT forests similar to those used in this work [158]. The bounds for these

parameters were set to encompass the full range of reported CNT properties [18]. As with the glass-Al samples all other parameters in the model were considered to be known.

7.3 Measurement Sensitivity and Uncertainty

With the relatively large number of fitting parameters and the varying sensitivity of the measurement to those parameters, understanding the uncertainty in the measurement is essential. The impact a parameter has on the measurement signal is described the sensitivity. The sensitivity to a parameter represents the percentage change in the measurement signal per percentage change in the parameter. If the sensitivity to a parameter is comparatively small, it will have less influence on the signal than other parameters in the system. In an ideal experiment the parameter with the highest sensitivity is the unknown parameter of interest. Formally, the sensitivity for a parameter p, denoted as S_p, in a TDTR experiment is calculated as

$$S_p = \frac{\partial \ln(V_{in}/V_{out})}{\partial \ln(p)}, \tag{7.1}$$

where V_{in}/V_{out} is the ratio of the in-phase and out-of-phase signal [102, 110].

There are typically two sources of uncertainty in a TDTR experiment; *i)* uncertainty in the V_{in}/V_{out} signal, and *ii)* the propagation of uncertainty from other parameters in the model [108, 154], which includes uncertainties related to measurement precision and data fitting sensitivities. In a TDTR measurement the absolute value of the signal phase is set by adjusting the reference phase of the lock-in amplifier until the out-of-phase voltage, V_{out}, is constant across zero delay time [101]. The uncertainty in the phase of the signal is taken as the RMS noise in the out-of-phase signal from delay times of -20 to +20 ps normalized by the jump in the in-phase signal at the zero crossing

$$\delta_\varphi = \frac{\delta_{V_{out}}}{V_{in}(0+) - V_{in}(0-)}, \tag{7.2}$$

where δ_{φ} is the uncertainty in the signal phase, $\delta_{V_{out}}$ is the noise in the out-of-phase signal, and V_{in} is the in-phase signal [154]. The uncertainty in a parameter p due to the propagation of uncertainty from another parameter y is calculated using sensitivities and is given by

$$\frac{\delta_p}{p} = \frac{S_y}{S_p}\frac{\delta_y}{y}. \tag{7.2}$$

The net uncertainty is taken as the square root of the sum of these two sources squared - that is the net uncertainty in a fit parameter p, denoted as δ_p, is given by

$$\left(\frac{\delta_p}{p}\right)^2 = \left((V_{io}/V_{out})\frac{\delta_{\varphi}}{S_p}\right)^2 + \sum_b \left(\frac{S_y}{S_p} \cdot \frac{\delta_y}{y}\right)^2, \tag{7.3}$$

where the first term represents the contribution from the uncertainty in the measurement signal and the second term represents the contribution propagated from uncertainty in other parameters, such as the thickness of the Al transducer [154]. The uncertainty in a parameter is calculated for each modulation frequency using sensitivities averaged over the entire delay time range of a scan, 300-7000 ps. When data at multiple modulation frequencies are simultaneously fit the frequency with the highest sensitivity to each parameter inherently has the largest influence in determining that parameter. Therefore, the total uncertainty for a parameter in a multi-frequency data set is taken as the sensitivity weighted average of the uncertainties at each modulation frequency.

At each delay time data is collected over a time span of 1-2 seconds. This provides an average and standard deviation in the signal at each time step. The standard deviation in the signal is useful for estimating the resolution of the measurement with respect to different parameters in the model. To estimate the resolution of the measurement the standard deviation in the V_{in}/V_{out} signal is compared to the difference between a theoretical V_{in}/V_{out} response, i.e. a solution, and experimental data via the expression

$$\Delta = \sum \left(V_{io,std.dev.} - \left| V_{io,exp.} - V_{io,theo.} \right| \right), \tag{7.4}$$

where $V_{io,std.dev.}$ is the standard deviation in the experimental signal (V_{in}/V_{out}), $V_{io,exp.}$ and $V_{io,theo.}$ are the experimental and theoretical signals respectively, and Δ is the difference summed across all delay times. If Δ is positive for two theoretical solutions then the solutions are considered to be indistinguishable, as they fall within the experimental error. The resolution of the measurement can be estimated by determining the range for a parameter over which Δ is positive.

Similarly, Equation 7.4 can also be used as an alternative method for calculating the uncertainty in a fitting parameter due to the uncertainty in the measurement signal, i.e. the resolution of the measurement. In this case the unknown parameter of interest, p, is held fixed while a solution is obtained by fitting for all other unknown parameters. The process is repeated using different initial values for p until the range that fits the data is established. In essence, if an initial value for p is chosen that doesn't fit the data, p cannot be that value. Throughout this process the range of allowable values for the other unknown fitting parameters should be restricted to physically plausible values [159].

7.4 Results

7.4.1 Glass-Al Interface Results

The best-fit solutions for the thermal conductivity and heat capacity of the glass layer and the interface resistance between the glass and Al layers ranged from 1.04-1.14 W/m-K, 1.4-1.6 MJ/m^3-K, and 0.02-0.04 mm^2-K/W (26-56 MW/m^2-K) respectively, within the anticipated range for glass [160]. A typical fit to experimental data is displayed in Figure 7.2, and the corresponding sensitivity plots for the best fit solution in Figure 7.3. The measurement is relatively insensitive to the glass-Al interface resistance, hence the wide range in best-fit solutions for this parameter, and is equally sensitive to thermal conductivity and heat capacity of the glass layer at both 1.2 and 3.6 MHz. This is because the measurement is actually sensitive to the glass

thermal diffusivity, $\alpha = k/C$, at both modulation frequencies. The standard deviation of the best-fit solutions to the glass thermal diffusivity was only ~1%, signifying that the thermal diffusivity of the glass is precisely identified.

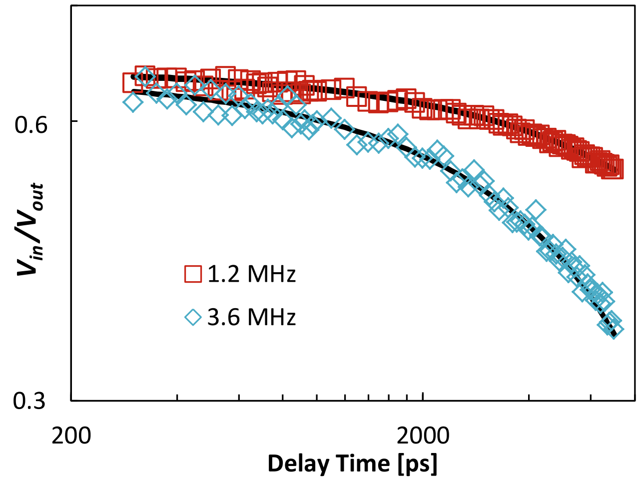

Figure 7.2: Representative TDTR data and best-fit solution for a Glass-Al sample.

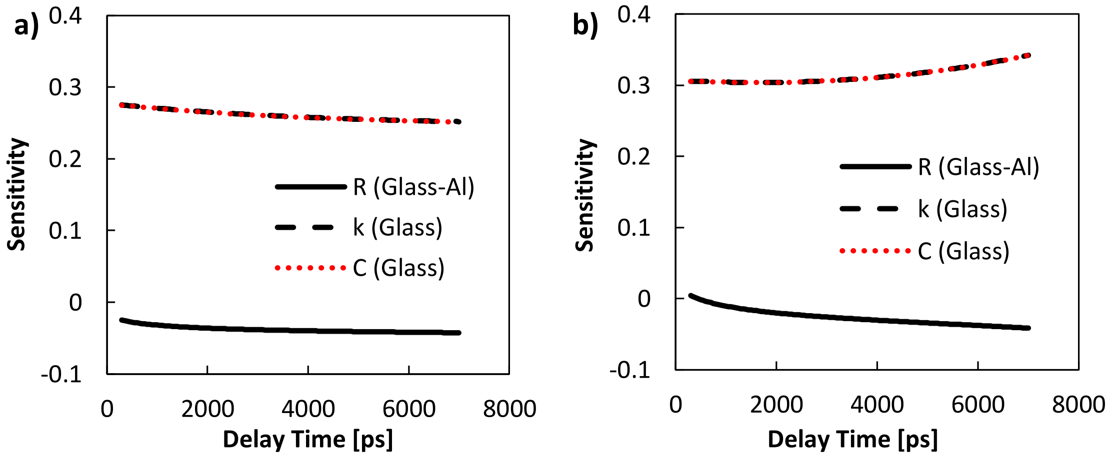

Figure 7.3: Sensitivity plots for Glass-Al at **(a)** 3.6 MHz, and **(b)** 1.2 MHz, showing equal sensitivity to thermal conductivity and heat capacity and relatively low sensitivity to the Glass-Al interface resistance.

The uncertainty calculated using Equation 7.3 ranged from 10-30% for the thermal conductivity and heat capacity and was frequently in excess of 100% for the glass-Al interface resistance. The uncertainty is dominated by the propagation of uncertainty from the Al layer

thickness. The contributions due to error in the V_{in}/V_{out} signal were usually less than 5% for the thermal conductivity and heat capacity. Since the same vendor and model of glass microscope slides were used throughout this research the thermal conductivity and heat capacity are expected to remain constant. Therefore, the average of the best-fit solutions for the thermal conductivity and heat capacity, 1.08 W/m-K and 1.49 MJ/m^3-K, were used and considered known in the subsequent measurement of CNT forest properties. Likewise, the average of best-fit solutions for the glass-Al interface resistance, 2.7x10^{-2} mm^2-K/W, was also used. Although the measurement is relatively insensitive to this parameter it likely varies between samples and across the surface of a single sample due to variations in the cleanliness of the glass surface prior to the Al deposition. To account for such variations an uncertainty of ± 43%, equivalent to the standard deviation of the best-fit solutions, was carried into in the subsequent analysis of CNT forest contacts.

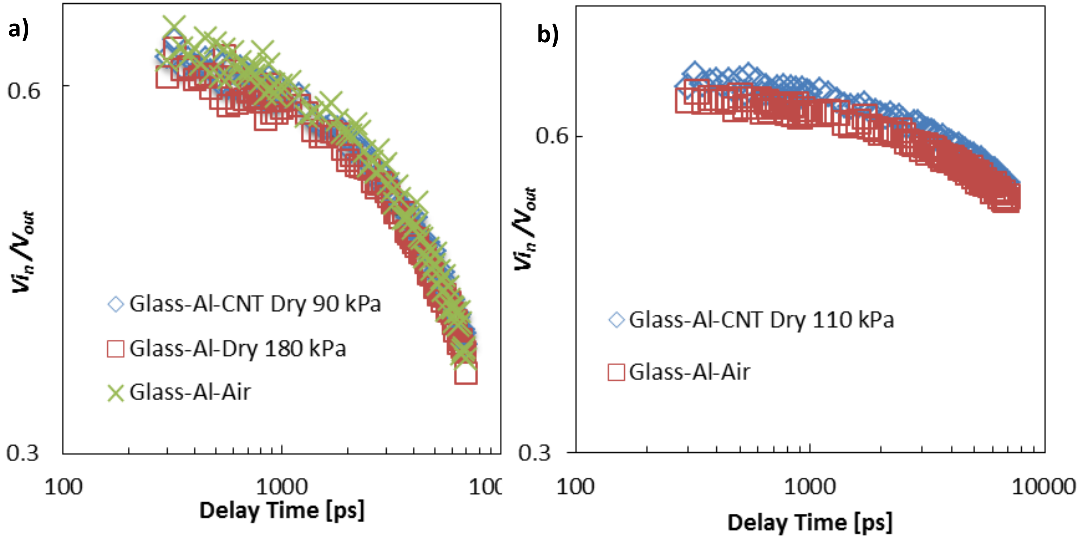

Figure 7.4: TDTR data at **(a)** 3.6 and **(b)** 1.2 MHz for Glass-Al and Glass-Al-Dry Contact CNTs are indistinguishable within the measurement error, indicating that the differences in interface resistance for these sample types cannot be resolved with TDTR at the modulation frequencies used.

7.4.2 Glass-Al-CNT Forest Interface Results

TDTR scans of CNT forests in dry contact with the Al coated glass at pressures ranging from 90 to 220 kPa were indistinguishable from scans on Al coated glass without CNTs, i.e. those with air as the backing, shown for a modulation frequency of 3.6 and 1.2 MHz in Figure 7.4. Due to the high interface resistance between the CNT forest tips and the Al (estimated ≥ 20 mm^2-K/W from Figure 5.4(a)) the majority of the heat deposited by the laser is directed into the glass slide. For this reason the measurement is insensitive to the thermal properties of dry contact CNT forests and thereby could not be measured with TDTR at the modulation frequencies (1.2, 3.6, and 6.3 MHz) and compressive pressures tested.

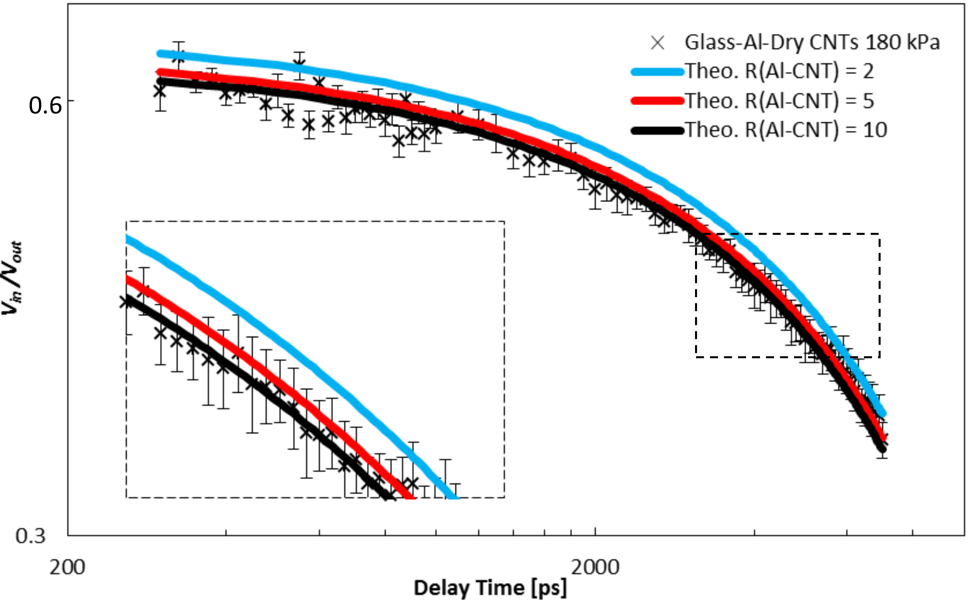

Figure 7.5: Actual Glass-Al-Dry Contact CNT data compared to theoretical Glass-Al-CNT data at 3.6 MHz with varying Al-CNT interface resistances illustrating the resolution of TDTR for characterizing dry contact CNT forests.

To gain insight into the maximum CNT tip interface resistance that can be resolved with TDTR theoretical V_{in}/V_{out} responses were generated for glass-Al-CNT forest samples with

assorted Al-CNT interface resistance values and compared to the experimental data for dry contact CNT forests (Figure 7.5). To calculate the theoretical responses the CNT forest properties were set to the initial guess parameters from Table 7.1 and the glass properties to the measured averages. Equation 7.4 was found to change sign for a contact resistance of ~3 mm^2-K/W indicating that resistances above this value cannot be resolved for the CNT forest properties and modulation frequencies considered here.

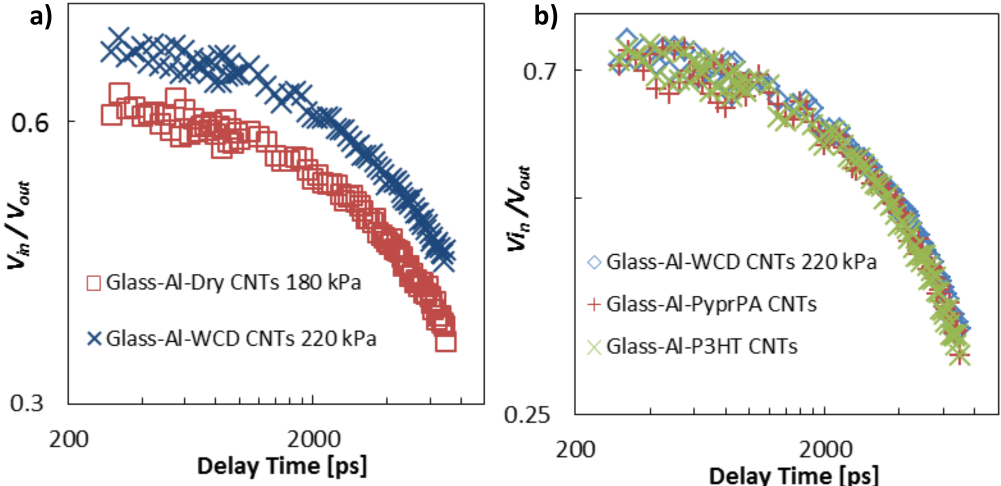

Figure 7.6: (a) Representative Dry and WCD CNT data at 3.6 MHz illustrating the shift in the signal associated with the WCD process. **(b)** TDTR data at 3.6 MHz for bonded CNT interfaces is indistinguishable, indicating that the differences in interface resistance for these sample types cannot be resolved with TDTR at the modulation frequencies used.

As a result of the WCD process the TDTR signal increased definitively at all of the modulation frequencies tested. An example of the change in the measurement signal at 3.6 MHz is shown in Figure 7.6(a). Bonding of CNT forests with a monolayer of the surface modifier PyprPA(with solvent) and the polymer P3HT had V_{in}/V_{out} responses comparable to the WCD CNT forest, shown at 3.6 MHz in Figure 7.6(b). A typical three frequency fit for P3HT bonded CNTs is shown in Figure 7.7. The best-fit solutions for the thermal diffusivity of bonded and WCD CNT forests ranged from 4.6x10^{-5} to 5.9x10^{-4} m^2/s, in agreement with previously reported

values [11, 161], and had uncertainties as calculated by Equation 7.3 typically on the order of 50%. The uncertainty primarily stemmed from the uncertainty in the Al layer thickness. The contribution due to the uncertainty in the V_{in}/V_{out} signal was below 3% for all samples.

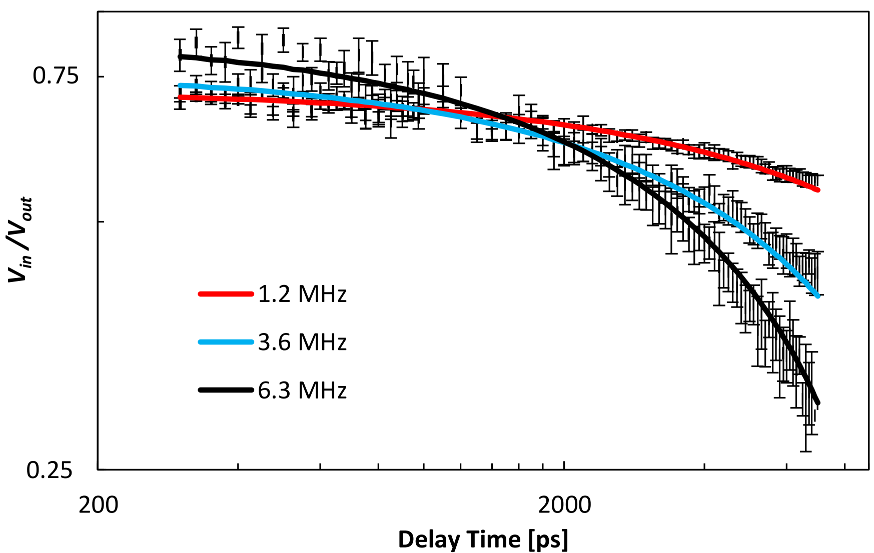

Figure 7.7: Representative three frequency data fit for P3HT bonded CNTs.

The uncertainty in the best-fit solutions for the thermal resistance of the bonded and WCD CNT forest interfaces ranged from ~130 to 560%, indicating that the thermal contact resistance could not be accurately resolved. In general, it was found that the measurement is unable to resolve the Al-CNT forest interface resistance below a certain threshold. To better understand this threshold the data was fit by adjusting the CNT forest thermal conductivity and heat capacity, while keeping the Al-CNT interface resistance fixed. The data was fit using progressively larger Al-CNT interface resistance values until the solution failed to fit the data within the standard deviation. The process is illustrated in Figure 7.8 for a PyprPA bonded CNT forest at 6.3 MHz. The bounds for the CNT forest thermal conductivity and heat capacity listed in Table 7.1 were used to restrict the solution space, although the parameters never approached these bounds. Equation 7.4 was used to establish a criterion for determining whether or not a solution

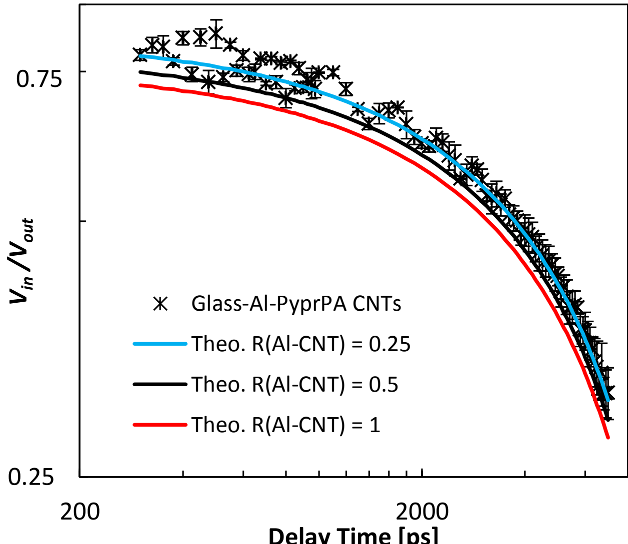

Figure 7.8: TDTR Data for Glass-Al-PyprPA bonded CNTs and theoretical fits with fixed Al-CNT interface resistances at 6.3 MHz used to determine the measurement resolution for characterizing bonded CNT forests.

"fit" the experimental data. The solution was considered to no longer fit the data when Δ became negative for one or more of the modulation frequencies. The Al-CNT forest interface resistance at which Δ changed signs represents a minimum resolution for characterizing the bonded CNT forests with TDTR. It also represents a range of possible values for the Al-CNT forest interface resistance, while only considering the standard deviation in the measurement signal as a source of uncertainty.

The upper bound for the Al-CNT interface resistances of bonded and WCD CNT forests calculated using the best-fit values and uncertainty calculated from Equation 7.3 are compared to the range estimated using Equation 7.4, in Table 7.2 below. The best-fit CNT forest thermal conductivity, heat capacity, and thermal diffusivity are also included in Table 7.2 for reference. PyprPA bonded samples could not be fit simultaneously fit to frequency pairings including 3.6 MHz. Since data at 1.2 and 6.3 MHz could be fit simultaneously those solutions are reported. The range of solutions for the Al-CNT forest interface resistance as calculated using Equation 7.4 was found to span from < 0.3 to < 0.6 mm^2-K/W for all samples. Similarly, the range of best-fit

Table 7.2: CNT forest thermal properties. See Appendix D for a more rigorous treatment of the uncertainty in these results using a preliminary Monte Carlo method and additional discussion.

Sample	Frequency [MHz]	Best-Fit (Eqn. 7.3)				(Eqn. 7.4)
		$R_{Al\text{-}CNT}$ [mm^2-K/W]	k_{CNT} [W/m-K]	C_{CNT} [kJ/m^3-K]	α_{CNT} [m^2/s]$\cdot 10^{-4}$	$R_{Al\text{-}CNT}$ [mm^2-K/W]
PyprPA	1.2, 6.3	< 0.5	9 ± 7	19 ± 6	4.9 ± 3.7	< 0.6
	1.2, 6.3	< 0.4	7 ± 3	6 ± 2	1.2 ± 0.7	< 0.3
	1.2, 6.3	< 0.3	9 ± 4	22 ± 6	4.2 ± 2.2	< 0.4
P3HT	1.2, 3.6, 6.3	< 1	4 ± 3	30 ± 2	1.3 ± 1.1	< 0.6
	1.2, 3.6, 6.3	< 0.2	7 ± 3	23 ± 8	3.3 ± 1.8	< 0.5
	1.2, 3.6, 6.3	< 0.4	3 ± 2	50 ± 30	0.6 ± 0.5	< 0.3
WCD	1.2, 3.6, 6.3	< 0.5	3 ± 2	60 ± 35	0.5 ± 0.4	< 0.3

solutions for the Al-CNT forest interface resistance calculated using Equation 7.3 ranged from < 0.2 to < 1 mm^2-K/W. The uncertainty in these values had contributions from the uncertainty in the Al film thickness and the uncertainty in the measurement signal. Equation 7.3 and Equation 7.4 lead to comparable ranges for the Al-CNT forest interface resistance. Equation 7.3 seems to represent a more lenient consideration of the uncertainty in the measurement signal, whereas Equation 7.4 is known to be conservative estimate since the criterion, a phase shift difference equal to one standard deviation of the signal, can be resolved. The magnitude of these findings for the Al-CNT interface resistance are comparable to those of a recent study by Kaur et al. [107] where the identical sample structure was used to characterize CNT forests bonded with two different surface modifiers. The method used by Kaur et al. to calculate the uncertainty in the measurement was not disclosed, however, the uncertainty in their reported values is likely under-predicted based on the findings of this study.

Overall, none of processing methods definitively reduced the contact resistance at the CNT tip interface more extensively than the others. All of the methods produced CNT forest contact resistances < 0.4 mm^2-K/W for at least one measurement location. This suggests that thermal transport at individual CNT contacts could be similar for all cases, although without exact knowledge of the contact resistance and contact area it remains unclear. If a contact

resistance of 0.02 mm^2-K/W [20, 41] is assumed for an individual CNT vdW contact, a CNT forest free tip contact resistance of 0.4 mm^2-K/W would correspond to 5% contact area. This value is significantly higher than theoretical predictions for the maximum contact area at CNT forest interfaces (~1%) [44]. However, it is physically conceivable; especially for the polymer bonded CNT contacts where the polymer coating is expected to significantly extend the contact area at individual CNT tips (Chapter 6). Moreover, contact areas less than 5% would be feasible for bonded CNT contacts, such as those bonded with PyprPA or other surface modifiers, where the stronger bonding is expected to decrease the resistance of individual CNT contacts significantly [78].

Considering the lowest total resistances for the bonded and WCD CNT TIMs measured in this research ranged 3-5 mm^2-K/W, the CNT free tip interface after processing contributes < 13% to the total resistance (assuming a free tip resistance of 0.4 mm^2-K/W). This contribution will only be further diminished for taller CNT forests, as the layer resistance and potentially the growth substrate resistance increase [106]. Additionally, for all of the bonded and WCD interfaces the Al-CNT contact resistance never exceeded 1 mm^2-W, indicating the efficacy of the methods across the entire area of interface, i.e. across device-sized areas.

7.5 Limitations of the Bi-Directional Sample Configuration

The upper limit on the Al-CNT forest contact resistance that can be resolved with the bi-directional sample configuration in TDTR is dictated by the relative flow of heat into the materials on either side of the interface, and by the penetration depth of the thermal waves (Equation 3.1). For the dry contact glass-Al-CNT forest interfaces in this research the high Al-CNT contact resistance causes the majority of the heat to preferentially flow along the lower resistance pathway, i.e. into the glass layer. As a result, the V_{in}/V_{out} response of glass-Al-CNT forest dry contact interfaces was observed to be equivalent to that of a glass-Al-air sample. The upper limit on Al-CNT forest that can be resolved with TDTR could be improved by decreasing the thermal conductivity of the backing to direct more of the heat into the CNT forest and by

decreasing the modulation frequency to increase the thermal penetration depth. In the ideal sample the glass backing ($k \approx 1$) would be replaced with air ($k \approx 0.02$). This is representative of the conventional TDTR sample configuration, where the Al transducer is deposited directly on the sample of interest.

For the bonded glass-Al-CNT forest samples, where the Al-CNT interface resistances are significantly lower (< 1 mm^2-K/W) the resolution of the measurement is plagued by low sensitivity to the CNT layer properties and interface resistance. In this scenario the sensitivity to the properties of the CNT forest is determined by the relative thermal effusivities of the glass and CNT forest. The thermal effusivity, commonly referred to as thermal inertia, is defined as

$$e = (kC)^{1/2}. \tag{7.5}$$

This dependence is illustrated in a plot showing the sensitivity of the measurement at 3.6 MHz and a delay time of 1000 ps to generic CNT forest properties for a variety of backing substrate diffusivities in Figure 7.9. Most of these materials are not feasible as actual baking substrates for TDTR because they are not transparent to the pump and probe beam wavelengths (400 and 800 nm respectively), or do not support the high vacuum deposition of the transducer. Nonetheless, they illustrate the full range of possibility for a bi-directional sample configuration. As shown in Figure 7.9 the thermal effusivity of the CNT forest is comparatively low leading to low sensitivities for backing substrates of common solids. Air again represents the best-choice as a backing for maximizing the resolution of the measurement for CNT forests. However, doing so does not guarantee that CNT forest contacts can be resolved. For CNT forests with the transducer evaporated directly onto the free tips Gao et al. [106] was yet unable to resolve the transducer-CNT forest interface below 0.5 mm^2-K/W using both nanosecond thermoreflectance and FDTR.

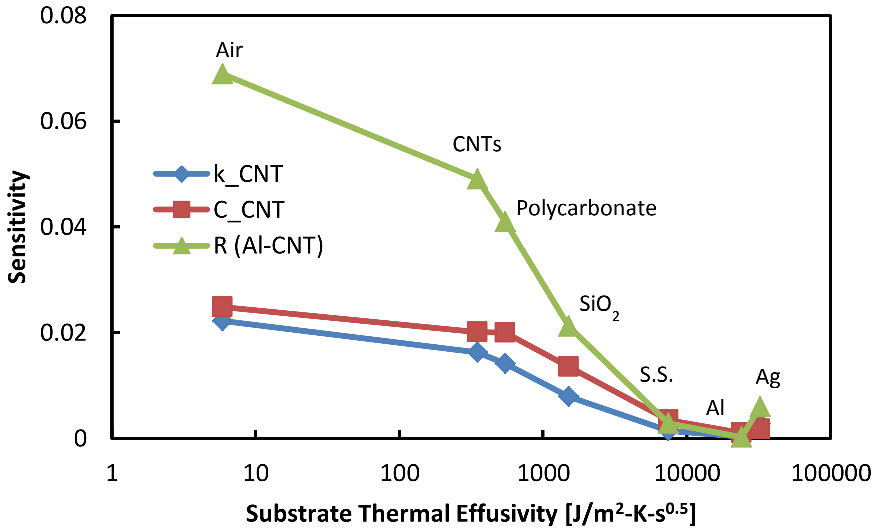

Figure 7.9: TDTR measurement sensitivity to CNT properties as a function of the effusivity of the backing substrate.

7.6 Summary and Recommendations

7.6.1 Summary

Time-domain thermoreflectance was used to resolve the thermal resistance of the CNT forest free tip interface and to evaluate the approaches developed in this research. PyprPA and polymer (P3HT) bonded and WCD interfaces were all measured to have thermal contact resistances < 1 mm^2-K/W. As such, for all the approaches developed in this research the CNT free tip interface no longer dominates the total resistance of the CNT TIM. The resolution of the measurement for examining dry and bonded CNT forest contacts is limited by the relatively high thermal conductivity and thermal effusivity of the transparent glass backing substrate.

7.6.2 Recommendations

To improve the capabilities of the measurement for studying both dry and bonded CNT forest contacts is it recommended that the backing substrate be replaced with air at the location of the measurement. Since studying bonded or pressed CNT forest contacts requires that the transducer be deposited on a mechanically rigid substrate the backing substrate cannot be altogether

eliminated. Instead it is recommended that a process is developed to fabricate small holes, ~100 μm in dimension (large enough for the pump and probe beams to pass through), in the backing substrate without damaging the Al transducer film. Furthermore, a comprehensive Monte Carlo treatment of the uncertainty (Appendix D) should be carried out to better understand the limitations of the measurement.

CHAPTER 8

SUMMARY AND RECOMMENDATIONS

Several methods for integrating CNT forests as TIMs in electronics packaging with low thermal contact resistance have been developed. These approaches require low temperatures and pressures compared to existing methods that rely on metal as a bonding material, and generally utilize low-cost materials and processes. As such, these approaches represent a significant step towards both practical and effective CNT forest TIMs that are amenable to adoption at commercial scales.

8.1 Summary and Major Findings

This research specifically concentrated on the problem of contact resistance at the interfaces between the free tips of CNT forests and surfaces in electronics packaging. The contact resistances for dry CNT forests at these interfaces are known to be prohibitively high, and were estimated through measurement of the total resistance with photoacoustic to be 10-20 mm^2-K/W or greater for the CNT forests examined in this research. Low contact area and weak bonding were identified as the foremost factors contributing to the contact resistance and targeted as mechanisms for reducing it. Three separate strategies were developed with low-cost and scaling in mind; *i)* liquid softening, *ii)* surface modifiers, and *iii)* nanoscale polymer coatings. For CNT forests around 10 μm in height all of the strategies developed were measured with photoacoustic to reduce the total resistance by 70-90% to ~5 mm^2-K/W. The contact resistance at the CNT tip interface was resolved from the total resistance using time-domain thermoreflectance. All three of the strategies produced CNT forest contact resistances < 1 mm^2-K/W.

Consequently, the total thermal resistance of CNT forest TIMs is no longer dominated by the contact resistance at the free tips. To illustrate this point the ratio of the free tip contact resistance to the total resistance is plotted as a function of CNT forest height for a range of CNT forest thermal conductivities in Figure 8.1. The free tip interface resistance is set to 0.5 mm^2-

K/W, based on the findings of this research and other studies discussed in section 8.2. The other side of the CNT forest is modeled as a growth-substrate interface and the interface resistance is set to 1 mm^2-K/W [11]. As shown in Figure 8.1 the contribution of the CNT tip interface is at most 1/3 of the total resistance for the prescribed conditions. For a 10 μm tall CNT forest, the lower end of bond-line-thickness anticipated for applications, with a thermal conductivity of 10 W/m-K the contact resistance at the free tip interface only contributes 20% of the total resistance. A number of recent studies have reported CNT forest thermal conductivities below 10 W/m-K [106, 123, 162] and growth substrate interface resistances increasing with CNT forest height to values as high as 80 mm^2-K/W [106]. The contribution of the free tip contact resistance would be even further diminished for CNT forests with these characteristics.

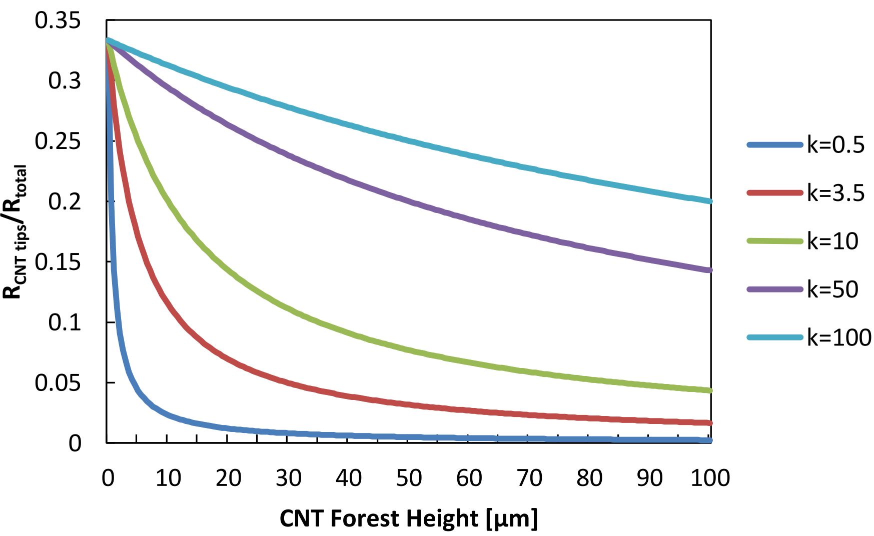

Figure 8.1: Ratio of the CNT free tip contact resistance to the total resistance after processing with the methods developed in this research illustrating the diminished role of the contact resistance. The CNT free tip resistance is set to 0.5 mm^2-K/W and the growth substrate resistance to 1 mm^2-K/W.

In addition to effectively mitigating the contact resistance at the CNT forest free tip interface a number of other technical and scientific developments resulted from this research. A

brief summary of each of the strategies is given in the sections below, alongside a list of the most significant findings.

8.1.1 Chapter 4: Liquid Softening

A strikingly simple and straight-forward approach for enhancing the contact area at the CNT forest tip interface was demonstrated. The approach relies on infiltrating the CNT forest with a liquid before compressing it against a surface and allowing it to dry. Infiltrating the CNT forest with the liquid attenuates the van der Waals interactions at inter-CNT contact points within the forest and thereby reduces its mechanical stiffness. When compressed against a surface in the wet state the CNT forest more readily deforms leading to increased contact between the CNT forest and the surface. The contact area was found to increase by as much as ~80%, corresponding to an equivalent reduction in thermal contact resistance and enhancements in adhesion to glass surfaces. Specific novel findings from this work include:

- Contact area explicitly identified as a major contributor to the thermal resistance of CNT forest contacts
- Demonstration that through wet compression the contact area can be enhanced to dramatically reduce contact resistance, by as much as ~80%
- Contact area saturation with CNT forests at unprecedentedly low compressive pressure, 35 kPa, possibly lower
- Record approaching dry CNT forest shear adhesion to glass at an order of magnitude lower compressive preload: 10-24 N/cm^2 for wet compression at 35-105 kPa
- Evidence was not found to support the hypothesis that capillary induced deformations during drying of a CNT forest while compressed in an interface significantly alter the contact area or thermal resistance

8.1.2 Chapter 5: Pyrenylpropyl Phosphonic Acid Surface Modifier

A pyreneypropyl phosphonic acid (PyprPA) surface modifier was created for coupling CNTs to metal oxide surfaces in a simple and scalable manner to reduce the thermal contact resistance. When used to couple vertical CNT forests to oxidized Cu surfaces the PyprPA modifier reduced the thermal contact resistance by approximately 9-fold over CNT forests in non-bonded dry contact. As a thermal interface material PyprPA coupled CNT forests had a total thermal resistance of 4.6 ± 0.5 mm^2-K/W. Electrical characterization of PyprPA coupled and dry contact CNT interfaces indicate that the modifier may reduce the electrical contact resistance by a similar magnitude. The results of this work highlight the important role of bond strength in thermal transport at CNT contacts. Furthermore, it demonstrates that surface modifiers, such as the one synthesized here, could be used with relatively simple and repeatable processing steps to significantly reduce contact resistances in CNT-based materials for thermal and electrical transport.

Specific novel findings from this work include:

- Bond strength explicitly identified as a major contributor to the thermal resistance of CNT forest contacts
- Identification of surface modifiers as a viable strategy for improving bond strength and reducing the thermal resistance of CNT forests contacts uniformly over device-sized areas, by as much $> 80\%$ with PyprPA
- Demonstration of surface modifiers as a method for mechanically attaching CNT forests to surfaces. A normal adhesion of 340 ± 50 kPa was achieved with PyprPA
- Identification of surface modifiers as an instrument to reduce electrical resistance of CNT forest contacts. A $> 80\%$ reduction was demonstrated with PyprPA
- Identification of PyprPA as a potential surface modifier for forming ohmic CNT contacts
- Identification of additional surface modification and bonding strategies

8.1.3 Chapter 6: Polymer Spray Coating and Bonding

A spray coating process was developed for depositing nanoscale coatings of polymer onto CNT forests, as a bonding agent. The coatings mitigate the thermal resistance by enhancing the area contact area locally around individual CNT tips. Two polymers were tried; polystyrene and poly(3-hexylthiophene), and no dependence on polymer type was observed. Total thermal resistances as low as 4.9 ± 0.3 mm^2-K/W were achieved.

Significant novel findings from this work include:

- Spray coating demonstrated as a method for applying nanoscale coatings of soluble materials to the surfaces of CNT forests, while preserving the internal morphology/microstructure of the forest
- Polymers, generally thermal insulators, were demonstrated as effective materials for reducing the thermal resistance of CNT forest contacts when applied as nanoscale coatings
- Spray coating and bonding of CNT forests with polymers at room temperature and low pressure (140 kPa) reduced the thermal resistance of the CNT forest tip interface by as much as ~75%, although the process had control/repeatability issues
- Locally increasing the contact area at individual CNT tips by the addition of coatings identified as potential method for reducing thermal resistance.
- Polymers coatings demonstrated as a method for mechanically attaching CNT forests to surfaces. An average shear attachment strength of 29 N/cm^2 was achieved.

8.2 Comparison with Existing Bonding Approaches

The thermal resistances of CNT TIMs fabricated via these approaches and the relevant processing parameters are compared to existing methods in Table 8.1. The processes developed in this research focused on scalable and effective methods for reducing the contact resistance at the CNT tips, therefore, a comparison at the scale of total resistance like most of the entries in Table 8.1, is

Table 8.1 Thermal resistances of bonded CNT forest TIMs compared to conventional TIMs.

Interface	CNT Forest Height [μm]	Measurement Pressure [kPa]	Thermal Resistance [mm^2-K/W]	Implementation Process
Bonded CNT Forests:			**Bonded/Dry Contact:**	
Si-MWCNT-In-SiO_2[32]	10	0	$R_{CNT\ tips} \approx R_{total}$: ~1/11	Metal Evaporation, Bonding (Pressure NA[a], 180 °C)
Si-MWCNT-Au-Ag[34]	30	0	R_{total}: 4.5/NA[a]	Metal Evaporation, Bonding (Pressure NA[a], 220 °C)
Si-Au-Patterned MWCNT-Au-Si[35]	~60	63	R_{total}: 62/336[b]	Metal Evaporation, Bonding (63 kPa, 150 °C)
Cu-MWCNT-Si[33]	NA	0	R_{total}: 10/50	Spin Coating, Microwave Bonding (6.425 GHz, 750 kPa, 160 °C)
Si-MWCNT-Pd-Ag[163]	20	34	R_{total}: 11/22	Drop Casting, Bonding (273 kPa, 250°C)
Si-MWCNT-Al/Ni-SiO_2[162]	500	50-500	$R_{CNT\ tips}$: 27-41/~1000	Metal Evaporation, Bonding (250 kPa)
Si-MWCNT-In-SiO_2[162]	500	100-600	$R_{CNT\ tips}$: 30-47/~1000	Metal Evaporation, Bonding (250 kPa, 180 °C)
Si-MWCNT-APS-Al-SiO_2[107]	70-100	0	$R_{CNT\ tips}$: 0.6/3.5	O_2 Plasma, Solution Modification, Bonding (120 °C, 50 kPa)
Si-MWCNT-Cyst-Au-SiO_2[107]	70-100	0	$R_{CNT\ tips}$: 0.8/3.5	O_2 Plasma, Solution Modification, Bonding (120 °C, 50 kPa)
This Research:				
Si-MWCNT-Ag	5	7	R_{total}:3/11 $R_{CNT\ tips}$: < 0.5	Wetting, Compression (35 kPa, RT[c])
Si-MWCNT-PyprPA-Cu-Ag	15	7	R_{total}:5/40 $R_{CNT\ tips}$: < 0.6	Solution Modification, Bonding (300 kPa, RT[c])
Si-MWCNT-Polymer-Ag	10-115	7	R_{total}:5-44/20-80 $R_{CNT\ tips}$: < 1	Spray Coating, Bonding (140 kPa, RT[c])
Conventional Materials [17]:				
Greases			20-100	
Gels			40-80	
Pads			100-300	
Phase Change			30-70	
Solder			5	

[a] NA: Data not available [b] The reported area specific thermal resistances were recalculated using the total area of the interface (4 mm^2) instead of only the patterned CNT area (1.13 mm^2) to reflect the effective thermal resistance, as would be experienced by a real device. [c] RT: room temperature

not a true evaluation of methods developed in this research. However, due to the challenging nature of resolving the CNT forest tip interface resistance this is usually the only comparison that can be made.

There are a few instances where direct comparisons of the contact resistance at the CNT can be used to evaluate the merits of the approaches developed in this research. In 2007 Tong et al. [32] using 1 μm of In to bond CNTs to glass was able to reduce the contact resistance from ~11 to < 1 mm^2-K/W, a greater than 90% reduction. Although, the contact resistance achieved is similar those obtained in this research, Tong noted that the bonding was inconsistent across the surface of the sample resulting in areas of increased contact resistance. Furthermore, this approach utilized bonding at 180 °C, which is not feasible for many devices and packaging schemes. In a similar approach Barako et al. [162] used 25 μm of In to bond metal coated CNTs to metal coated target substrates. The bonding process reduced the contact resistance at the CNT tips from ~1000 mm^2-K/W to between 30 and 47 mm^2-K/W, a > 95% reduction. Yet, the bonded contact resistances are at least an order of magnitude larger than those achieved in this research. Moreover, the approach utilized metal evaporation on both the CNT forest and target substrate to facilitate wetting of the indium and high temperature and pressure bonding (180 °C and 250 kPa). In the same study Barako et al. [162] also examined bonding using a commercially-available reactive metal film (*NanoFoil®, Indium Corp*). Given a small activation energy in the form of an electrical current, optical pulse, or heat pulse the reactive film undergoes an exothermic reaction to melt and join the interface. This removes the necessity to apply heat from an external source, however, 250 kPa of pressure and metal evaporation on the CNT forest tips and target substrate were still used to facilitate bonding. The contact resistance of CNT forests tips bonded using the reactive film were also 27-41 mm^2-K/W, at least an order of magnitude higher than the contact resistances achieved in this research.

Kaur et al. [107] used the commercially-available surface modifiers aminopropyl triethoxysilane and cysteamine to join CNT forests to Al and Au surfaces respectively. The

modifiers reduced the contact resistance from 3.5 ± 0.5 to 0.6 ± 0.2 and 0.8 ± 0.2 mm^2-K/W for the modified Al and Au interfaces respectively. As such, both modification strategies produce bonded contact resistances similar to those achieved by this research. The modification and bonding procedures employed by these strategies were nearly identical to that developed for the PyprPA modifier (Chapter 5) with the exceptions that the CNT forests were treated with oxygen plasma, and that bonding was conducted at 120 °C. Aside from these processing differences the scalability and effectiveness of the strategies are comparable that of the PyprPA. The polymer spray coating and bonding (Chapter 6) and wet compression (WCD) process (Chapter 4) represent potentially more scalable processes that achieve similar contact resistances.

8.3 Recommendations

There remains a significant and growing need for mechanically compliant, i.e. reliable, TIMs with low thermal resistance (< 10 mm^2-K/W) that are chemically stable at elevated temperatures (> 130 °C) (see Chapter 1) [5, 9, 17]. Utilizing the methods developed in this research, and elsewhere, for mitigating the contact resistance at the free tip interface, even CNT forests with relatively low thermal conductivity (< 10 W/m-K) could potentially meet these requirements and fill a major technological gap. Future research should therefore continue to focus on improving CNT forests with regard to these aspects. Perhaps foremost, the reliability of CNT TIMs should be investigated. Several recent studies have reported on the favorable low in-plane modulus of CNT forests [164], however, there have yet to be any studies published that critically examine the reliability of bonded CNT forest TIMs. Future research should also continue efforts to reduce the thermal resistance of CNT TIMs. Although, the emphasis should now be shifted from free tip interface resistance to the thermal conductivity of the CNT forest [106, 123, 162], and possibly the growth substrate resistance [106]. Pursuing CNT growth strategies for higher number density of CNTs in the array [165] could help address this issue since the most arrays currently only have about 1 to 10% CNT material [18]. The mechanisms that affect the chemical stability of CNTs

are well understood and the majority of CNTs are stable at sufficiently high temperatures. Accordingly, this aspect should not be a point of emphasis.

The thermal properties of CNT forests and their application as TIMs have been an active topic of academic research for nearly a decade. Although our understanding of these materials has advanced dramatically during that time there remains more to be learned. Unfortunately, basic science funding and the general excitement of the scientific community toward these materials has and will continue to fade. If research on CNT forest TIMs is to continue and a commercially viable CNT TIM is to be realized it will be essential that researchers studying these materials take their knowledge and research programs to industrial partners or transition the technology from academia to industry themselves.

APPENDIX A

MODIFICATION OF CNTS AND COPPER OXIDE WITH PYRENYLPROPYL PHOSPHONIC ACID

This research was carried out by collaborators Dr. O'Neil L. Smith and Professor Seth R. Marder of the Georgia Tech School of Chemical and Biomolecular Engineering in support of the research reported in Chapter 5 of this dissertation.

A.1 Verification of CNT Modification with PyprPA

CNTs (10 mg) were added to 50 mL of DI water and sonicated for 4 hours before a PyprPA solution (1.5 mM, in methanol) was added and the mixture stirred overnight. Several centrifugation/wash cycles in DI water was undertaken to remove the excess PyprPA, after which the modified tubes were dried in a vacuum oven at 80 °C. Prior to annealing in the oven, the degree of removal of the excess acid was assessed by monitoring the UV-vis spectra of the PyprPA in the DI water supernatant (Figure A.1(a)). It was observed that after the nine washes, very little acid was removed in subsequent cycles which suggest that the majority of the remaining molecules were directly associated with the CNT. In order to approximate the amount of the acid that was bound to the CNTs, calibration curves for both the CNTs and the pyrene modifier were generated using the absorptions at 254 and 344 nm, respectively (Figure A.2) in 1% sodium dodecyl sulfate. Based on the difference spectrum between the UV-vis of the modified CNTs and the pristine nanotube (Figure A.1(b)) the amount of PyprPA per microgram of CNT was found to be 1.2×10^{-4} mol/µg. A CNT spectrum was chosen such that the absorption within the 600 – 800 nm region closely approximates that of the modified CNT as have been demonstrated elsewhere [166]. Raman spectroscopy was performed on the CNT-PyprPA hybrid. The Raman spectra (Figure A.3) of the pristine and modified CNTs showed the characteristic

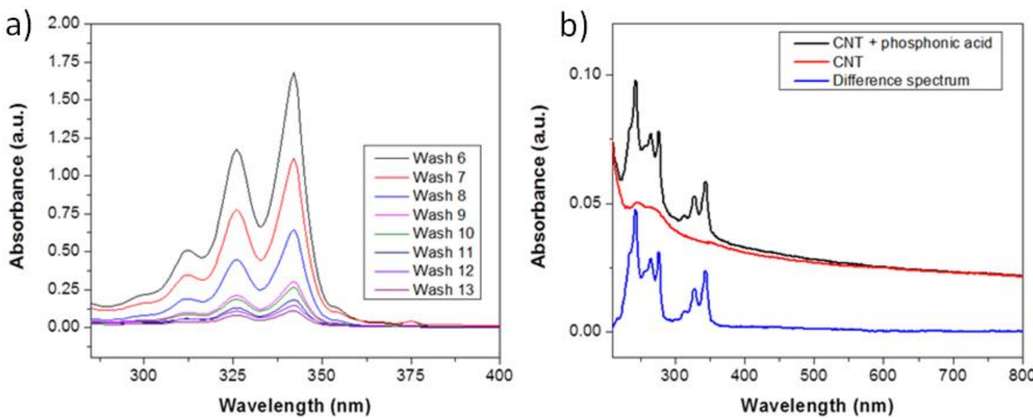

Figure A.1: Modification of CNTs with pyrenylpropyl phosphonic acid. (**a**) Monitoring the supernatant after modification to assess the removal of excess modifier from the CNTs. (**b**) UV-Vis spectra used to approximate the amount of the modifier per micro gram of CNT.

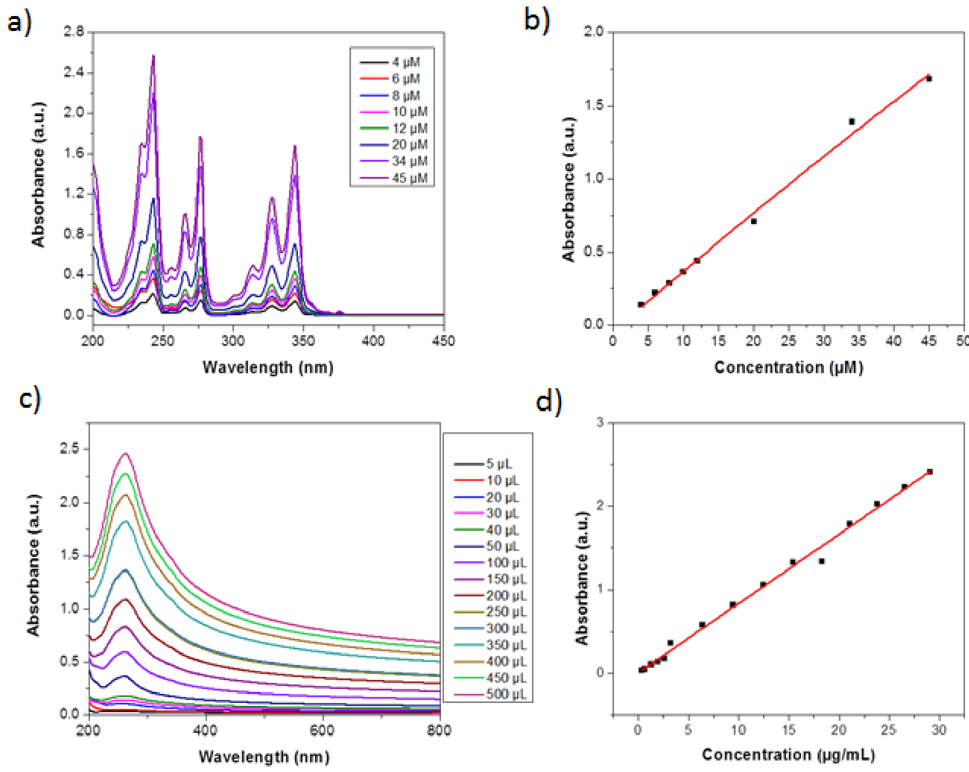

Figure A.2: Calibration curves. **(a)** UV-vis of various concentration of pyrene-based phosphonic acid. **(b)** calibration curve, of pyrene moiety. **(c)** UV-vis of various concentration of CNTs. **(d)** calibration curve, of CNTs.

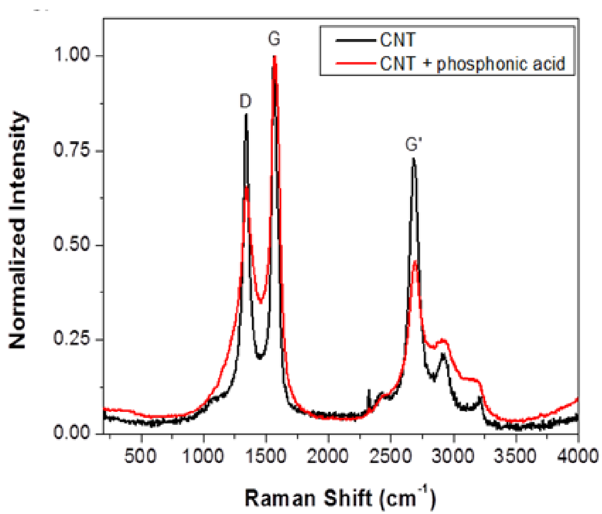

Figure A.3: Raman spectra of modified and unmodified CNT.

bands [93] but no clear shift in the band positions between the modified and unmodified CNTs was observed as reported elsewhere [131, 132].

A.2 Verification of Copper Oxide Film Modification with PyprPA

Prior to modification, the copper substrates were cleaned by sonicating them consecutively in dilute triton X, DI water and ethanol for 10 min each. The oxide films were then dried under a stream of nitrogen and oxygen plasma etched for 2 min (Plasma Etch-50) before they were immersed in a 1.5 mM solution of the PyprPA solution (ethanol:chloroform; 1:1) for 24 hours. After modification, the films were sonicated for 30 min in the aforementioned solvent system to remove any physisorbed molecules before they were examined by XPS. All XPS measurements were carried out on a *Kratos Axis Ultra* spectrometer using a monochromatic Al(Kα) source. All the measurements were acquired at normal take-off angle of 0° relative to the surface normal at pass energies of 160 eV and 20 eV for surveys and high resolution data, respectively. The high resolution spectra of Cu 2p region is shown in Figure A.4(a) for both the modified and unmodified copper oxide films; peak assignments were consistent with that shown by Barr [167]. The surface coverage was approximated by evaluating the degree attenuation

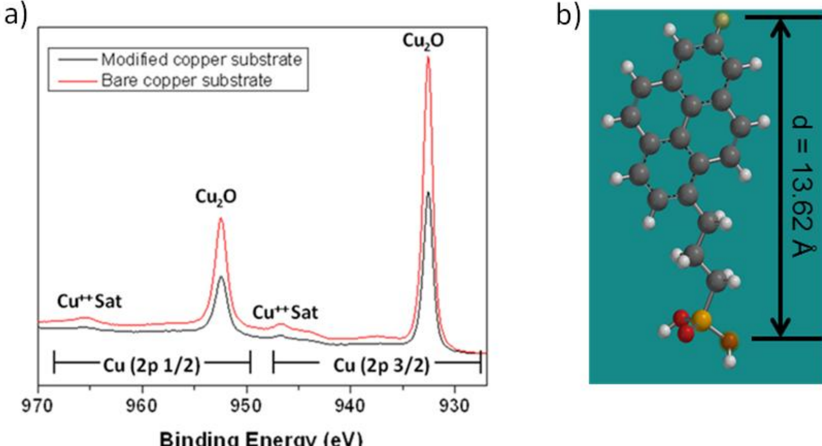

Figure A.4: Assessment of coverage. **(a)** High resolution spectra of the Cu 2p region which shows the attenuation of the signal upon modification with the phosphonic acid. (**b**) optimized geometry (Hartree-Fock, basis set 6-31 G) in which the molecular length is estimated to be 13.62 Å.

of the Cu 2p photoelectrons by the organic overlayer. The attenuation of the Cu 2p signal (A_{Cu}) is represented by

$$A_{Cu} = S_{Cu}^{ML}/S_{Cu} = \exp[-d/\lambda_{ML} \sin \theta], \qquad (A.1)$$

where S_{Cu}^{ML} is the signal from the modified surface, S_{Cu} is the signal from the bare Cu substrate, d is the thickness of the monolayer, λ_{ML} is the attenuation length of the copper photoelectrons in the organic layer and θ is the take-off angle between the sample and the detector. The attenuation length was approximated from the inelastic mean free path (IMFP) using the Cumpson method [168]. In this approach the IMFP is determined based on the connectivity and electronic environment of the molecule using a quantitative structure-property relationship model. Subsequently, elastic scattering is assumed to be negligible therefore IMFP ~ λ_{ML}. Using this approach, the thickness of the monolayer was found to be 10.35 ± 0.34 Å. Theoretical calculations on the Hartree-Fock optimized

molecular structure (basis set 6-31 G) suggest that for a monolayer coverage the maximum thickness should be about 13.62 Å (Figure A.4(b)).

APPENDIX B

EXPLORATION OF ADDITIONAL PHOSPHONIC ACID SURFACE MODIFIERS

Here we explore the bridging of oxide-coated CNT forests with metal and metal oxide surfaces using phosphonic acid based surface modifiers. These modifiers form covalent bonds to both sides of the interface. The intent is to address the technical need for a thermally conductive, mechanically compliant, and electrically insulating TIM architecture. This research was conducted in collaboration with Dr. Virendra Singh and Ms. Cristal J. Vasquez of the George W. Woodruff School of Mechanical Engineering at Georgia Tech and Dr. Stephen Barlow, Dr. Tim Parker, and Professor Seth R. Marder of the Georgia Tech School of Chemical and Biomolecular Engineering. It was partially supported by the Georgia Tech X-Materials Program.

B.1 Methods

B.1.1 Sample Configuration

To examine different linker molecules in a configuration representative of an application and to simultaneously facilitate measurements of thermal resistance, oxide coated CNT forests were contacted by 25 μm Ag foils coated with 30 nm of Al, as is shown in Figure B.1. In this configuration the Al_2O_3 coated CNT free tips and the native oxide on aluminum surface can be modified and bonded using phosphonic acid surface modifiers.

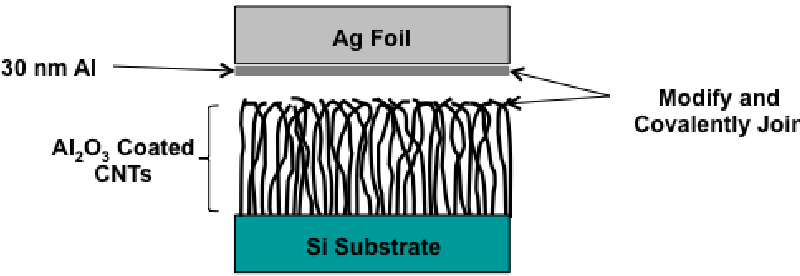

Figure B.1: Sample configuration for evaluating surface modifiers and processing strategies.

B.1.2 Oxide Coated Carbon Nanotube Forest Synthesis

Nominally vertically aligned multi-wall CNT forests were grown on crystalline Si substrates 1x1 cm in area in size using the synthesis procedure described in section 3.1. The growth time was varied from 1-10 min to achieve forest heights ranging from 10-50 μm, as measured by SEM. A *Cambridge NanoTech* ALD system was used for plasma enhanced atomic layer deposition (PALD), where Al_2O_3 coatings were deposited on individual CNTs in forests. This process was facilitated by an O_2 plasma pretreatment to functionalize the surfaces of the CNTs to nucleate oxide growth [156]. The precursors for Al_2O_3 are trimethylaluminium (TMA) for Al and H_2O for O_2. Al_2O_3 is deposited thermally at 250 °C with a deposition rate of 1.0 Å – 1.1 Å per cycle and 30 s exposure times. For this work 0.5-10 nm thick coatings were used. An image of a CNT forest coated with 8 nm of Al_2O_3 is shown Figure B.2.

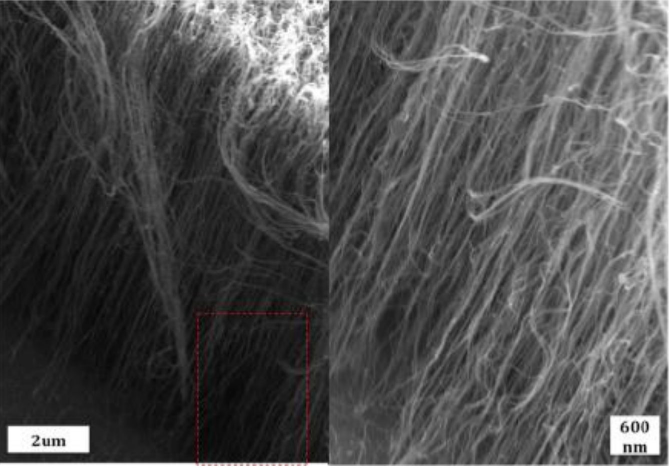

Figure B.2: SEM image of a ~10 μm tall CNTs coated with 8 nm of Al_2O_3. The right image is a magnification of the red box outlined in the left image.

B.1.3 Modification and Bonding Strategies

Two different approaches were considered for covalently linking oxide coated CNTs to metal-oxide surfaces. The first, *Strategy 1*, centered on using linear carbon molecules terminated at each end with a phosphonic acid functionality, which we refer to as a bisphosphonic acid (BisPA).

From the plethora of possible BisPA molecules a (1,4-phenylenebis(methylene))diphosphonic acid (Benzene-BisPA) and a 1,8-Octanediphosphonic acid (Octane-BisPA) were selected for testing and are illustrated in Figure B.3. The selection of these two molecules was motivated by the differences in the length of their carbon backbones. The second strategy, *Strategy 2*, involved using two different phosphonic acid terminated molecules to separately modify the oxide coated CNTs and the metal oxide surface, and then join them via a reaction between the opposing terminations of the two modifiers (Figure B.3(c)). Specifically, an acrylate-phosphonic acid (Acrylate-PA), CH_2=CH-C(O)O$(CH_2)_{11}PO_3H_2$, and 3-aminopropylphosphonic acid (Amino-PA), $NH_2(CH_2)_3PO_3H_2$, were used to separately modify the oxide coated metal and CNTs, respectively. The two modified surfaces are then brought into contact and joined through Michael-addition between terminal amine and acrylate functionalities [141].

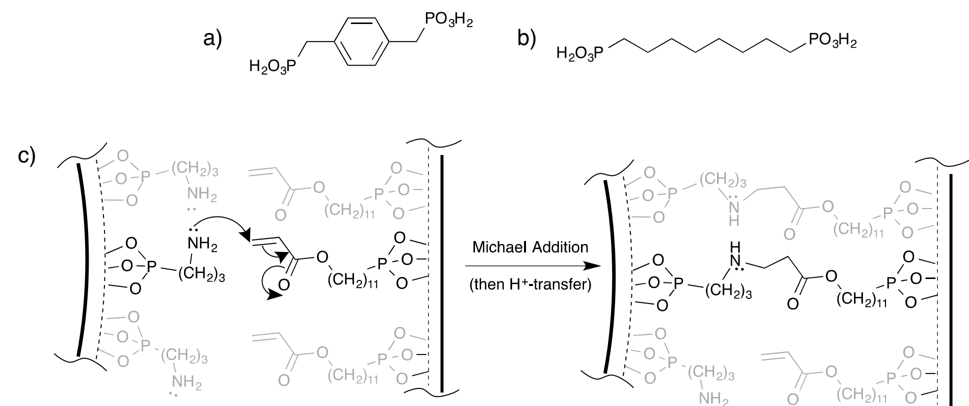

Figure B.3: (a) Benzene-BisPA and **(b)** Octane-BisPA modifiers used in Strategy 1; **(c)** Strategy 2.

For the modification of all surfaces in this work the modifiers were dissolved in ethanol, at varying concentrations, Table B.1. All modification processes took place at room temperature. Since Strategy 1 relies on using a single molecule terminated with identical phosphonic acid moieties to join both surfaces it is possible that during the modification process both phosphonic acid groups bond to the same surface. In effort to identify a modification procedure that maximized the number of surface modifiers that bridge the interface to join the two surfaces, two

Table B.1: Concentration of modifier solutions.

Molecular Linker	Concentration
Benzene-BisPA	1.0 mM
Octane-BisPA	5.0 mM
Acrylate-PA	0.5 mg/mL
Amino-PA	0.5 mg/mL

processes were explored. The first consisted of a stepwise modification procedure, where either the oxide coated CNT forest or the Ag foil was first modified by soaking it in solution and subsequently brought into contact with the other surface and bonded. The second process involved placing the foil into dry contact with the oxide coated CNT forest and then infiltrating the assembled structure with the solution containing the BisPA modifiers. In this case the modifiers may be able to bond to one or both surfaces while the solution evaporated over the course of several hours. For Strategy 2 the oxide coated CNTs were arbitrarily modified in the Acrylate-PA solution and the Ag foils in the Amino-PA solution.

B.1.4 Thermal Characterization

The photoacoustic method was used to measure the total thermal resistance of dry contact and modifier bonded CNT forests at an applied pressure of 140 kPa, as described in section 3.2.1.

B.2 Results

B.2.1Modification and Bonding

Strategy 1: Several CNT forest samples coated with oxide thicknesses of 0.5, 5, and 10 nm were modified and bonded using two processes outlined in the methods section of this appendix. For the samples prepared by the stepwise modification procedure no noticeable adhesion between the Al coated foil and CNT forest was achieved for either the Benzene-BisPA or Octane-BisPA modifiers. This indicates that the stepwise procedure failed to chemically link the two surfaces. Since phosphonic modification of oxide surfaces is a robust process [124, 135-137] it is likely that both phosphonic acid moieties of individual modifiers bonded to the same surface and failed

to join the interface. For samples that were assembled in a dry state and then infiltrated with BisPA solutions, qualitatively weak adhesion was observed, suggesting that relatively few of the modifiers linked the interface. It is likely that the majority of the modifiers again bonded to a single surface.

Strategy 2: Several CNT forests, coated with oxide thicknesses of 5 or 10 nm, and foil sets were modified and bonded using the Acrylate-PA and Amino-PA solutions respectively. Modification of the aluminum coated foil with the Amino-PA was verified via contact angle measurements. The contact angle of the unmodified foil was moderately hydrophobic at ~100°, and became hydrophilic, ~25°, after modification with the Amino-PA modifier, indicative of successful modification. It is possible that the modifier coverage could be improved by increasing the coverage of the oxide layer on the unmodified aluminum coated foil. This could be done by a simple O_2 plasma treatment of the surface. Nonetheless, all of samples prepared exhibited excellent adhesion, regardless of the oxide coating thickness.

B.2.2 Total Thermal Resistance

The total thermal resistance of interfaces that failed to bond or had delaminated ranged from ~60-100 mm^2-K/W, consistent with previous observations [156]. The thermal resistance of samples that exhibited appreciable adhesion, as well as those that did not (None/Non-bonded) is displayed in Table B.2. The best performing samples were those prepared using the Amino-PA and Acrylate-PA of Strategy 2. Effective bonding of these samples reduced the total thermal resistance from roughly 50 to 10 mm^2-K/W, an ~80% reduction. An electrically insulating TIM with a thermal resistance of only 10 mm^2-K/W is not available commercially. As such, the TIM structure and bonding strategy developed in this work could potentially fill a major technological gap in electronics packaging.

We have previously measured the thermal conductivity of oxide coated CNT forests at ~3.5 W/m-K [123, 156], and the growth substrate interface resistance at ≤ 1 mm^2-K/W [11].

Table B.2: Total thermal resistance of CNT forests.

Molecular Linker	CNT Forest Height [μm]	Oxide Thickness [nm]	Total Resistance [mm^2-K/W]
None/Non-bonded	15-40	0.5-10	60-100
Benzene-BisPA	20	0.5	21 ± 2
Acrylate/Amino-PA	30	10	11 ± 1

Using these values, the CNT forest height of 30 μm, and assuming that they remained unchanged during the modification and bonding process, the thermal resistance of the CNT tip interface was reduced from roughly 40 to $\lesssim$ 1 mm^2-K/W. This calculation suggests that phosphonic acid linking of the CNT tip interface can reduce the thermal resistance of the interface to a level where it no longer dominates the total resistance. Instead, the intrinsic thermal resistance of the CNT forest itself becomes the dominant component.

B.3 Conclusion

We explored using phosphonic-acid based surface modifiers to covalently bridge oxide coated CNT forest-metal oxide interfaces for thermal interface material applications. Surface modifiers comprised of bisphosphonic acids were found to be ineffective, as both phosphonic acid moieties typically bonded to the same surface and failed to bridge the interface. However, modification and reaction procedure utilizing acrylate and amino molecules containing phosphonic acid functional groups was found to successfully bond the interface. In doing so, the procedure reduced the total thermal resistance from roughly 50 to 10 mm^2-K/W. An electrically insulating TIM with a thermal resistance of only 10 mm^2-K/W is not currently commercially available. As such, the TIM structure and bonding strategy developed in this work could potentially fill a major technological gap in electronics packaging.

APPENDIX C

PATTERNED CNT FOREST-SOLDER TIMS

This research was carried out in collaboration with Dr. Anuradha Bulusu of the George W. Woodruff School of Mechanical Engineering at Georgia Tech and Mr. David H. Altman, Mr. Isaac S.G. Lee, Mr. Todd R. Gattuso, Mr. Anurag Gupta, and other staff members of the Raytheon Corporation.

C.1 Introduction and Motivation

Metal solders and films of sintered silver nanoparticles are currently being tested for use as thermal interface materials (TIMs) in high-temperature power electronics packaging. However, these materials have yet to produce the combination of low thermal resistance (< 5 mm^2K/W) and thermomechanical reliability that is required for future packaging technologies. These performance characteristics are difficult to achieve with metals due to competing effects. Specifically, the high elastic modulus of most solders (~10 GPa) necessitates the use of increased bond-line-thicknesses to alleviate stresses between packaging components with different CTEs. Concomitantly, the thermal resistance of a solder film increases proportionally with the bond-line-thickness [16]. Vertically-aligned CNT (VACNT) forests, comprised of individual CNTs with an axial thermal conductivity on the order of 200-3000 W/m-K [18] and an effective in-plane elastic modulus of only 8-300 MPa [164] are promising TIMs that could meet these demands. Yet their practical use has been limited by poor bonding strength, high thermal contact resistances, and relatively low effective thermal conductivity of the forests (because of the low volume fraction of CNTs in the forests). We propose to overcome these limits by fabricating CNT forest-solder composite TIMs to access a combination of thermal and mechanical properties that

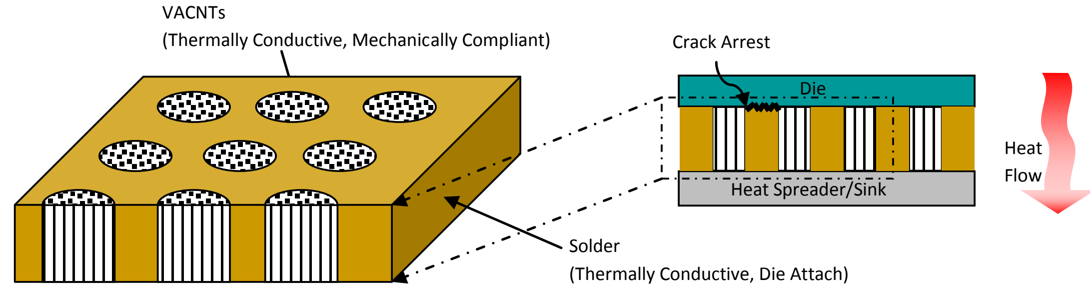

Figure C.1: Thermally conductive and mechanically compliant patterned CNT forest-solder TIM.

are unavailable with existing TIMs. CNT forests are synthesized in patterned configurations and pressed into a molten solder film to create a composite material with discrete regions of CNTs and solder, as shown in Figure C.1. The addition of the CNT forest regions will reduce the effective mechanical modulus of the composite enabling thinner bond lines and decreased thermal resistance, while the solder regions will provide mechanical attachment and the primary electrical and thermal transport pathway. The intermittent CNT forest regions will also improve the reliability of the package by serving as act as crack arrest zones that terminate crack propagation and prevent delamination. By tuning the volume ratio of CNT forest to solder the thermal conductivity, mechanical compliance, attachment strength, and CTE of the composite can be optimized to achieve reliable TIMs with thermal resistances less ≤ 5 mm^2-K/W. Here we demonstrate the synthesis of patterned CNT forest-solder composites and characterize their thermal resistance. Additional research is required to evaluate the reliability of these TIMs.

C.2 Methods

C.2.1 Synthesis of Patterned CNT forest-Al Foil Interposers

The catalyst for CNT growth was patterned onto both sides of 10 µm Al foil using a shadow mask and electron beam evaporation. The shadow mask patterns the catalyst into a grid of 100 µm diameter circles with a 250 µm center-center spacing. The catalyst stack and CNT forest growth recipe detailed in section 3.1 was used to grow CNT forest pillars from the patterned catalyst to

heights of 15 to 80 μm. A representative patterned CNT forest-Al foil interposer is shown in Figure C.2.

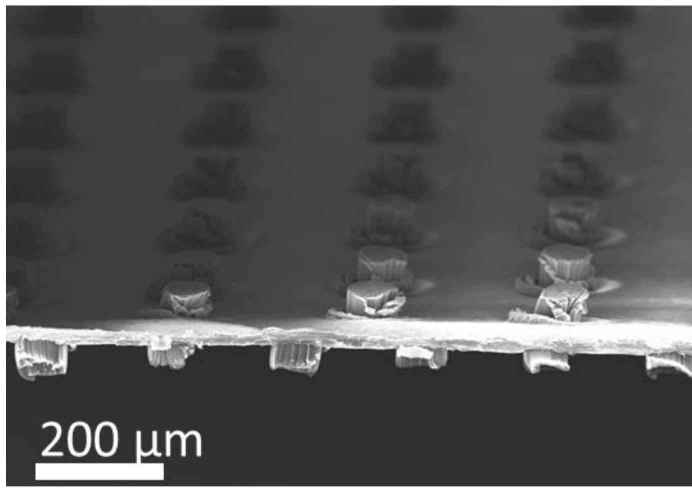

Figure C.2: Patterned CNT forests grown on both sides of 10 μm Al foil.

C.2.3 Fabrication and Bonding of Patterned CNT Forest-Solder TIMs

To facilitate wetting of the solder to the CNT forest pillars and Al foil 60 nm of Ti followed by 250 nm of Au was evaporated onto the surface of the CNT forest pillars and foil. The TIM was then bonded between two CuMo meter bars, also coated with 60 nm of Ti and 250 nm of Au, for thermal testing using two 12.7 to 25.4 μm thick Au/Sn solder foils under 200 kPa at 250 °C for 30 min. The excess solder was pressed out of the interface during bonding. After the TIMs were thermally tested the interfaces were broken apart and examined using SEM and energy dispersive X-ray spectroscopy (EDS). From the EDS it was revealed that for the majority of the TIM area the solder completely bridges the interface. Figure C.3 shows a SEM image of a separated TIM after thermal testing.

C.2.2 Thermal Characterization

The total thermal resistance (Equation 1.1) of the patterned CNT forest-solder TIMs was measured using a modified version [37] of the ASTM D5470 [55], shown schematically in Figure C.4. In this setup the TIM is solder bonded between two CuMo meter bars, as described above.

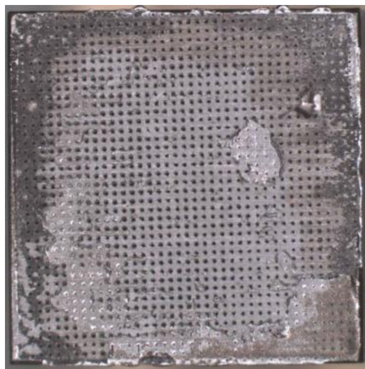

Figure C.3: SEM image of the CNT forest-composite TIM remnants left on the bottom meter bar after separating the interface. EDS of both meter bars suggest that the solder completely fills the interstitial space.

The end of one of the metal bars is maintained at a constant temperature T_{hot} and the end of the opposite bar at a constant temperature T_{cold}. This temperature difference creates a steady heat flow across the TIM, Q. Using thermocouples the temperature drop across the TIM, ΔT, is measured and the total thermal resistance of the TIM is extracted using the relation

$$R = \frac{\Delta T \cdot A}{Q}, \tag{C.1}$$

where A is the cross sectional area of the TIM.

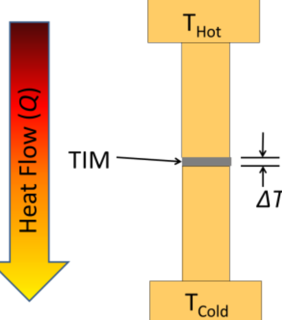

Figure C.4: Schematic of the modified ASTM D5470 setup used to measure the total resistance of CNT forest-solder TIMs.

C.3 Results

The total thermal resistance of 18 patterned CNT forest-solder TIMs was measured at an applied pressure of 135 kPa and is displayed in Figure C.5. The thermal resistances ranged from ~0.5 to 11 mm^2-K/W, comparable to solder only interfaces. No obvious dependence on the CNT forest pillar height was observed. These results suggest that the solder completely fills the interstitial space between the foil, meter bars, and adjacent CNT forest pillars, as was indicated by the EDS analysis. It also suggests that adding the patterned regions of CNT forests, ~13% of the cross sectional area, does not significantly degrade the thermal resistance of the composite structure. The thermal resistance of the TIMs was also measure under applied pressures of 270 and 405 kPa and observed to remain constant, indicating that the interfaces are well bonded.

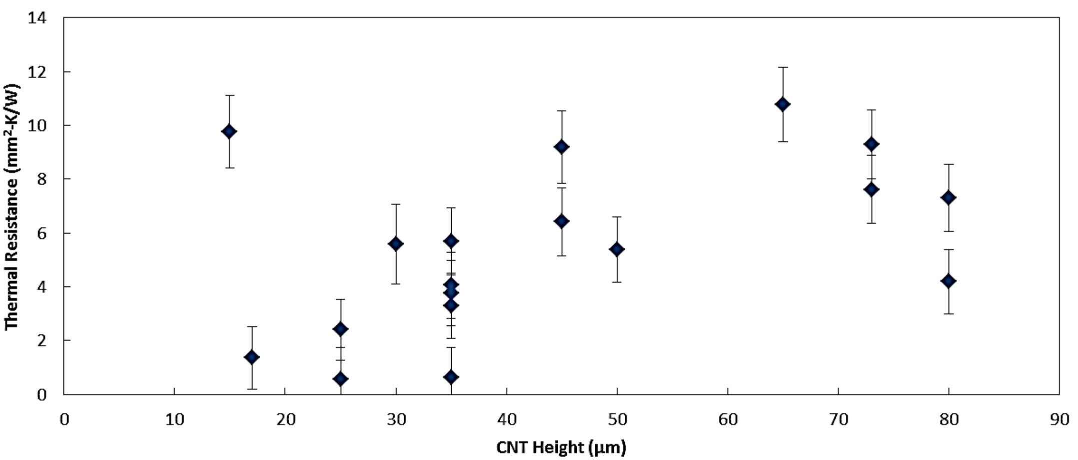

Figure C.5: Total thermal resistance of CNT forest-solder TIMs.

C.4 Conclusions and Recommendations

A methodology for fabricating patterned CNT forest-solder TIMs was demonstrated. The TIMs had thermal resistances ranging from ~0.5-11 mm^2-K/W, comparable to solder-only TIMs. As such, these results represent a promising first-step towards thermally conductive and reliable

TIMs. Future research should focus on optimizing the CNT/solder ratio to maximize the reliability of these TIMs.

APPENDIX D

MONTE CARLO TREATMENT OF UNCERTAINTY IN TDTR OF CNT FOREST TIMS

These uncertainty calculations were carried out in extensive collaboration with Mr. Thomas L. Bougher of the George W. Woodrfuff School of Mechanical Engineering.

D.1 Introduction

In Chapter 7 the uncertainty in the TDTR measurement of CNT forest TIMs was calculated using the method of Koh et al. [154], given by Equation 7.3. Due to low sensitivity (Equation 7.1) to and relatively large uncertainty in the Al transducer layer thickness (± 10 nm) the uncertainty in the Al-CNT forest interface resistance and CNT forest properties exceeded 100% and implied that parameters could be negative which is non-physical. For example, the Al-CNT forest interface resistance for bonded CNT forests ranged from ~100-600%. To better understand the true uncertainty in the measurement a Monte Carlo (MC) simulation was conducted. The MC simulation includes uncertainties due to background noise, error in setting the phase shift of the lock-in amplifier, noise in the measurement signal, and uncertainty in other fixed parameters, such as the thickness of the Al transducer layer. In the MC simulation values for each of these uncertain parameters are randomly sampled from a normal distribution to create a set of initial guess values and experimental data for fitting. 500 randomly generated sets are fit to create a distribution of probable values for the Al-CNT interface conductance, CNT forest thermal conductivity, and CNT forest specific heat.

D.2 Methods

MC simulations were carried out for TDTR scans of P3HT bonded, PyprPA bonded, and WCD samples (sample configuration described in Chapter 7) at a modulation frequency of 6.3 MHz. In these simulations the Al-CNT forest interface resistance, CNT forest thermal conductivity, and CNT forest specific heat are the unknown fitting parameters. Uncertainties due to background noise, error in setting the phase shift of the lock-in amplifier, and noise in the measurement signal are extracted from data collected during the experiment, whereas the uncertainties in parameters held constant during data fitting are prescribed. Table D.1 shows the uncertainties prescribed to sample parameters held constant during data fitting. An uncertainty of 3% and 7% were also prescribed for the pump and probe beam radii respectively. The uncertainty in the Al transducer film thickness and glass-Al transducer interface were taken from the TDTR and profilometry experiments described in Chapter 7. The remaining uncertainties were prescribed based on experience with TDTR measurements. The initial guess values given in Table 7.1 were used. The MC simulations were conducted for 500 iterations, over which all three fitting parameters achieved reasonable convergence. The convergence of the 10th, 50th, and 90th percentiles for the P3HT bonded Al-CNT forest interface resistance are shown in Figure D.1.

Table D.1: Uncertainty prescribed to fixed fitting parameters in MC simulations

% Uncertainty in Sample Parameters					
Layer	k [W/m-K]	C [J/kg-K]	ρ [kg/m^3]	L [nm]	R [mm^2-K/W]
Al	0.05	-	0.02	0.067	0.43
Glass	0.07	0.01	-	-	

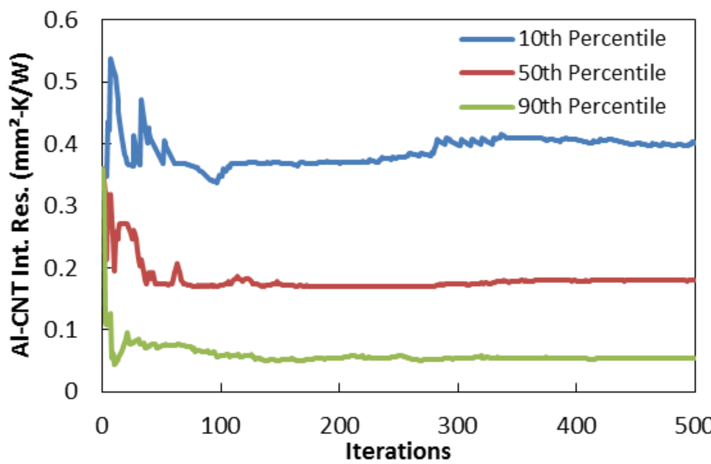

Figure D.1: Convergence of Al-CNT forest interface resistance over 500 iterations.

D.3 Results and Discussion

The MC simulation results for each of the unknown fitting parameters are displayed in Table D.2. Figure D.2 shows the parameter distributions for the P3HT bonded CNT forest, which are also representative of those for the PyprPA bonded and WCD CNT forests. The distributions for the CNT forest thermal conductivity and specific heat resemble slightly skewed normal distributions. The best-fit values for those parameters were taken as the 50th percentile of the distribution and the ± uncertainties were taken as the 5th and 95th percentiles to represent a 90% confidence interval. The distributions for the Al-CNT interface resistance are comparatively more skewed, as shown in Figure D.2a, with peaks shifted towards a resistance value of zero. The upper bound for the Al-CNT forest interface resistance is taken as the 90th percentile to also represent a 90% confidence interval. In contrast with the conventional uncertainty estimates of Chapter 7, the MC simulations do not predict negative values for any of the fitting parameters and represent a more rigorous treatment of uncertainty.

No difference, within the uncertainty, was observed in the best-fit values for the Al-CNT forest interface resistance, CNT forest thermal conductivity, and specific heat for the three

Table D.2: MC simulation results for bonded CNT forests.

Sample	Parameter		
	k [W/m-K]	C [J/kg-K]	R [mm^2-K/W]
P3HT	6 +5/-3	1260 +980/-670	0.18 +0.41/-0.13
PyprPA	6 +4/-3	1280 +850/-630	0.11 +0.43/-0.09
WCD	5 +4/-4	950 +1050/-490	0.15 +0.79/-0.12

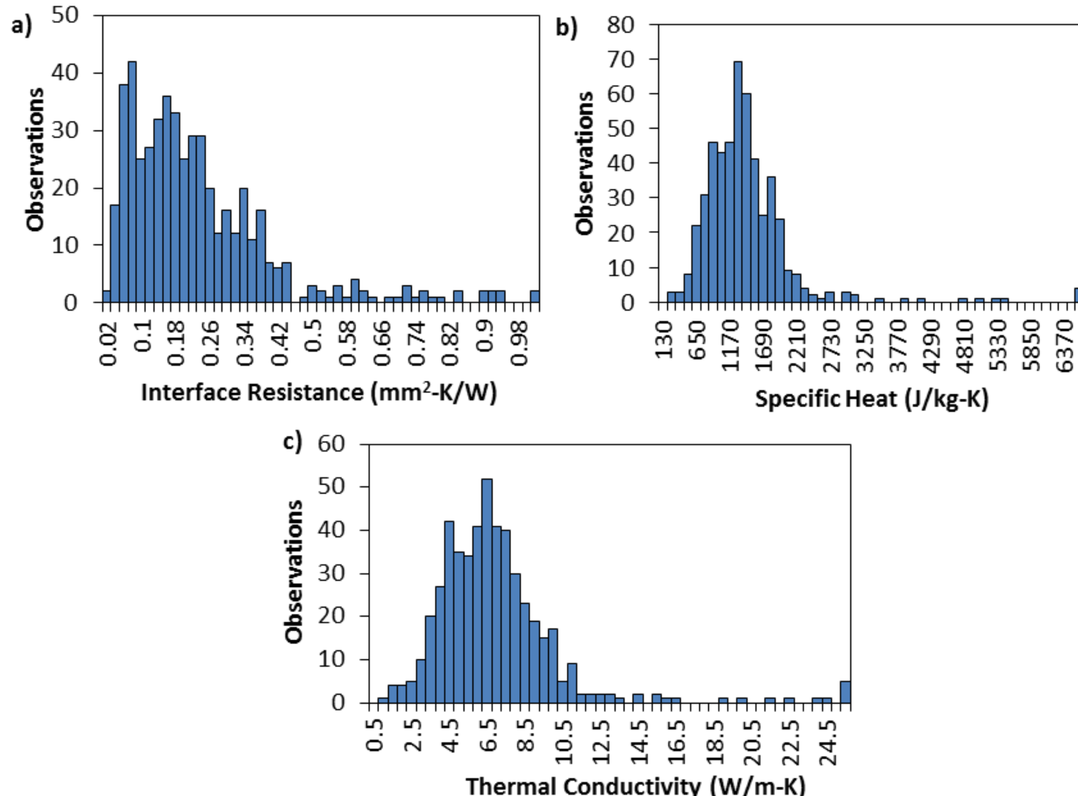

Figure D.2: MC simulation distributions for a P3HT bonded CNT forest.

sample types. Although, only a single modulation frequency, 6.3 MHz, was considered we do not expect significant changes in the best-fit values if other modulation frequencies are included. However, conducting multi-frequency MC simulations should reduce the uncertainty in the fitting parameters significantly. A challenge associated with the MC treatment of uncertainty is the computational expense required to complete the simulations. The single modulation frequency

data sets considered here required 10-15 hours each to complete on a standard desktop computer. However, utilization of a high performance computer and further optimization of the algorithm would lead to significant reductions in computation time. Additionally, the MC simulations do not provide explicit information on the contributions of individual sources of uncertainty to the total uncertainty.

D.4 Conclusions and Recommendations

MC methods were used to evaluate the true uncertainty in TDTR measurements of CNT forest interfaces. In contrast with the method of Koh et al. [154], used in the Chapter 7, the MC simulations do not predict negative values for fitting parameters, which are non-physical. No difference was observed in the Al-CNT forest interface resistance for P3HT bonded, PyprPA bonded, and WCD CNT forests. Future efforts should extend the MC simulations to multi-frequency data sets to understand the extent to which multiple modulations frequencies can reduce the uncertainty in the measurement.

REFERENCES

[1] A. Bar-Cohen, "DAPRA-BAA-11-09: Near Junction Thermal Transport," ed. https://www.fbo.gov/: United States of America, 2010.

[2] A. Bar-Cohen, "DARPA-BAA-12-50: Intrachip/Interchip Enhanced Cooling Fundamentals (ICECool Fundamentals)," ed. https://www.fbo.gov/: United States of America, 2012.

[3] T. Kenny, "DARPA-BAA-09-44: Active Cooling Modules (ACM)," ed. https://www.fbo.gov/: United States of America, 2009.

[4] T. Kenny, "DARPA BAA 08-15: Microtechnologies for Air-Cooled Exchangers (MACE)," ed. https://www.fbo.gov/: United States of America, 2008.

[5] T. Kenny, "DARPA-BAA-08-42: NanoThermal Interfaces (NTI)," ed. https://www.fbo.gov/: United States of America, 2008.

[6] T. Kenny, "DARPA BAA 07-36: Thermal Ground Plane (TGP) ", ed. https://www.fbo.gov/: United States of America, 2007.

[7] "International Technology Roadmap for Semiconductors," www.ITRS.net/home.html2012.

[8] S. V. Garimella, "Advances in mesoscale thermal management technologies for microelectronics," *Microelectronics Journal,* vol. 37, pp. 1165-1185, Nov 2006.

[9] J. H. Taphouse and B. A. Cola, "Nanostructured Thermal Interfaces," in *Annual Review of Heat Transfer*. vol. 18, ed: Begell House, in press.

[10] E. G. Wolff and D. A. Schneider, "Prediction of thermal contact resistance between polished surfaces," *International Journal of Heat and Mass Transfer,* vol. 41, pp. 3469-3482, 1998.

[11] B. A. Cola, J. Xu, C. R. Cheng, X. F. Xu, T. S. Fisher, and H. P. Hu, "Photoacoustic characterization of carbon nanotube array thermal interfaces," *Journal of Applied Physics,* vol. 101, Mar 2007.

[12] B. B. Mikic, "Thermal Contact Conductance - Theoretical Considerations," *International Journal of Heat and Mass Transfer,* vol. 17, pp. 205-214, 1974.

[13] F. P. Incropera and F. P. Incropera, *Fundamentals of heat and mass transfer*, 6th ed. Hoboken, NJ: John Wiley, 2007.

[14] C. V. Madhusudana, *Thermal contact conductance*. New York: Springer-Verlag, 1996.

[15] M. M. Yovanovich, "Four decades of research on thermal contact, gap, and joint resistance in microelectronics," *Ieee Transactions on Components and Packaging Technologies,* vol. 28, pp. 182-206, Jun 2005.

[16] W. T. Chen and C. W. Nelson, "Thermal Stress in Bonded Joints," *IBM Journal of Research and Development,* vol. 23, pp. 179-188, 1979.

[17] K. C. Otiaba, N. N. Ekere, R. S. Bhatti, S. Mallik, M. O. Alam, and E. H. Amalu, "Thermal interface materials for automotive electronic control unit: Trends, technology and R&D challenges," *Microelectronics Reliability,* vol. 51, pp. 2031-2043, Dec 2011.

[18] A. M. Marconnet, M. A. Panzer, and K. E. Goodson, "Thermal conduction phenomena in carbon nanotubes and related nanostructured materials," *Reviews of Modern Physics,* vol. 85, pp. 1295-1326, 2013.

[19] M. S. Dresselhaus, G. Dresselhaus, and P. Avouris, *Carbon nanotubes : synthesis, structure, properties, and applications*. Berlin ; New York: Springer, 2001.

[20] P. Kim, L. Shi, A. Majumdar, and P. L. McEuen, "Thermal transport measurements of individual multiwalled nanotubes," *Physical Review Letters,* vol. 87, Nov 2001.

[21] E. Pop, D. Mann, Q. Wang, K. E. Goodson, and H. J. Dai, "Thermal conductance of an individual single-wall carbon nanotube above room temperature," *Nano Letters,* vol. 6, pp. 96-100, Jan 2006.

[22] J. Hone, M. Whitney, C. Piskoti, and A. Zettl, "Thermal conductivity of single-walled carbon nanotubes," *Physical Review B,* vol. 59, pp. R2514-R2516, Jan 1999.

[23] J. K. Yang, Y. Yang, S. W. Waltermire, T. Gutu, A. A. Zinn, T. T. Xu, Y. F. Chen, and D. Y. Li, "Measurement of the Intrinsic Thermal Conductivity of a Multiwalled Carbon Nanotube and Its Contact Thermal Resistance with the Substrate," *Small,* vol. 7, pp. 2334-2340, Aug 2011.

[24] S. Berber, Y. K. Kwon, and D. Tomanek, "Unusually high thermal conductivity of carbon nanotubes," *Physical Review Letters,* vol. 84, pp. 4613-4616, May 2000.

[25] B. Peng, M. Locascio, P. Zapol, S. Y. Li, S. L. Mielke, G. C. Schatz, and H. D. Espinosa, "Measurements of near-ultimate strength for multiwalled carbon nanotubes and irradiation-induced crosslinking improvements," *Nature Nanotechnology,* vol. 3, pp. 626-631, Oct 2008.

[26] D. Bom, R. Andrews, D. Jacques, J. Anthony, B. L. Chen, M. S. Meier, and J. P. Selegue, "Thermogravimetric analysis of the oxidation of multiwalled carbon nanotubes: Evidence for the role of defect sites in carbon nanotube chemistry," *Nano Letters,* vol. 2, pp. 615-619, Jun 2002.

[27] J. Xu and T. S. Fisher, "Enhanced thermal contact conductance using carbon nanotube arrays," in *Thermal and Thermomechanical Phenomena in Electronic Systems, 2004. ITHERM '04. The Ninth Intersociety Conference on*, 2004, pp. 549-555 Vol.2.

[28] X. J. Hu, M. Panzer, and K. E. Goodson, "Thermal characterization of two opposing carbon nanotube arrays using diffraction-limited infrared microscopy," in *Proceedings of the Asme Heat Transfer Division 2005, Vol 2*. vol. 376-2, ed New York: Amer Soc Mechanical Engineers, 2005, pp. 835-839.

[29] T. Tong, Y. Zhao, L. Delzeit, A. Kashani, A. Majumdar, and M. Meyyappan, "Vertically aligned multi-walled carbon nanotube arrays as thermal interface materials and measurement technique," in *Proceedings of the ASME Heat Transfer Division 2005*. vol. 376-2, ed New York: Amer Soc Mechanical Engineers, 2005, pp. 777-783.

[30] J. Xu and T. S. Fisher, "Enhanced thermal contact conductance using carbon nanotube array interfaces," *Ieee Transactions on Components and Packaging Technologies,* vol. 29, pp. 261-267, Jun 2006.

[31] X. J. Hu, A. A. Padilla, J. Xu, T. S. Fisher, and K. E. Goodson, "3-omega measurements of vertically oriented carbon nanotubes on silicon," *Journal of Heat Transfer-Transactions of the Asme,* vol. 128, pp. 1109-1113, Nov 2006.

[32] T. Tong, Y. Zhao, L. Delzeit, A. Kashani, M. Meyyappan, and A. Majumdar, "Dense, vertically aligned multiwalled carbon nanotube arrays as thermal interface materials," *Ieee Transactions on Components and Packaging Technologies,* vol. 30, pp. 92-100, Mar 2007.

[33] W. Lin, R. W. Zhang, K. S. Moon, and C. P. Wong, "Molecular phonon couplers at carbon nanotube/substrate interface to enhance interfacial thermal transport," *Carbon,* vol. 48, pp. 107-113, Jan 2010.

[34] R. Cross, B. A. Cola, T. Fisher, X. F. Xu, K. Gall, and S. Graham, "A metallization and bonding approach for high performance carbon nanotube thermal interface materials," *Nanotechnology,* vol. 21, Nov 2010.

[35] A. Hamdan, J. Cho, R. Johnson, J. Jiao, D. Bahr, R. Richards, and C. Richards, "Evaluation of a thermal interface material fabricated using thermocompression bonding of carbon nanotube turf," *Nanotechnology,* vol. 21, Jan 2010.
[36] D. D. L. Chung, "Materials for thermal conduction," *Applied Thermal Engineering,* vol. 21, pp. 1593-1605, Nov 2001.
[37] J. R. Wasniewski, D. H. Altman, S. L. Hodson, T. S. Fisher, A. Bulusu, S. Graham, and B. A. Cola, "Characterization of Metallically Bonded Carbon Nanotube-Based Thermal Interface Materials Using a High Accuracy 1D Steady-State Technique," *Journal of Electronic Packaging,* vol. 134, Jun 2012.
[38] R. Prasher, "Predicting the thermal resistance of nanosized constrictions," *Nano Letters,* vol. 5, pp. 2155-2159, Nov 2005.
[39] R. Prasher, "Thermal conductance of single-walled carbon nanotube embedded in an elastic half-space," *Applied Physics Letters,* vol. 90, Apr 2007.
[40] R. Prasher, "Thermal boundary resistance and thermal conductivity of multiwalled carbon nanotubes," *Physical Review B,* vol. 77, Feb 2008.
[41] Z. Y. Ong and E. Pop, "Molecular dynamics simulation of thermal boundary conductance between carbon nanotubes and SiO2," *Physical Review B,* vol. 81, Apr 2010.
[42] J. Hirotani, T. Ikuta, T. Nishiyama, and K. Takahashi, "Thermal boundary resistance between the end of an individual carbon nanotube and a Au surface," *Nanotechnology,* vol. 22, Aug 2011.
[43] S. Shenogin, J. Gengler, A. Roy, A. A. Voevodin, and C. Muratore, "Molecular dynamics studies of thermal boundary resistance at carbon-metal interfaces," *Scripta Materialia,* vol. 69, pp. 100-103, Jul 2013.
[44] B. A. Cola, J. Xu, and T. S. Fisher, "Contact mechanics and thermal conductance of carbon nanotube array interfaces," *International Journal of Heat and Mass Transfer,* vol. 52, pp. 3490-3503, Jul 2009.
[45] M. A. Panzer, G. Zhang, D. Mann, X. Hu, E. Pop, H. Dai, and K. E. Goodson, "Thermal properties of metal-coated vertically aligned single-wall nanotube arrays," *Journal of Heat Transfer-Transactions of the Asme,* vol. 130, May 2008.
[46] M. A. Panzer, H. M. Duong, J. Okawa, J. Shiomi, B. L. Wardle, S. Maruyama, and K. E. Goodson, "Temperature-Dependent Phonon Conduction and Nanotube Engagement in Metalized Single Wall Carbon Nanotube Films," *Nano Letters,* vol. 10, pp. 2395-2400, Jul 2010.
[47] D. D. L. Chung, "Thermal interface materials," *Journal of Materials Engineering and Performance,* vol. 10, pp. 56-59, Feb 2001.
[48] D. L. Saums, "Advances in Thermal Interface Materials for Power LED Applications," in *Thermal Management for LED Applications*. vol. 2, C. J. M. Lasance and A. Poppe, Eds., ed: Springer New York, 2014, pp. 299-346.
[49] I. Corporation. (November 29). Available: http://www.indium.com/thermal-interface-materials/ribbon-and-foil/
[50] (November 29). Available: http://www.arcticsilver.com/as5.htm
[51] A. Castle. (2010, November 29). *How-To: Properly Apply Thermal Paste and Install a CPU*. Available: http://www.maximumpc.com/article/howtos/howto_install_cpu_and_apply_thermal_paste
[52] T. Bahman. (2005, November 29). *Choosing a heat-sink attachment system*. Available: http://www.electronicproducts.com/Passive_Components/Choosing_a_heat-sink-attachment_system.aspx

[53] J. P. Gwinn and R. L. Webb, "Performance and testing of thermal interface materials," *Microelectronics Journal,* vol. 34, pp. 215-222, 2003.

[54] C. J. M. Lasance, C. T. Murray, D. L. Saums, and M. Rencz, "Challenges in thermal interface material testing," in *Semiconductor Thermal Measurement and Management Symposium, 2006 IEEE Twenty-Second Annual IEEE*, 2006, pp. 42-49.

[55] ASTM, "Standard Test Method for Thermal Transmission Properties of Thermally Conductive Electrical Insulating Materials," in *D5470*, ed. West Conshohocken, Pennsylvania: ASTM International, 2006.

[56] P. L. Kapitza, "Heat transfer and superfluidity of helium II," *Physical Review,* vol. 60, pp. 354-355, Aug 1941.

[57] E. T. Swartz and R. O. Pohl, "Thermal boundary resistance," *Reviews of Modern Physics,* vol. 61, pp. 605-668, 1989.

[58] W. A. Little, "The Transport of Heat between Dissimilar Solids at Low Temperatures," *Canadian Journal of Physics,* vol. 37, pp. 334-349, 1959.

[59] G. Chen, *Nanoscale energy transport and conversion : a parallel treatment of electrons, molecules, phonons, and photons*. Oxford ; New York: Oxford University Press, 2005.

[60] I. M. Khalatnikov, *Journal of Experimental and Theoretical Physics (USSR),* vol. 22, pp. 687-704, 1952.

[61] Z. M. Zhang, *Nano/microscale heat transfer*. New York, NY: McGraw-Hill, 2007.

[62] E. T. Swartz and R. O. Pohl, "Thermal-Boundary Resistance," *Reviews of Modern Physics,* vol. 61, pp. 605-668, Jul 1989.

[63] J. R. Olson and R. O. Pohl, "Kapitza Resistance between Silicon and He-4," *Journal of Low Temperature Physics,* vol. 94, pp. 539-550, Mar 1994.

[64] P. E. Phelan, "Application of diffuse mismatch theory to the prediction of thermal boundary resistance in thin-film high-T-c superconductors," *Journal of Heat Transfer-Transactions of the Asme,* vol. 120, pp. 37-43, Feb 1998.

[65] P. Reddy, K. Castelino, and A. Majumdar, "Diffuse mismatch model of thermal boundary conductance using exact phonon dispersion," *Applied Physics Letters,* vol. 87, Nov 2005.

[66] J. C. Duda, T. E. Beechem, J. L. Smoyer, P. M. Norris, and P. E. Hopkins, "Role of dispersion on phononic thermal boundary conductance," *Journal of Applied Physics,* vol. 108, Oct 2010.

[67] L. De Bellis, P. E. Phelan, and R. S. Prasher, "Variations of acoustic and diffuse mismatch models in predicting thermal-boundary resistance," *Journal of Thermophysics and Heat Transfer,* vol. 14, pp. 144-150, Apr-Jun 2000.

[68] A. Majumdar, "Effect of Interfacial Roughness on Phonon Radiative Heat-Conduction," *Journal of Heat Transfer-Transactions of the Asme,* vol. 113, pp. 797-805, Nov 1991.

[69] P. E. Hopkins, L. M. Phinney, J. R. Serrano, and T. E. Beechem, "Effects of surface roughness and oxide layer on the thermal boundary conductance at aluminum/silicon interfaces," *Physical Review B,* vol. 82, 2010.

[70] R. S. Prasher and P. E. Phelan, "A scattering-mediated acoustic mismatch model for the prediction of thermal boundary resistance (vol 123, pg 105, 2001)," *Journal of Heat Transfer-Transactions of the Asme,* vol. 123, pp. 1194-1194, Dec 2001.

[71] T. Beechem, S. Graham, P. Hopkins, and P. Norris, "Role of interface disorder on thermal boundary conductance using a virtual crystal approach," *Applied Physics Letters,* vol. 90, p. 054104, 2007.

[72] M. M. Yovanovich and E. E. Marotta, "Thermal Spreading and Contact Resistances," in *Heat Transfer Handbook*, A. Bejan and A. D. Kraus, Eds., ed New York: Wiley, 2003, pp. 261-393.

[73] M. G. Cooper, B. B. Mikic, and Yovanovi.Mm, "Thermal Contact Conductance," *International Journal of Heat and Mass Transfer,* vol. 12, pp. 279-&, 1969.
[74] R. J. Stoner and H. J. Maris, "Kapitza Conductance and Heat-Flow between Solids at Temperatures from 50 to 300 K," *Physical Review B,* vol. 48, pp. 16373-16387, Dec 1993.
[75] L. Hu, L. F. Zhang, M. Hu, J. S. Wang, B. W. Li, and P. Keblinski, "Phonon interference at self-assembled monolayer interfaces: Molecular dynamics simulations," *Physical Review B,* vol. 81, Jun 2010.
[76] N. Shenogina, R. Godawat, P. Keblinski, and S. Garde, "How Wetting and Adhesion Affect Thermal Conductance of a Range of Hydrophobic to Hydrophilic Aqueous Interfaces," *Physical Review Letters,* vol. 102, Apr 2009.
[77] M. Hu, P. Keblinski, and P. K. Schelling, "Kapitza conductance of silicon-amorphous polyethylene interfaces by molecular dynamics simulations," *Physical Review B,* vol. 79, Mar 2009.
[78] R. Prasher, "Acoustic mismatch model for thermal contact resistance of van der Waals contacts," *Applied Physics Letters,* vol. 94, Jan 2009.
[79] M. D. Losego, M. E. Grady, N. R. Sottos, D. G. Cahill, and P. V. Braun, "Effects of chemical bonding on heat transport across interfaces," *Nature Materials,* vol. 11, pp. 502-506, Jun 2012.
[80] M. Schoenberg, "Elastic Wave Behavior across Linear Slip Interfaces," *Journal of the Acoustical Society of America,* vol. 68, pp. 1516-1521, 1980.
[81] M. A. Panzer and K. E. Goodson, "Thermal resistance between low-dimensional nanostructures and semi-infinite media," *Journal of Applied Physics,* vol. 103, p. 094301, 2008.
[82] M. Bedewy, E. R. Meshot, H. C. Guo, E. A. Verploegen, W. Lu, and A. J. Hart, "Collective Mechanism for the Evolution and Self-Termination of Vertically Aligned Carbon Nanotube Growth," *Journal of Physical Chemistry C,* vol. 113, pp. 20576-20582, Dec 2009.
[83] L. Zhang, Z. R. Li, Y. Q. Tan, G. Lolli, N. Sakulchaicharoen, F. G. Requejo, B. S. Mun, and D. E. Resasco, "Influence of a top crust of entangled nanotubes on the structure of vertically aligned forests of single-walled carbon nanotubes," *Chemistry of Materials,* vol. 18, pp. 5624-5629, Nov 2006.
[84] V. Bahadur, J. Xu, Y. Liu, and T. S. Fisher, "Thermal resistance of nanowire-plane interfaces," *Journal of Heat Transfer-Transactions of the Asme,* vol. 127, pp. 664-668, Jun 2005.
[85] M. T. Pettes and L. Shi, "Thermal and Structural Characterizations of Individual Single-, Double-, and Multi-Walled Carbon Nanotubes," *Advanced Functional Materials,* vol. 19, pp. 3918-3925, 2009.
[86] K. T. Regner, D. P. Sellan, Z. Su, C. H. Amon, A. J. McGaughey, and J. A. Malen, "Broadband phonon mean free path contributions to thermal conductivity measured using frequency domain thermoreflectance," *Nat Commun,* vol. 4, p. 1640, 2013.
[87] G. R. McGee, M. H. Schankula, and M. M. Yovanovich, "Thermal-Resistance of Cylinder-Flat Contacts - Theoretical-Analysis and Experimental-Verification of a Line-Contact Model," *Nuclear Engineering and Design,* vol. 86, pp. 369-381, 1985 1985.
[88] S. Sadasivam, Y. Che, Z. Huang, L. Chen, S. Kumar, and T. S. Fisher, "The atomistic Green's function method for interfacial phonon transport," *Ann. Rev. Heat Transfer,* vol. 17, pp. 89-145, 2014.

[89] I. Srivastava, S. Sadasivam, K. C. Smith, and T. S. Fisher, "Combined Microstructure and Heat Conduction Modeling of Heterogeneous Interfaces and Materials," *Journal of Heat Transfer-Transactions of the Asme,* vol. 135, Jun 2013.

[90] M. J. Buehler, "Mesoscale modeling of mechanics of carbon nanotubes: Self-assembly, self-folding, and fracture," *Journal of Materials Research,* vol. 21, pp. 2855-2869, 2011.

[91] C. Van Wyk, "20—NOTE ON THE COMPRESSIBILITY OF WOOL," *Journal of the Textile Institute Transactions,* vol. 37, pp. T285-T292, 1946.

[92] S. De Jong, J. Snaith, and N. Michie, "A mechanical model for the lateral compression of woven fabrics," *Textile Research Journal,* vol. 56, pp. 759-767, 1986.

[93] M. S. Dresselhaus, G. Dresselhaus, R. Saito, and A. Jorio, "Raman spectroscopy of carbon nanotubes," *Physics Reports-Review Section of Physics Letters,* vol. 409, pp. 47-99, Mar 2005.

[94] B. A. Cola, X. F. Xu, and T. S. Fisher, "Increased real contact in thermal interfaces: A carbon nanotube/foil material," *Applied Physics Letters,* vol. 90, Feb 2007.

[95] T. L. Bergman and F. P. Incropera, *Fundamentals of heat and mass transfer*, 7th ed. Hoboken, NJ: Wiley, 2011.

[96] H. P. Hu, X. W. Wang, and X. F. Xu, "Generalized theory of the photoacoustic effect in a multilayer material," *Journal of Applied Physics,* vol. 86, pp. 3953-3958, Oct 1999.

[97] X. Wang, B. A. Cola, T. L. Bougher, S. L. Hodson, T. S. Fisher, and X. Xu, "Photoacoustic Technique for Thermal Conductivity and Thermal Interface Measurements," in *Annual Review of Heat Transfer*. vol. 16, ed, 2013, pp. 135-157.

[98] W. H. Press, *Numerical recipes : the art of scientific computing*, 3rd ed. Cambridge, UK ; New York: Cambridge University Press, 2007.

[99] A. J. Schmidt, R. Cheaito, and M. Chiesa, "A frequency-domain thermoreflectance method for the characterization of thermal properties," *Review of Scientific Instruments,* vol. 80, Sep 2009.

[100] Y. X. Wang, J. Y. Park, Y. K. Koh, and D. G. Cahill, "Thermoreflectance of metal transducers for time-domain thermoreflectance," *Journal of Applied Physics,* vol. 108, Aug 2010.

[101] D. G. Cahill, "Analysis of heat flow in layered structures for time-domain thermoreflectance," *Review of Scientific Instruments,* vol. 75, pp. 5119-5122, Dec 2004.

[102] A. J. Schmidt, X. Y. Chen, and G. Chen, "Pulse accumulation, radial heat conduction, and anisotropic thermal conductivity in pump-probe transient thermoreflectance," *Review of Scientific Instruments,* vol. 79, Nov 2008.

[103] A. Schmidt, M. Chiesa, X. Y. Chen, and G. Chen, "An optical pump-probe technique for measuring the thermal conductivity of liquids," *Review of Scientific Instruments,* vol. 79, Jun 2008.

[104] B. C. Gundrum, D. G. Cahill, and R. S. Averback, "Thermal conductance of metal-metal interfaces," *Physical Review B,* vol. 72, Dec 2005.

[105] A. J. Schmidt, K. C. Collins, A. J. Minnich, and G. Chen, "Thermal conductance and phonon transmissivity of metal-graphite interfaces," *Journal of Applied Physics,* vol. 107, May 2010.

[106] Y. Gao, A. M. Marconnet, R. Xiang, S. Maruyama, and K. E. Goodson, "Heat Capacity, Thermal Conductivity, and Interface Resistance Extraction for Single-Walled Carbon Nanotube Films Using Frequency-Domain Thermoreflectance," *Components, Packaging and Manufacturing Technology, IEEE Transactions on,* vol. PP, pp. 1-1, 2013.

[107] S. Kaur, N. Raravikar, B. A. Helms, R. Prasher, and D. F. Ogletree, "Enhanced thermal transport at covalently functionalized carbon nanotube array interfaces," *Nat Commun,* vol. 5, p. 3082, 2014.

[108] C. Wei, X. Zheng, D. G. Cahill, and J. C. Zhao, "Invited article: micron resolution spatially resolved measurement of heat capacity using dual-frequency time-domain thermoreflectance," *Rev Sci Instrum,* vol. 84, p. 071301, Jul 2013.

[109] J. Liu, J. Zhu, M. Tian, X. Gu, A. Schmidt, and R. Yang, "Simultaneous measurement of thermal conductivity and heat capacity of bulk and thin film materials using frequency-dependent transient thermoreflectance method," *Rev Sci Instrum,* vol. 84, p. 034902, Mar 2013.

[110] P. E. Hopkins, J. R. Serrano, L. M. Phinney, S. P. Kearney, T. W. Grasser, and C. T. Harris, "Criteria for Cross-Plane Dominated Thermal Transport in Multilayer Thin Film Systems During Modulated Laser Heating," *Journal of Heat Transfer,* vol. 132, p. 081302, 2010.

[111] A. Y. Cao, P. L. Dickrell, W. G. Sawyer, M. N. Ghasemi-Nejhad, and P. M. Ajayan, "Super-compressible foamlike carbon nanotube films," *Science,* vol. 310, pp. 1307-1310, Nov 2005.

[112] S. D. Mesarovic, C. M. McCarter, D. F. Bahr, H. Radhakrishnan, R. F. Richards, C. D. Richards, D. McClain, and J. Jiao, "Mechanical behavior of a carbon nanotube turf," *Scripta Materialia,* vol. 56, pp. 157-160, Jan 2007.

[113] M. R. Maschmann, Q. H. Zhang, F. Du, L. M. Dai, and J. Baur, "Length dependent foam-like mechanical response of axially indented vertically oriented carbon nanotube arrays," *Carbon,* vol. 49, pp. 386-397, Feb 2011.

[114] P. Pour Shahid Saeed Abadi, S. B. Hutchens, J. R. Greer, B. A. Cola, and S. Graham, "Effects of morphology on the micro-compression response of carbon nanotube forests," *Nanoscale,* vol. 4, pp. 3373-3380, 2012.

[115] X. C. Gui, Z. P. Zeng, A. Y. Cao, Z. Q. Lin, H. Q. Zeng, R. Xiang, T. Z. Wu, Y. Zhu, and Z. K. Tang, "Elastic shape recovery of carbon nanotube sponges in liquid oil," *Journal of Materials Chemistry,* vol. 22, pp. 18300-18305, 2012.

[116] P. P. Abadi, M. R. Maschmann, S. M. Mortuza, S. Banerjee, J. W. Baur, S. Graham, and B. A. Cola, "Reversible Tailoring of Mechanical Properties of Carbon Nanotube Forests by Immersing in Solvents," *Carbon (accepted),* 2013.

[117] A. Misra, P. Kumar, J. R. Raney, A. Singhal, L. Lattanzi, and C. Daraio, "Effect of fluid medium on mechanical behavior of carbon nanotube foam," *Applied Physics Letters,* vol. 104, p. 221910, 2014.

[118] N. Chakrapani, B. Q. Wei, A. Carrillo, P. M. Ajayan, and R. S. Kane, "Capillarity-driven assembly of two-dimensional cellular carbon nanotube foams," *Proceedings of the National Academy of Sciences of the United States of America,* vol. 101, pp. 4009-4012, Mar 2004.

[119] S. Kaur, S. Sahoo, P. Ajayan, and R. S. Kane, "Capillarity-driven assembly of carbon nanotubes on substrates into dense vertically aligned arrays," *Advanced Materials,* vol. 19, pp. 2984-+, Oct 2007.

[120] Z. Liu, N. Bajwa, L. Ci, S. H. Lee, S. Kar, P. M. Ajayan, and J. Q. Lu, "Densification of carbon nanotube bundles for interconnect application," in *Proceedings of the IEEE 2007 International Interconnect Technology Conference*, ed, 2007, pp. 201-203.

[121] S. Tawfick, M. De Volder, and A. J. Hart, "Structurally Programmed Capillary Folding of Carbon Nanotube Assemblies," *Langmuir,* vol. 27, pp. 6389-6394, May 2011.

[122] J. A. Dean and N. A. Lange, "Lange's handbook of chemistry," ed. New York: McGraw-Hill, 1973, p. v.

[123] T. L. Bougher, C. J. Vasquez, and B. A. Cola, "Thermal Conductivity Measurement of Bare Carbon Nanotube Films Using the Photoacoustic Technique," in *15th International Heat Transfer Conference*, Kyoto Japan, 2014.
[124] J. H. Taphouse, O. N. L. Smith, S. R. Marder, and B. A. Cola, "A Pyrenylpropyl Phosphonic Acid Surface Modifier for Mitigating the Thermal Resistance of Carbon Nanotube Contacts," *Advanced Functional Materials,* vol. 24, pp. 465-471, 2014.
[125] L. T. Qu, L. M. Dai, M. Stone, Z. H. Xia, and Z. L. Wang, "Carbon nanotube arrays with strong shear binding-on and easy normal lifting-off," *Science,* vol. 322, pp. 238-242, Oct 2008.
[126] Y. Zhao, T. Tong, L. Delzeit, A. Kashani, M. Meyyappan, and A. Majumdar, "Interfacial energy and strength of multiwalled-carbon-nanotube-based dry adhesive," *Journal of Vacuum Science & Technology B,* vol. 24, pp. 331-335, Jan-Feb 2006.
[127] L. Qu and L. Dai, "Gecko-foot-mimetic aligned single-walled carbon nanotube dry adhesives with unique electrical and thermal properties," *Advanced Materials,* vol. 19, pp. 3844-+, Nov 2007.
[128] P. Pour Shahid Saeed Abadi, S. B. Hutchens, J. R. Greer, B. A. Cola, and S. Graham, "Buckling-driven delamination of carbon nanotube forests," *Applied Physics Letters,* vol. 102, p. 223103, 2013.
[129] S. Tawfick, Z. Z. Zhao, M. Maschmann, A. Brieland-Shoultz, M. De Volder, J. W. Baur, W. Lu, and A. J. Hart, "Mechanics of Capillary Forming of Aligned Carbon Nanotube Assemblies," *Langmuir,* vol. 29, pp. 5190-5198, Apr 2013.
[130] M. F. L. De Volder, S. J. Park, S. H. Tawfick, D. O. Vidaud, and A. J. Hart, "Fabrication and electrical integration of robust carbon nanotube micropillars by self-directed elastocapillary densification," *Journal of Micromechanics and Microengineering,* vol. 21, p. 045033, 2011.
[131] S. G. Stepanian, V. A. Karachevtsev, A. Y. Glamazda, U. Dettlaff-Weglikowska, and L. Adamowicz, "Combined Raman scattering and ab initio investigation of the interaction between pyrene and carbon SWNT," *Molecular Physics,* vol. 101, pp. 2609-2614, Aug 2003.
[132] Q. Yang, L. Shuai, J. Zhou, F. C. Lu, and X. J. Pan, "Functionalization of Multiwalled Carbon Nanotubes by Pyrene-Labeled Hydroxypropyl Cellulose," *Journal of Physical Chemistry B,* vol. 112, pp. 12934-12939, Oct 2008.
[133] P. H. Mutin, G. Guerrero, and A. Vioux, "Organic-inorganic hybrid materials based on organophosphorus coupling molecules: from metal phosphonates to surface modification of oxides," *Comptes Rendus Chimie,* vol. 6, pp. 1153-1164, Aug-Oct 2003.
[134] P. H. Mutin, G. Guerrero, and A. Vioux, "Hybrid materials from organophosphorus coupling molecules," *Journal of Materials Chemistry,* vol. 15, pp. 3761-3768, 2005.
[135] P. Kim, N. M. Doss, J. P. Tillotson, P. J. Hotchkiss, M. J. Pan, S. R. Marder, J. Y. Li, J. P. Calame, and J. W. Perry, "High Energy Density Nanocomposites Based on Surface-Modified BaTiO3 and a Ferroelectric Polymer," *Acs Nano,* vol. 3, pp. 2581-2592, Sep 2009.
[136] P. J. Hotchkiss, M. Malicki, A. J. Giordano, N. R. Armstrong, and S. R. Marder, "Characterization of phosphonic acid binding to zinc oxide," *Journal of Materials Chemistry,* vol. 21, pp. 3107-3112, 2011.
[137] S. A. Paniagua, P. J. Hotchkiss, S. C. Jones, S. R. Marder, A. Mudalige, F. S. Marrikar, J. E. Pemberton, and N. R. Armstrong, "Phosphonic acid modification of indium-tin oxide electrodes: Combined XPS/UPS/contact angle studies," *Journal of Physical Chemistry C,* vol. 112, pp. 7809-7817, May 2008.

[138] S. Gastaldi and D. Stien, "PAH-supported tin hydride: a new tin reagent easily removable from reaction mixtures," *Tetrahedron Letters,* vol. 43, pp. 4309-4311, Jun 2002.
[139] T. J. Simmons, J. Bult, D. P. Hashim, R. J. Linhardt, and P. M. Ajayan, "Noncovalent Functionalization as an Alternative to Oxidative Acid Treatment of Single Wall Carbon Nanotubes With Applications for Polymer Composites," *Acs Nano,* vol. 3, pp. 865-870, Apr 2009.
[140] X. Wallart, C. H. de Villeneuve, and P. Allongue, "Truly quantitative XPS characterization of organic monolayers on silicon: Study of alkyl and alkoxy monolayers on H-Si(111)," *Journal of the American Chemical Society,* vol. 127, pp. 7871-7878, Jun 2005.
[141] M. R. Weatherspoon, S. M. Allan, E. Hunt, Y. Cai, and K. H. Sandhage, "Sol-gel synthesis on self-replicating single-cell scaffolds: applying complex chemistries to nature's 3-D nanostructured templates," *Chemical Communications,* pp. 651-653, 2005.
[142] T. Muraki, M. Ueta, E. Ihara, and K. Inoue, "Enhancement of thermal stability of polystyrene and poly(methyl methacrylate) by cyclotriphosphazene derivatives," *Polymer Degradation and Stability,* vol. 84, pp. 87-93, Apr 2004.
[143] M. Giulianini, E. R. Waclawik, J. M. Bell, M. De Crescenzi, P. Castrucci, M. Scarselli, M. Diociauti, S. Casciardi, and N. Motta, "Evidence of Multiwall Carbon Nanotube Deformation Caused by Poly(3-hexylthiophene) Adhesion," *Journal of Physical Chemistry C,* vol. 115, pp. 6324-6330, Apr 2011.
[144] V. Saini, Z. R. Li, S. Bourdo, E. Dervishi, Y. Xu, X. D. Ma, V. P. Kunets, G. J. Salamo, T. Viswanathan, A. R. Biris, D. Saini, and A. S. Biris, "Electrical, Optical, and Morphological Properties of P3HT-MWNT Nanocomposites Prepared by in Situ Polymerization," *Journal of Physical Chemistry C,* vol. 113, pp. 8023-8029, May 2009.
[145] C. Caddeo, C. Melis, L. Colombo, and A. Mattoni, "Understanding the Helical Wrapping of Poly(3-hexylthiophene) on Carbon Nanotubes," *Journal of Physical Chemistry C,* vol. 114, pp. 21109-21113, Dec 2010.
[146] S. Hugger, R. Thomann, T. Heinzel, and T. Thurn-Albrecht, "Semicrystalline morphology in thin films of poly(3-hexylthiophene)," *Colloid and Polymer Science,* vol. 282, pp. 932-938, Jun 2004.
[147] R. Prasher, "Thermal interface materials: Historical perspective, status, and future directions," *Proceedings of the Ieee,* vol. 94, pp. 1571-1586, Aug 2006.
[148] G. Chen, "Size and interface effects on thermal conductivity of superlattices and periodic thin-film structures," *Journal of Heat Transfer-Transactions of the Asme,* vol. 119, pp. 220-229, May 1997.
[149] N. W. Ashcroft and N. D. Mermin, *Solid state physics*. New York,: Holt, 1976.
[150] R. E. Bolz and G. L. Tuve, *CRC handbook of tables for applied engineering science*, 2d ed. Cleveland, Ohio,: CRC Press, 1973.
[151] V. Singh, T. L. Bougher, A. Weathers, Y. Cai, K. Bi, M. T. Pettes, S. A. McMenamin, W. Lv, D. P. Resler, T. R. Gattuso, D. H. Altman, K. H. Sandhage, L. Shi, A. Henry, and B. A. Cola, "High thermal conductivity of chain-oriented amorphous polythiophene," *Nat Nano,* vol. advance online publication, 2014.
[152] X. Wang, V. Ho, R. A. Segalman, and D. G. Cahill, "Thermal Conductivity of High-Modulus Polymer Fibers," *Macromolecules,* vol. 46, pp. 4937-4943, 2013.
[153] S. Shen, A. Henry, J. Tong, R. T. Zheng, and G. Chen, "Polyethylene nanofibres with very high thermal conductivities," *Nature Nanotechnology,* vol. 5, pp. 251-255, Apr 2010.
[154] Y. K. Koh, S. L. Singer, W. Kim, J. M. O. Zide, H. Lu, D. G. Cahill, A. Majumdar, and A. C. Gossard, "Comparison of the 3ω method and time-domain thermoreflectance for

measurements of the cross-plane thermal conductivity of epitaxial semiconductors," *Journal of Applied Physics,* vol. 105, p. 054303, 2009.

[155] K. E. O'Hara, X. Hu, and D. G. Cahill, "Characterization of nanostructured metal films by picosecond acoustics and interferometry," *Journal of Applied Physics,* vol. 90, p. 4852, 2001.

[156] C. J. Vasquez, "Oxide-Coated Vertically Aligned Carbon Nanotube Forests as Thermal Interface Materials," Master of Science, Mechanical Engineering, Georgia Institute of Technology, 2014.

[157] C. Masarapu, L. L. Henry, and B. Wei, "Specific heat of aligned multiwalled carbon nanotubes," *Nanotechnology,* vol. 16, pp. 1490-1494, 2005.

[158] P. P. S. S. Abadi, "Mechanical Behavior of Carbon Nanotube Forests Under Compressive Loading," Ph.D. Dissertation, G.W. Woodruff School of Mechanical Engineering, Georgia Institute of Technology, 2013.

[159] J. V. Beck and K. J. Arnold, *Parameter estimation in engineering and science*. New York: Wiley, 1977.

[160] N. P. Bansal and R. H. Doremus, *Handbook of glass properties*. Orlando: Academic Press, 1986.

[161] W. Lin, J. Shang, W. Gu, and C. P. Wong, "Parametric study of intrinsic thermal transport in vertically aligned multi-walled carbon nanotubes using a laser flash technique," *Carbon,* vol. 50, pp. 1591-1603, 2012.

[162] M. T. Barako, Y. Gao, Y. Won, A. M. Marconnet, M. Asheghi, and K. E. Goodson, "Reactive Metal Bonding of Carbon Nanotube Arrays for Thermal Interface Applications."

[163] S. L. Hodson, T. Bhuvana, B. A. Cola, X. F. Xu, G. U. Kulkarni, and T. S. Fisher, "Palladium Thiolate Bonding of Carbon Nanotube Thermal Interfaces," *Journal of Electronic Packaging,* vol. 133, Jun 2011.

[164] Y. Won, Y. Gao, M. A. Panzer, S. Dogbe, L. Pan, T. W. Kenny, and K. E. Goodson, "Mechanical characterization of aligned multi-walled carbon nanotube films using microfabricated resonators," *Carbon,* vol. 50, pp. 347-355, Feb 2012.

[165] G. Zhong, J. H. Warner, M. Fouquet, A. W. Robertson, B. Chen, and J. Robertson, "Growth of ultrahigh density single-walled carbon nanotube forests by improved catalyst design," *Acs Nano,* vol. 6, pp. 2893-2903, 2012.

[166] J. Liu, O. Bibari, P. Mailley, J. Dijon, E. Rouviere, F. Sauter-Starace, P. Caillat, F. Vinet, and G. Marchand, "Stable non-covalent functionalisation of multi-walled carbon nanotubes by pyrene-polyethylene glycol through pi-pi stacking," *New Journal of Chemistry,* vol. 33, pp. 1017-1024, 2009.

[167] T. L. Barr, "Esca Study of Termination of Passivation of Elemental Metals," *Journal of Physical Chemistry,* vol. 82, pp. 1801-1810, 1978.

[168] P. J. Cumpson, "Estimation of inelastic mean free paths for polymers and other organic materials: use of quantitative structure-property relationships," *Surface and Interface Analysis,* vol. 31, pp. 23-34, Jan 2001.